THE UNIVERSITY *of* EDINBURGH

EngD in Offshore Renewable Energy

Thesis

Instream generation using tethered kites in the carousel configuration

August 6, 2021

Kristin N. Luttik

This thesis is submitted in part fulfilment of the requirements for the award of Engineering Doctorate, jointly awarded by the University of Edinburgh, the University of Exeter, and the University of Strathclyde.
The work presented has been conducted under the industrial supervision of the Scottish Association of Marine Science, as a project within the Industrial Doctoral Centre for Offshore Renewable Energy (IDCORE)

Industrial Supervisor:
Dr. Philip Anderson

Academic Supervisors:
Dr. Ignazio Maria Viola
Prof. Lars Johanning
Prof. Panagiotis Kaklis
Dr. Gregory Francois

Declaration

I declare that this thesis was composed by myself. The work contained herein is my own except where explicitly stated in the text by reference or acknowledgement. This work has not been submitted, in part or in full, for any other degree or professional qualification.

Signed:

Kristin Luttik
2020

Lay summary

This thesis has presented a low order numerical model model of a tethered kite, which allowed for control inputs. This presents a useful tool when illustrating kite dynamics and may be used to test kite control systems to follow optimum flightpaths. This conceptual model was used to demonstrate the benefit of applying control strategies to adjust kite forces throughout the carousel cycle to allow for a net power gain, even with minimal control complexity.

The model was expressed in state space allowing for optimization of turning and power controls for power production throughout the carousel cycle. Because the model optimizes power output over a repetitive carousel cycle, start-up strategies were presented which showed how a kite might get from a stationary position to the starting conditions of a cycle. This start-up sequence was demonstrated for a single kite positioned downwind. A parameter study was done to investigate the effect of various carousel configurations and operating points to show the effect on optimum flightpath and corresponding power output. Throughout all this the carousel velocity was assumed to be set to a constant rate. Subsequently the smoothing effect of adding multiple kites to the carousel was shown. As the carousel velocity was already kept constant the benefit of multiple kites on maintaining a constant carousel velocity were not included.

Finally a case study was presented which showed how the parameter study and flightpath optimization can be applied to preliminary sizing and design of a carousel in a particular tidal flow.

Acknowledgements

This thesis would not have been possible without a multitude of people, who I sincerely thank. First, all my supervisors; Phil, Ignazio, Lars, and Panagiotis; thank you for your support, guidance, advice, and input throughout this process. Special thanks to Gregory Francois, for his particular insights on optimization and control. To my colleagues and fellow doctoral students at SAMS; thank you for the support throughout this project and a weekly dose of levity and cake. To the members of my IDCORE cohort; misery loves company, and you have all provided a great source of that over the years.

I must also thank my friends and family for the ceaseless support, persistent positivity, and relentless reassurance. Throughout this process you have kept me grounded Thank you David, for the constant support and never ending stream of emails and messages over the years that provided a welcome and necessary source of encouragement and feedback.

This research was funded by the Energy Technologies Institute and RCUK Energy Programme through the Industrial Doctoral Centre for Offshore Renewable Energy (Grant number EP/J500847/1) and is gratefully acknowledged

Abstract

In recent years, kites are beginning to be considered as viable alternatives to offshore wind turbines, due to the potential reduction in levelised cost of energy and the increase in exploitable resource due to versatility of kite based generators. This thesis focuses on the kite carousel design, which consists of a ground based vertical axis generator with a number of kites attached. The kites are flown in a pattern that induces motion in the generator and thus produces power. This method of energy harvesting allows substantial scaling of devices. Device output depends not only on the available flow and kite size, but is further influenced by the length of the kite tether, the radius of the carousel structure, and the number of kites attached.

Although kites have been studied extensively in recent years, there is no consensus on the optimum design and configuration of the carousel. The thesis presents a minimum order model of a kite carousel. This numerical model is used to indicate the driving principles of the carousel and the importance of flightpath design on output. The presented model can be applied to various flow conditions. However, due to the definition of dimensionless power used, there is a scaling dependency of the model outputs regarding the kite tether length. An alternative method of describing the swept area of the carousel, based on the swept area of the kite flightpath, is used to mitigate this and indicate device efficiency in power extraction.

The flightpath optimisation and parameter study illustrate this scaling dependency and highlight the effect of the carousel radius and tether length on the optimized flightpath. These results then inform a case study for a carousel placed in a representative tidal flow. The case study describes a device with 8 kites attached to a 5 m diameter carousel that produces 64 kW over a representative tidal cycle with a peak flow of 2.2 m/s.

Nomenclature

Acronyms

KKT	Karush-Kuhn-Tucker conditions	-
ODE	Ordinary differential equations	-

Greek Symbols

α	Kite angle of attack	rad
Δ	Difference/change in variable	-
η	Efficiency factor	-
γ	Carousel rotation angle	rad
ν	Kinematic viscosity of fluid	m^2/s
ϕ	Kite reach angle from carousel arm	rad
ψ	Kite roll angle	rad
ρ	Density of fluid	rad
θ	Kite azimuth angle from vertical	rad

Roman Symbols

$Æ$	Aspect ratio	-
$\boldsymbol{D}$	Drag force vector	N
$\boldsymbol{e}$	Vector describing the local kite based coordinate system	
$\boldsymbol{F}$	resultant force vector	N
$\boldsymbol{G}$	Gravity force vector	N
$\boldsymbol{g}$	Gravitational acceleration	ms^{-2}
$\boldsymbol{L}$	Lift force vector	N
$\boldsymbol{s}$	Vector of states for optimization	
$\boldsymbol{T}$	transformation matrix between coordinate systems	-
$\boldsymbol{u}$	Vector of controlled variables for optimization	
$\boldsymbol{v}$	Velocity vector	ms^{-1}
$\boldsymbol{X}, \boldsymbol{Y}, \boldsymbol{Z}$	Vectors describing coordinate system	-

$\boldsymbol{x}, \boldsymbol{y}, \boldsymbol{z}$	Vectors describing local coordinate system	-
A	Area	m^2
C	Coefficient	-
c	chord length	m
d	Diameter	m
F	Force vector component	N
K	Induced drag coefficient	-
l	Length	m
m	Mass	kg
P	Mechanical power at carousel	N
q	Dynamic pressure	Nm^{-2}
r	Radius	m
Re	Reynolds number	-
s	Component in vector of states for optimization	m
t	Time	s
u	Component of controlled variable for optimization	
v	Velocity magnitude	m/s
W	Work	J
z	Height	m

Sub-/superscripts

$\dot{}$	time derivative of variable	$\cdot s^{-1}$
$_c$	refers to centrifugal force	
$_n$	step number	
$_p$	relevant to power	
$_0$	at initialization	
$_\phi$	relevant to tether reach angle ϕ	
$_\theta$	relevant to tether azimuth angle θ	
$_a$	relevant to the apparent flow	
$_B$	relevant to the carousel base	
$_b$	relevant to the intermediate local coordinate system at tether base	

$_D$	relevant to drag
$_e$	at termination
$_f$	relevant to flow
$_k$	relevant to kite
$_L$	relevant to lift
$_P$	relevant to power
$_r$	at reference point
$_T$	relevant to tether

Contents

List of Figures

List of Tables

Chapter 1

Introduction

1.1 Background and motivation

As renewable energy keeps developing it is important to keep pushing the boundaries to find new ways of extracting energy in various locations [7–16]. Thus far wind turbines have become a substantial source of renewable energy production throughout the world [17, 18]. However, despite continued technological advances there remain issues that limit the technical resource available [19]. Two of these limits are structural, concerning device size, and accessibility to exploitable sites [9]. Similarly, public backlash due to the invasive installation requirements, and resulting visual and audible impact of these turbines has prevented further viable areas from being exploited. Due to its design, the rated power output of a turbine is directly related to its size. As devices increase in capacity and size the practicalities of transport and installation become critical to the feasibility of a project.

In an effort to overcome these obstacles research has turned to airborne wind energy devices [15]. In effect this replaces the large cumbersome turbine structure with a comparatively light tether and kite. This concept was first proposed by Loyd in 1980 [20], and has since then evolved into a full field of study, which if successful could offer a cost effective alternative to wind turbines, with a substantially reduced visual and audible impact. As such, not only would kites provide financial benefits over turbines [12], they could provide an alternative source of renewable energy where practically turbines would be inappropriate [15]. While the airborne aspect of this concept is being

developed by a number of different research groups and industrial companies, other's have starting expanding the scope to marine generation using submerged kites [21–24].

Challenges in this sector include maintaining control of the kite in varying flow conditions, and developing automated launching sequences [11]. As such, the focus has been on developing small scale, single kite devices while working to overcome these control challenges. Despite these practical issues, references have been made in literature to the potential of multi-kite systems. One such concept first introduced by Williams et.al. in 2007 [1], and again looked at by Fagiano in 2009 [2] is that of the kite carousel. A commercial company based in Italy, KiteGen, has proposed a large scale carousel capable of generating 1 GW of output with a ground radius of 1 mile and 100 kites [25]. In this concept a ground based generator would be rotated by a number of attached, controllable kites. A further advantage to this configuration lies with the scalability. As such rather than creating an array of multiple devices, it is possible to scale up as proposed by KiteGen [26] by increasing the radius of the generator track and the number of kites attached.

Over the past years tidal energy generation has started evolving with a number of devices starting to export electricity to the grid [14]. As such it is worth investigating if the proposed benefits of airborne kites, would translate to the submerged case. This is of particular relevance since turbines generally operate at higher efficiency in higher velocity flows, as such slower ocean currents do not present ideal conditions. However, since kites have the ability of cross-stream motion, they are able to operate in far slower flows. This further opens the exploitable resource and could provide a niche where kites could operate in conditions previously thought unsuitable [24].

While there has been a substantial amount of work done on kite control models [2, 27–32], there has been limited validation of these models. This thesis describes a representative proof-of-concept model, which is used to investigate the feasibility of the carousel design. The numerical model will be used to test a number of design conditions, leading to a parameter study which will show the effect of varying design elements on device operational efficiency; Resulting in a model which can be applied in the commercial sector to size carousel type devices and compute device potential.

1.2 Aim and Objectives

Loyd [20] first proposed using a kite to mine kinetic energy from the wind through cross-wind flight. Since then, particularly in the past two decades, a multitude of research has gone into turning this concept into a reality. A multitude of kite based designs have been proposed, however no consensus has been reached on the best method of converting wind energy to electrical power. One concept which has been little explored is the vertical axis kite turbine, also known as the carousel. This concept has been briefly investigated [1, 33], however conclusions reached concerning operation and output differed.

1.2.1 Aim

This project aims to prove the output potential of the kite carousel. This thesis will present a high level global carousel model which can be applied to any flow condition. A preliminary evaluation done of a submerged design in tidal flows shows the potential use and optimum design with the data available, and shows the potential for using the model developed as a design tool for further product development.

1.2.2 Research question and objectives

To create a comprehensive global carousel model two research objectives are defined. This section will show how this thesis approaches each research objective and how they fit within the overarching research question. This research question this thesis aims to answer is formulated as follows:

Is the kite carousel a realistic design for power extraction from a fluid flow?

This aim is specifically geared toward the engineering feasibility in terms of dimensioning and power output. The economic and environmental feasibility are beyond the scope of this thesis. To answer the research question three core objectives are identified:

- Investigate the parameter space of the kite carousel to determine the effects of carousel diameter and tether length on the flightpath and overall output of the device, through a numerical model,

- Quantify realistic power extracted by a kite carousel, with model simulations.

In order to investigate the parameter space of the kite carousel, a numerical model is developed. Due to the high computational power, and time requirement for a full computational fluid dynamics model of the carousel design, it is decided to create a numerical model. The numerical model is used to identify the parameter space and investigate the effect of tether and carousel dimensions on device forces and output power. The knowledge gained from this investigation are subsequently used to analyze preferable design conditions for a carousel in a flow; which are used in a simulated case study to indicate a potential power output in ideal conditions.

1.3 Original contribution

As mentioned the carousel design has been looked at twice before, the model created in this thesis allows for control of both the angle of attack and the rate of roll throughout a flightpath simulation. Additionally this thesis discusses the practical requirement of initiating a flightpath from a stationary starting point. Although this thesis results in a case study of a submerged carousel, the dimensionless analysis allows for the two reference points from literature to be compared and evaluated.

1.4 Methodology

The method in which this thesis is structured to meet the aims discussed in the previous section is illustrated through a flowchart shown in figure 1.1.

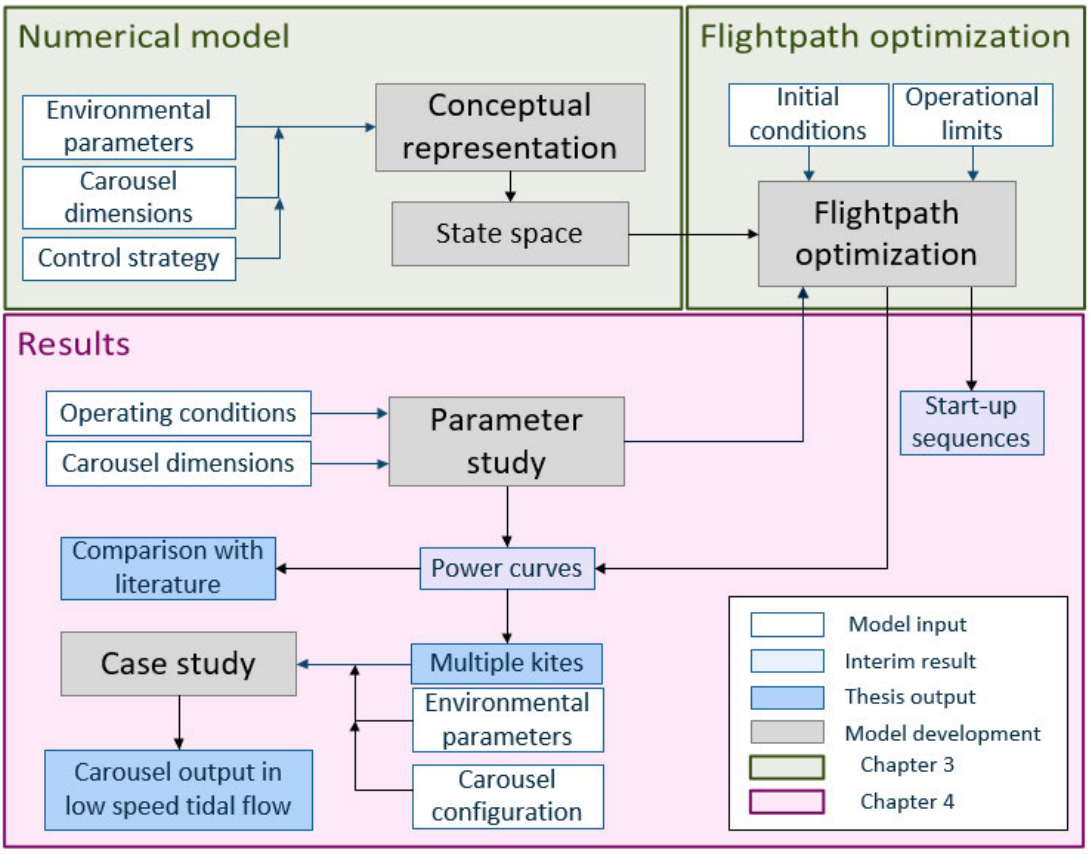

Figure 1.1: Thesis structure showing chapter distribution and thesis outputs

The feasibility of the carousel will be shown based on the numerical model developed. The flightpath optimisation and parameter study are critical to this feasibility as the determination of the best configuration greatly impacts the potential output of the device. Two main criteria are used to judge the technical feasibility of the concept. These criteria include:

- Ratio of power production to device size.
- Consistency of power output.

The ratio of power output to device size is used as a measure for device efficiency and is indicative of how the carousel would compare to existing turbine and kite based technology. Particularly in regards to marine energy the development of a device depends greatly on the potential to reduce costs of existing technology. The consistency of power output is a substantial concern for kite based devices. Kite based generators typically show highly periodic outputs, with times of requiring energy input in order to reposition the kite to its original state. One of the benefits of the kite carousel is that multiple

kites can be used on a single device in order to produce more consistent power output. This reduces the need of high capacity power electronics for smoothing of the output. The numerical kite model stands at the core of this project with a focus on being computationally efficient to the point where it runs quicker than real-time on a regular computer. Such that it can be used as the basis of an eventual control system. This model serves as a the basis of a parameter study, investigating the affects and impacts of device parameters, and required kite flight patterns. The parameters investigated will include the carousel radius to tether length ratio, and the ratio of generator angular velocity to the flow speed.

Approaching the research problem in such a way has numerous benefits. First, having a model that is effective yet computationally efficient substantially lowers the cost of simulation since the model can be run on a regular computer. As such it may form the basis upon which further research into this design concept is based. Alternatively, it could result highlight areas where additional technological advancements would be required to achieve feasibility.

1.5 Limitations to scope

The focus of this thesis is creating a high level kite carousel model which, using flightpath optimization, gives an indication of device output given design parameters. To this end assumptions are made for idealised flow and kite behaviour to keep the computational power required to run the full model to a minimum. The mathematical formulation of this low order model also allows for insights on the main constraints and governing laws of the system. These assumptions and their effects on the model are discussed in chapters 3 and 4.

1.6 Thesis structure

The thesis is structured into six core chapters. First, in the **Literature review**, relevant literature is introduced and discussed. The literature addresses common methods of using kites for energy generation and studies done evaluating them. While the majority of the literature refers to airborne kites, recently some studies have focused on

using submerged kite type wings in ocean currents.

In the **Numerical model** chapter, the progression of the numerical model from conceptual representation to state space formulation is shown . The initial representation focusses on visualizing kite responses to control inputs in an intuitive and realistic manner. The second section of this chapter focusses on the state space representation of this model. Here the model is adjusted such that it can be used in optimization software to find a control sequence that results in a continuous periodic flightpath. The additional steps toward optimization of the flightpath are discussed in the third section of this chapter

The **Results** is explained in chapter 4. This chapter discusses the trajectories resulting from running the optimization problem discussed in the previous chapter. The effect of varying carousel configuration on device performance is shown and explained. The conclusion to this chapter includes a sanity check of the model outputs through dimensional analysis and comparison with results found in literature. Finally, a case study is presented indicating potential output of a carousel placed in a representative low speed tidal flow, with a look at how adding multiple kites to the carousel impact the overall output.

In **Conclusions**, the results of this piece of research are discussed. The conclusions drawn throughout are summarized with a focus on the effect of the limitations to the project scope on the results, which leads into a discussion regarding further work that may follow from the results presented here.

Chapter 2

Literature review

Over the years a focus on renewable energy has pushed the industry to find new ways of extracting energy from the environment in a sustainable fashion [7–19]. In the past decade kite based generations systems have progressed from grand conceptual ideas through the development phases to fully operational prototypes with the potential to becoming an economic alternative to conventional turbines [34]

Similarly, in the past years study in tidal energy extraction has expanded to included kite-based devices. The benefit of controllable kite type hydrofoils [35], as opposed to tidal turbines, being proposed as potentially opening new extraction sites which were previously deemed unsuitable for extraction do to lower flow velocities, or less than ideal site depth.

This literature review provides perspective on the background of previous work and research framing the work done for this thesis.

2.1 Airborne wind energy

The concept of airborne wind energy using kites was first introduced by Loyd [20] in 1980. Since then much research has focussed on various methods of extracting energy from an airflow at high elevation. In this section a brief overview of kite dynamics and the general concepts behind common airborne wind energy designs are discussed with a focus on the carousel type model which is the focus of this thesis.

2.1.1 Kite aerodynamics

Like any wing a the flow around the aerodynamic profile of a kite induces lift (L) and drag (D) forces, which act through the centre of pressure ($c.o.p$), as illustrated in figure 2.1a. Lift acts perpendicular to the apparent wind, while drag is parallel in the direction of the wind. The apparent wind is defined as the wind vector as seen by the kite, taking the induced wind vector due to the kites own velocity into account, as shown in 2.1b. This as the kite velocity changes, so does the apparent wind vector and consequently the lift and drag of the kite. Kite behaviour is also affected by the kite gravity force(G), applied in the centre of gravity ($c.o.g$). Where the kite differs from a regular wing is that it is fastened to the ground by a tether, adding a tether force (F_T). The computation of these forces are explained in depth in chapter 3.1.2.

The tether force is the key to being able to extract power using a kite. In the steady state the tether force equals the sum of the kite aerodynamic and gravity forces. Extracting power with a ground based generator adds an additional force at the base of the tether, and an additional movement of the kite. This additional kite movement adjusts the kite velocity and thus the apparent wind seen by the kite, which affects the aerodynamic force vectors. In order to sustain power take off a control strategy must be applied. A general overview of common power take off strategies is given in section 2.1.2.

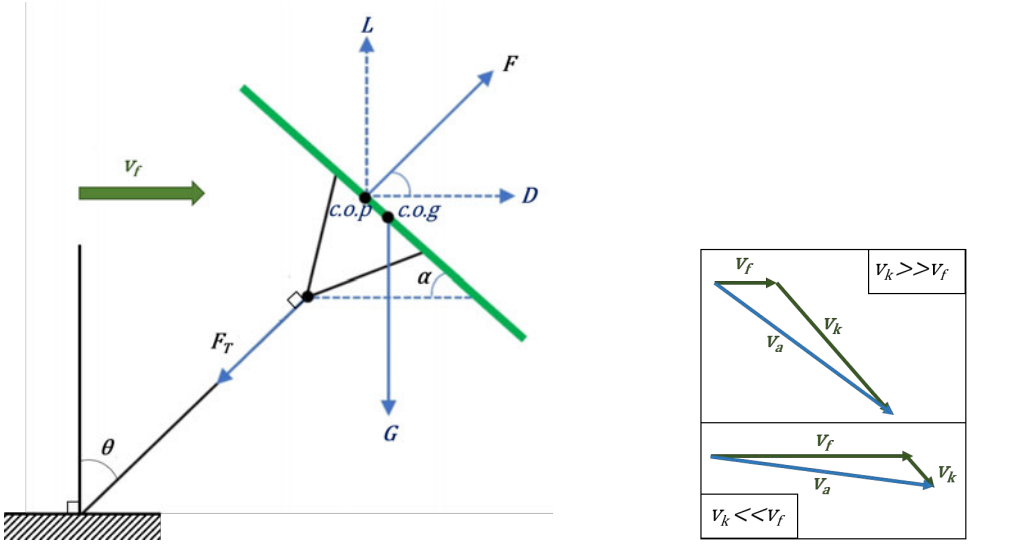

(a) FBD of kite

(b) Definition of apparent velocity

Figure 2.1: Freebody diagram illustrating kite aerodynamics

2.1.2 Kite systems

In the past decade research into kite based generation has increased dramatically. While much of this is academically based, there are strong ties with commercial companies who are actively working towards competitive power generation. Airborne wind energy concepts can be divided into two core designs, distinguished by the placement of the generator:

- Lift based, where the kite is used to induce motion in a ground based generator through tension in the tether caused by kite motion. The most common of these designs is the pumping kite design, where the kite is used to un-reel a tether and is subsequently reeled back in under lower drag conditions to create a net power output.
- Drag based, a platform type design where the generator is mounted at the end of the tether on an airborne structure and power is transmitted through a hybrid tether structure to the ground. A common design has a number of turbines mounted on an airborne wing, which is controlled in crosswind flight to increase the apparent wind experience by the turbine.

These methods have been researched and in some cases progressed toward early commercial development. Thus far, practicality has limited the bulk of research and development to single kite systems. Focus on modelling kite behaviour [36–45], has progressed from proof of concept to forming the base for development of control strategies for kites. These model range from point mass models [46], to high-order finite element models [37].

While mention has been made of multi-kite systems in research [9, 47, 48] as a potential way to further increase power output, issues with control and lack of firm, validated kite models, have limited the development of these concepts to full physical models. Although, there has been some preliminary modelling done concerning the carousel design [2, 49, 50].

Carousel Models

Williams *et.al.* [1] and Fagiano [2] investigate the potential of a kite carousel type

device, albeit taking two distinctly different approaches. While Williams looks at the case as a single cyclical problem of a vertical axis generator rotated by the movement of a kite; Fagiano dissects a full generator cycle into four separate stages, where a kite pulls a trolley along a circular track with generation coming from the spinning of the trolley wheels. In both cases the kite flight path is optimized to maximize predicted power output. Williams *et.al.* then continue to perform a quick sensitivity study to show the effect of variable kite size and wind velocity on the optimum flight trajectory, whereas Fagiano focusses on the control required to follow the decided upon flight trajectories. Due to the different approaches to control strategies the optimized flightpaths show distinct differences These resulting trajectories of each method are shown in figures 2.2, and 2.3. Williams *et.al.* optimize the flightpath to match the generation rotation, which lead to quick crosswind loops. In contrast Fagiano simulates the carousel as a number of vehicle being pulled around a circular rail with power take off through wheel mounted generators. In order to move upwind again the vehicles are powered through the rail. This process is optimized by dividing up the carousel period in distinct sections which are optimized individually. The result is a series of quick crosswind figure 8 movements during the down wind phase and the kite being flown to zenith to depower during the upwind phase.

Williams uses point-mass model, where tether mass and drag are ignored, and the kite is controlled by altering the angle of attack and the roll angle. Also, the power generation is assumed to be perfectly efficient, which means that friction losses are ignored. The numerical results were compared with flight test data, which was gathered using a kite demonstration rig. For the optimization of the flightpath it was assumed that the wind speed and direction remain constant.

The sensitivity study investigated the change in optimum flight path for a range of wind speeds and kite sizes. Looking at the average power produced over a cycle, it appears to be directly proportional to the kite area, and increases with a cube of the wind speed. This is taken as an implication that the calculated flight paths are indeed optimal.

Williams*et.al.* continued their work on optimizing flight paths by investigating the optimized flightpath for towing and power generating kites [51]. Which resulted in a distinctly different flightpath, mainly due to the change in purpose concerning the track

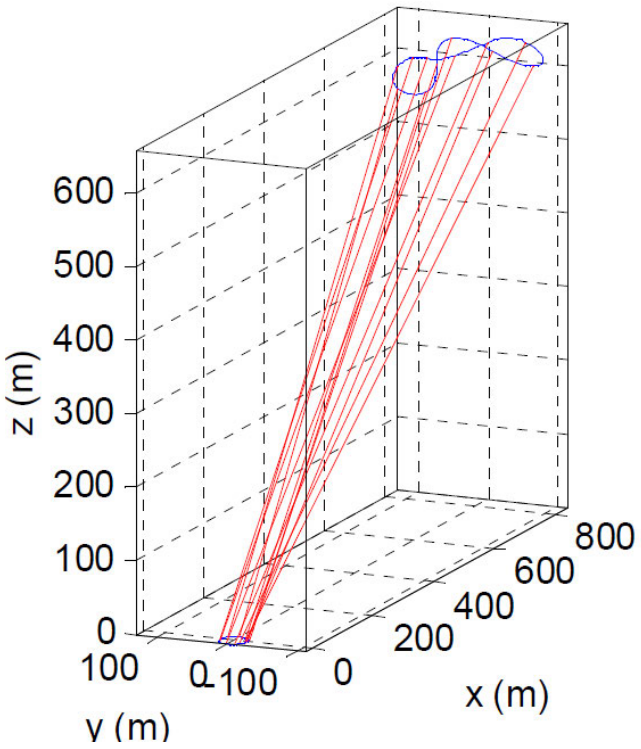

Figure 2.2: Optimal flightpath computed by Williams*et.al.* [1]

of the ground station.

A distinct difference between the Fagiano and Williams methods is the resulting kite trajectory computed. While the Williams model results in a smooth locus, Fagiano ends up with distinctly different kite behaviour for each of the 4 stages of the full cycle. Other than the alternative approach to the cycle definition, the main reason for the alternative trajectories is assumed to be due to the distinctly larger ground track radius used in the Fagiano model, as visible in figures 2.2, and 2.3. This results in a far longer stretch of downwind movement, in which case figure eights are used to maximize the use of crosswind motion. Fagiano further elaborates on the proposed control methods in future published works [33, 49]. It is important to consider appropriate types of control which do not require a large amount of computational power, but are able to track movement along a complex prescribed trajectory; control methods proposed by Baayen and Ockels [52], Jehle [53], and Houska and Diehl [27], show potential for tracking and controlling kites to follow a set flightpath. In 2016, Gerhmann [54] and Bechtle [55] published a concept to test flightpaths and control strategies for kites, using a deconstructed UAV attached to a tether. This low cost method is not dependant on

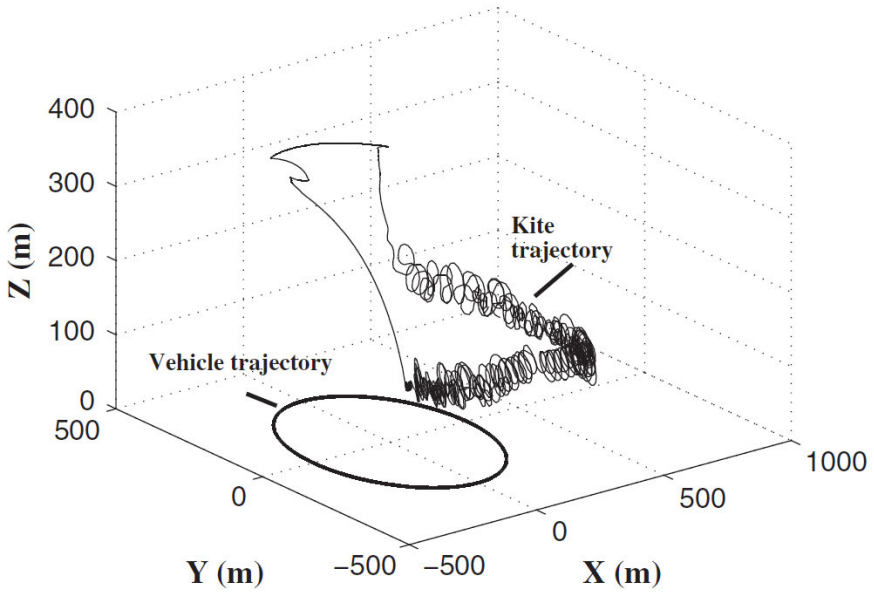

Figure 2.3: Optimized flight path around carousel computed by Fagiano [2].

strict wind requirement like full sized kite testing is.

Flightpath Over time much research has been done into how a kite flies and what the best method of determining beneficial flightpaths is [56–59]. A horizontal figure 8 is a simple way to control a kite to fly crosswind without tangling the lines. Although the shape and orientation of this figure 8 can vary substantially depending on the control input to the kite. For energy generation it is important to have a steady periodic flightpath without a net tether twist.

2.2 Submerged applications

While there has been commercial development of underwater kite systems, such as by the marine energy company Minesto UK, Ltd with their Deep Green technology; with a small turbine mounted on a kite type hydrofoil flying in a cross flow figure 8 flightpath to increase the apparent flow speed seen at the turbine. The academic research on this subject is limited, although Jansson [60] did write his Masters thesis on the hydrodynamic analysis and simulation of a Deep Green type device. In his thesis, Jansson describes the Simulink model he has set up using elements of various flight, and underwater simulations showing a representative model following a set figure 8 flightpath.

However, power take off and tether drag is not included in this model. In 2016 Kregting *et.al.* [61] delivered a baseline report for the environmental monitoring of Minesto's Powerkite project, specifically with respect to noise and collision risk with marine life. These aspects are further investigated [35, 62–64], and conclude that with appropriate operational limits a submerged kite can suitably mitigate risks to marine life.

In recent years research at Worcester Polytechnic institute has focussed on higher level numerical models of a submerged tethered wing. The studies published as a result of this are the first of its kind in this field. Olinger and Wang [22] investigated the energy harvesting potential of a system similar to an inverted Deep green concept. In this study the submerged wing is attached to a floating buoy, such that it can take advantage of the higher flow velocity closer to the surface, without the added drag of a long tether. This paper serves as a baseline technical study and focusses on tether dynamics and cavitation.

It is found that the dynamic pressure ($q = 0.5\rho v_a^2$) experienced by an underwater kite is increased by a factor 50, when compared to airborne kite systems. This is due to the increased density of water with respect to air, albeit compensated by the reduced flow velocity experienced. As such, it is concluded that significantly higher strength materials would be necessary for underwater kites. Hence, Olinger and Wang focus on rigid wings made from high-strength materials.

Due to the low power generated in turns, the net power actually temporarily goes negative. This is due to the larger steering input requirements during turns, and would support the potential benefit of a smooth locus as suggested by Williams. The cavitation boundaries are investigated for both the kite and the kite-mounted turbine. It is concluded that while a potential issue for mounted turbines, cavitation is unlikely at the kite itself.

A subsequent study by Ghasemi *et.al.* [3] builds on Olinger's work. Here the focus lies on the underwater pumping kite concept. As opposed to the previous study, the aim is to capture the non-linear effects in the flow around the kite. This is achieved by solving the full Navier-Stokes equations for the direct area around the kite, as opposed to just solving the differential equations using linear, inviscid flow models. The resulting flow simulations are shown in figure 2.4. Since the reel-in period does not fully return the

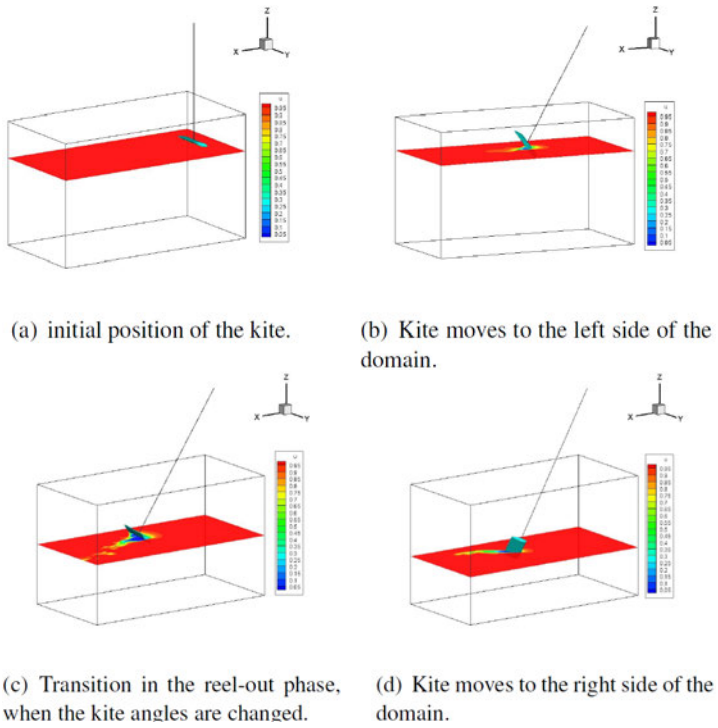

(a) initial position of the kite.

(b) Kite moves to the left side of the domain.

(c) Transition in the reel-out phase, when the kite angles are changed.

(d) Kite moves to the right side of the domain.

Figure 2.4: Snapshots from Ghasemi simulation [3].

kite to its starting location, the simulation does not cover a full pump cycle. As such the simulation should be expanded to cover at least a full cycle, for accurate power estimations in the future. While these results are not verified in any way, it is mentioned as 'future work' that they will be verified by cross referencing them with the theoretical predictions of Loyd [20].

In 2015, Li *et.al.* [65] presented their paper on the control of an undersea kite system. This again analyses a Minesto-type device, would be installed on the ocean floor. The kite model produced applies incompressible aerodynamic principles to the hydrokinetic forces, with a six degree-of-freedom kite model. System control is based on a proportional derivative controller, and verified with a baseline simulation. Li states that an underwater kite system could generate up to 50% of the theoretical maximum power. When compared to a marine turbine of the same cross section, the kite mounted turbine could produce up to seven times as much power, due to the increased apparent flow velocity caused by the cross flow motion of the kite.

2.3 Optimization

The optimization of a system includes all aspects from operation to design. In terms of kite power, optimization usually refers to finding the best way to control the kite in terms of effective force transfer and power transfer. In the last years this has ranged from investigating beneficial flightpaths [29, 32, 66–71], to optimizing control to allow kites to match the flightpaths in varying weather conditions as closely as possible [28, 30, 72–82]. As mentioned before, these methods and models predominantly geared toward a single kite device, and result in flightpath solutions that do not translate directly to the carousel problem.

For the carousel it was decided to use software called ACADO which is a collection of algorithms created for automatic control and dynamic optimization, and has been previously used for kite optimization by Ahbe [66]. This software is designed to be compatible with MATLAB scripts and has been used to solve a wide range of optimization problems [83–85].

Chapter 3

Numerical Method

The first two sections of this chapter are based largely on the contributions made to Renew 2018 [86]. It describes the work that lead to a highly reduced order model developed to be faster than real time and functions as a first step toward the generic carousel model presented further on. As the focus is on the carousel method of power take-off, the tether is kept at a constant length throughout, which reduces degrees of freedom and keeps model complexity low. In section 3.1 the model is presented conceptually, this is then written as a set of ordinary differential equations (ODE) in section 3.2. Further adjustments to this model for it to work with optimization toolkit is described in section 3.3.

3.1 Conceptual representation

An initial kite model was constructed with a focus on providing a visual representation of the behaviour of a kite under idealised conditions, with the ability to control said behaviour by adjusting the relative lengths of the steering lines. This behaviour was modelled by applying rotations to a kite-based reference frame with respect to a global frame of reference, initially based at the end of the tether, as shown in figure 3.1. When full carousel motion is considered the base of the tether is rotated around the base coordinate system.

Figure 3.1 shows a neutral kite position, where $\boldsymbol{Z_k}$ is in line with the pointing vector of the tether $\boldsymbol{X_T}$. The definition of the axes is critical as the position and orientation of

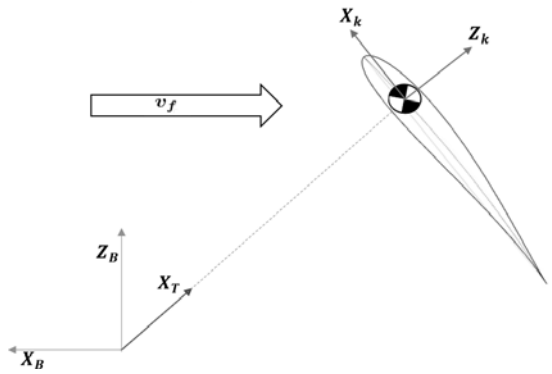

Figure 3.1: Reference frames used in initial model setup.

the kite frame evolves throughout the timed simulation to represent the attitude of the kite at each point in time. The model represents kite control through induced roll and pitch around $\boldsymbol{X_k}$, and $\boldsymbol{Y_k}$ respectively. The global reference system is defined afrom the base of the carousel $\boldsymbol{Z_B}$ pointing vertically upward, and $\boldsymbol{X_B}$, directed directly upwind.

3.1.1 Model Assumptions

In order to reduce computational power required, a number of assumptions were made. These assumptions are described in this section.

For comparison of the inertia terms, the kite is modeled as a point mass at the end of a tether. However, it is assumed to have an aerodynamic profile that can be adjusted for control purposes. It is assumed that this aerodynamic profile is kept a constant shape with the only changes in orientation due to control inputs.

While this assumption substantially reduces the degrees of freedom of the system, and thus the computational power required to solve a simulation, it does represent an idealised version of the design.

3.1.1.1 Flow profile

The apparent flow seen by the kite, $\boldsymbol{v_a}$, depends on the kite velocity, $\boldsymbol{v_k}$, and the component of the general flow velocity parallel to the kite velocity vector, $\boldsymbol{v_{f_k}}$, as shown in

$$\boldsymbol{v_a} = \boldsymbol{v_k} - \boldsymbol{v_{f_k}} \tag{3.1}$$

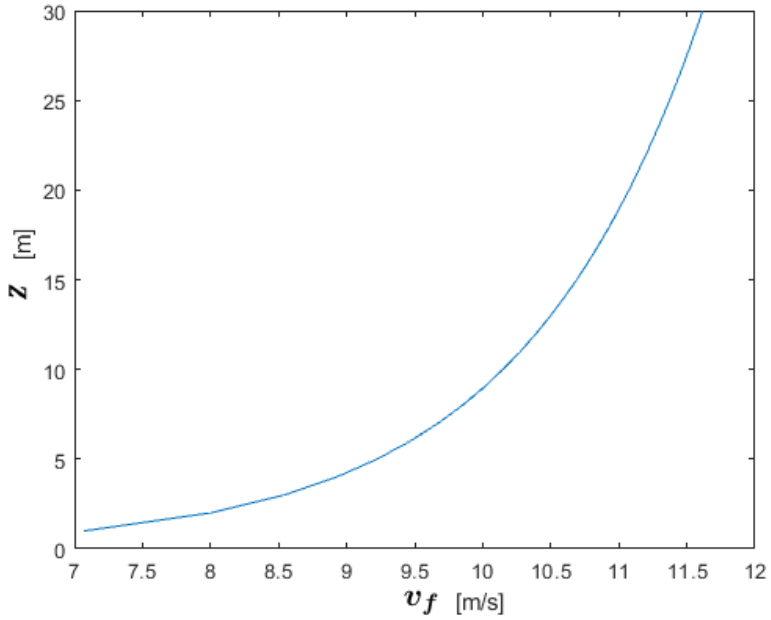

Figure 3.2: Flow profile used for numerical model

which varies dependant on height from the surface. This height dependency is shown through equation 3.2

$$\boldsymbol{v_{f_k}} = \boldsymbol{v_{f_r}} \frac{\ln\left(\frac{z_k}{z_0}\right)}{\ln\left(\frac{z_r}{z_0}\right)} \tag{3.2}$$

where a logarithmic profile is applied as done and proposed by Stull [87]. Here the wind velocity $|\boldsymbol{v_{f_k}}|$, is deduced kite level z_k, from the wind measured at a reference height ($|\boldsymbol{v_{f_r}}|$ at z_r), using a roughness length ($z_0 = 0.005$) m for a smooth landscape. The flow profile used here is depicted in figure 3.2, with a reference velocity of 8 m/s at 2 m height.

3.1.1.2 Power control

The kite power is controlled through the manipulation of the kite angle of attack α_k. This is done by adjusting the length of the rear control lines, which are attached to the trailing edge of the kite, with respect to the main power line, attached at the leading edge of the kite. Lengthening the control lines reduces α_k and subsequently the overall angle of attach α which is the sum of the kite angle of attack and the angle of attack

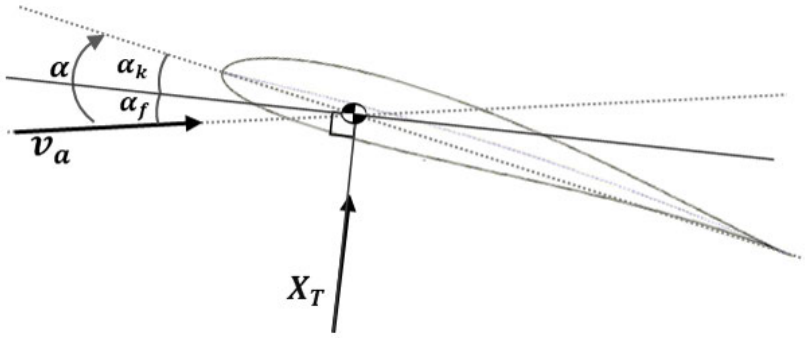

Figure 3.3: Side view of kite showing definition of α

of the flow α_f, illustrated in figure 3.3, and computed as follows:

$$\alpha = \alpha_k + \alpha_f \tag{3.3}$$

with,

$$\begin{aligned} \alpha_k &= \sin^{-1}\left(\boldsymbol{X_T} \cdot \boldsymbol{X_k}\right) \\ \alpha_f &= \sin^{-1}\left(\frac{\boldsymbol{v_a} \cdot \boldsymbol{X_T}}{|\boldsymbol{v_a}|}\right) \end{aligned} \tag{3.4}$$

The force transmitted through the main power line is adjusted due to the effect of adjusting α on the lift and drag coefficients C_L and C_D, which subsequently determine the aerodynamic forces on the kite. Figure 3.4 shows the initial relationship between α and the 2D aerodynamic coefficients, which is similar to those used by de Lellis *et.al.* [88], Fechner [4], and Spera [5]. These coefficients are translated to the full 3D lift and drag coefficents through:

$$\begin{aligned} C_L &= C_{L2D}\left(\frac{Æ}{Æ+2}\right)\alpha \\ C_D &= C_{D_0} + \frac{C_L^2}{\pi Æ \eta} \end{aligned} \tag{3.5}$$

This was used to interpret the initial acceptable working range of α to be $[-10°, 20°]$

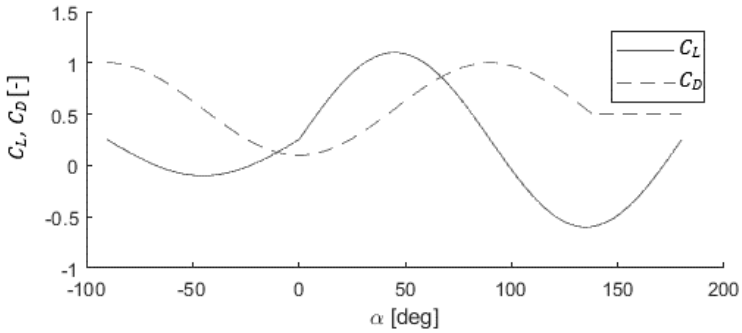

Figure 3.4: Aerodynamic coefficients used for initial estimation [4, 5]

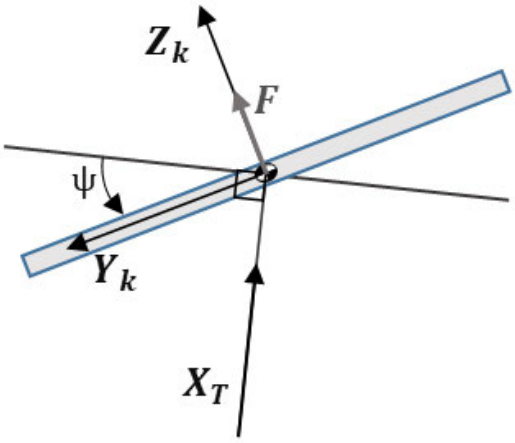

Figure 3.5: Rear view of kite showing the effect of ψ

3.1.1.3 Turning control

Turning dynamics of a flexible kite have been modelled and approximated extensively by de Lellis *et.al.* [75], and Bosch *et.al.* [37]. Typically a turn rate law is used to represent kite turning in numerical models [89].

In this case, a pseudo control is implemented in the numerical model, similar to that proposed by Williams *et.al.* [1], and Paiva & Fontes [31], where the roll angle is controlled to adjust the orientation of the aerodynamic forces acting at the kite point mass. Attitude dynamics were similarly not accounted for. It is assumed that the kite autocorrects to align $\boldsymbol{X_k}$ with the incoming flow. The roll accounts for a rotation of $\boldsymbol{Y_k}$ around the kite $\boldsymbol{X_k}$ axis, which in turn adjusts the angle of the lift force generated, as in figure 3.5. As the kite is moved to align $\boldsymbol{X_T}$ with the resultant force vector $\boldsymbol{F}$, this rotation causes a sideways motion in the kite. The sideways motion consequently adjusts the incoming flow velocity and subsequently the kite pointing vector $\boldsymbol{X_k}$ is ad-

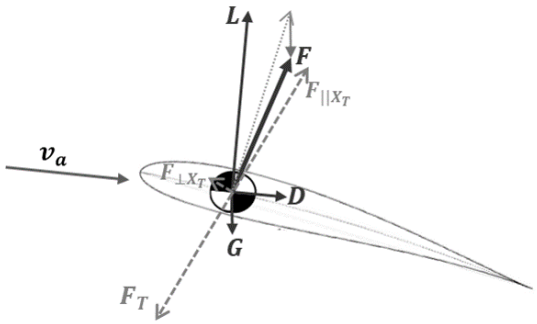

Figure 3.6: Kite load case

justed as well. The yaw turn rate is limited to allow for side slip at low kite velocities such as is experienced at the edges of the wind window.

3.1.1.4 Tether contributions

It is assumed that due to the short tether length used for the numerical model of less than 500 m, the tether would behave as a straight, rigid, inelastic, rod connecting the kite to the ground station. The mass of the tether is included in point mass of the kite, although in reality the tether mass is distributed along the full length of the tether. As a result the computed gravity and centrifugal forces at the kite will be slightly overestimated due to the marginally larger mass contribution of the concentrated tether mass.

At this point the tether drag contribution was assumed to be negligable. However it is factored in with later iterations of the model; first as a factor of the kite drag area as shown by Argatov *et.al.* [36], and later with a basic drag contribution by viewing the tether as a long cylinder, as in Fagiano [2].

3.1.2 Load case

The load case considered included both aerodynamic and gravity forces. The manner in which these forces act upon the point mass representation of the kite are shown in figure 3.6. As shown here the resultant force, $\boldsymbol{F}$, is computed as the sum of the lift,

drag, and gravity forces ($\boldsymbol{L}$, $\boldsymbol{D}$, and, $\boldsymbol{G}$) respectively, as shown in

$$\boldsymbol{F} = \boldsymbol{L} + \boldsymbol{D} + \boldsymbol{G} \tag{3.6}$$

Where the lift, drag and gravity vectors are computed with:

$$\begin{aligned} \boldsymbol{L} &= \frac{1}{2}\rho_f A_k C_L \left|\boldsymbol{Y_k} \times (\boldsymbol{v_a} \times \boldsymbol{Y_k})\right|^2 \frac{\boldsymbol{Y_k} \times \boldsymbol{v_a}}{|\boldsymbol{Y_k} \times \boldsymbol{v_a}|} \\ \boldsymbol{D} &= \frac{1}{2}\rho_f A_k C_D \left|\boldsymbol{v_a}\right| \boldsymbol{v_a} \\ \boldsymbol{G} &= (m_k + m_T)\, \boldsymbol{g} \end{aligned} \tag{3.7}$$

with air density ρ, kite area and mass, A_k and m_k, and tether mass m_t. The vector $\boldsymbol{g}$ indicates the gavitational acceleration. The apparent flow $\boldsymbol{v_a}$ is computed as per equations 3.1 and 3.2. Figure 3.6 shows how $\boldsymbol{F}$ is decomposed into the radial component parallel to the tether, $\boldsymbol{F}_{\parallel \boldsymbol{X_T}}$, and the tangential component perpendicular to the tether $\boldsymbol{F}_{\perp \boldsymbol{X_T}}$, of $\boldsymbol{F}$; which are computed numerically as follows:

$$\begin{aligned} \boldsymbol{F}_{\parallel \boldsymbol{X_T}} &= (\boldsymbol{F} \cdot \boldsymbol{X_T})\, \boldsymbol{X_T} \\ \boldsymbol{F}_{\perp \boldsymbol{X_T}} &= \boldsymbol{X_T} \times (\boldsymbol{F} \times \boldsymbol{X_T}) \end{aligned} \tag{3.8}$$

Since the kite tether is presumed to be of a constant length and inelastic, the kite radial acceleration is zero, which sets the tensile force in the tether to $F_T = \left|\boldsymbol{F}_{\parallel \boldsymbol{X_T}}\right|$. The tangential kite velocity is expressed through:

$$\boldsymbol{a}_{\boldsymbol{k}_{\perp \boldsymbol{X_T}}} = \frac{\boldsymbol{F}_{\perp \boldsymbol{X_T}}}{(m_k + m_T)\, l_T} \tag{3.9}$$

Carousel effects The carousel was modelled to rotate at a set angular velocity. As such the power take off, P could be computed using the horizontal component of the tether tension. As the tether is assumed to be inelastic there are no losses experienced through stretching, as such the tensile force is perfectly transmitted through to the base of the tether. As such the power is computed using the component of $\boldsymbol{F}_{\parallel \boldsymbol{X_T}}$ parallel to velocity vector of the base of the tether $\boldsymbol{v_T}$; $\boldsymbol{F_p}$, as shown:

$$P = |\boldsymbol{v_T}|\, |\boldsymbol{F_p}|\, \eta \tag{3.10}$$

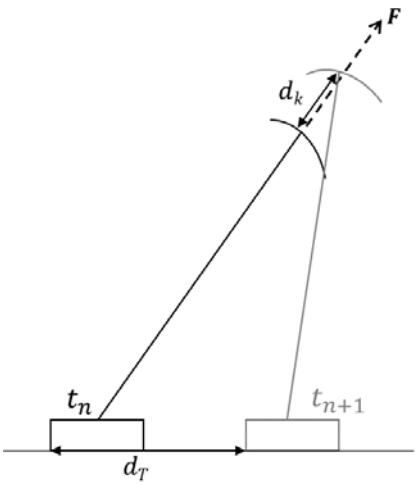

Figure 3.7: Kite motion due to carousel rotation

where the efficiency factor, η, is included to account for system losses. $\boldsymbol{F}_{\|\boldsymbol{X_T}}$ is adjusted to account for the reduction in tensile force due to the movement of the carousel $\boldsymbol{F}_{\|\boldsymbol{X_{Tc}}}$ by:

$$\begin{aligned} \boldsymbol{F_p} &= \left(\boldsymbol{v_T} \cdot \left(\boldsymbol{F}_{\|\boldsymbol{X_T}} - \boldsymbol{F}_{\|\boldsymbol{X_{Tc}}}\right)\right) \frac{\boldsymbol{v_T}}{|\boldsymbol{v_T}|^2} \\ \boldsymbol{F}_{\|\boldsymbol{X_{Tc}}} &= (m_k + m_T)\, \frac{\boldsymbol{d_k}}{dt^2} \\ \boldsymbol{v_T} &= \dot{\gamma} r_B \end{aligned} \tag{3.11}$$

as illustrated in figure 3.7. It is assumed that the velocity of the tether base $\boldsymbol{v_T}$ is substantially smaller than that of the kite and thus the additional motion would have negligible effects on the kite forces, within a single time step iteration.

The velocity of the tether base is computed assuming a constant rotation of the carousel base $\dot{\gamma}$, which the tether is attached to, and the radius of the carousel base r_B.

3.1.3 Model verification

Initial results were obtained for a kite with a stationary tether base, under a regular turn input, based in air as that is what the estimations of lift and drag coefficient in figure 3.4 are based on. Following the kite was modelled under similar conditions with the tether base attached to a rotating carousel as described in section 3.1.2.

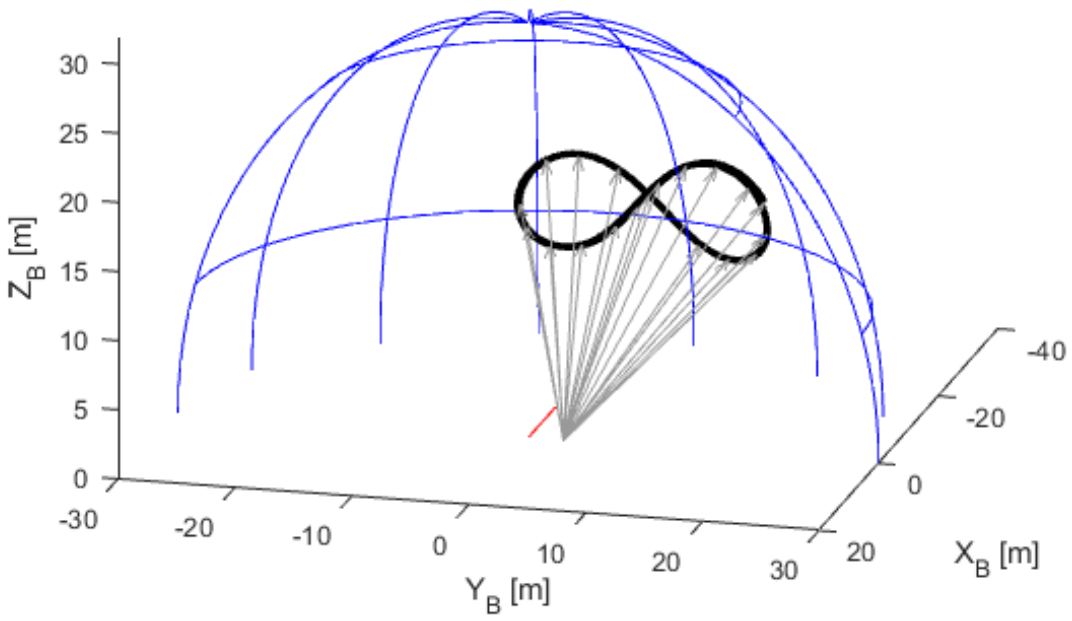

Figure 3.8: Kite flightpath under regular control inputs

Table 3.1: Parameters for initial kite model results

Symbol	Variable	Magnitude	unit
v_{f_r}	Flow velocity	8	m/s
A_k	Kite area	8	m^2
Æ	Kite aspect ratio	4.5	–
l_T	tether length	30	m
ρ_f	flow density	1.225	kg/m^3

3.1.3.1 Stationary kite base

A single kite with a stationary tether base was modelled under regular control inputs similar to the strategy used by Dadd *et.al.* [90]. The resulting flightpath is depicted in figure 3.8. The control inputs used to produce this result and the kite responses are shown in figure 3.9. Figure 3.10, shows the lift, drag and tether tensile forces throughout the simulated time period. It is assumed that the kite is controlled in such a way to keep the angle of attack such that the lift-to-drag ratio is near optimum, resulting in the computed lift force being a factor 3 higher than the drag force. The general input conditions for this case are shown in table 3.1.

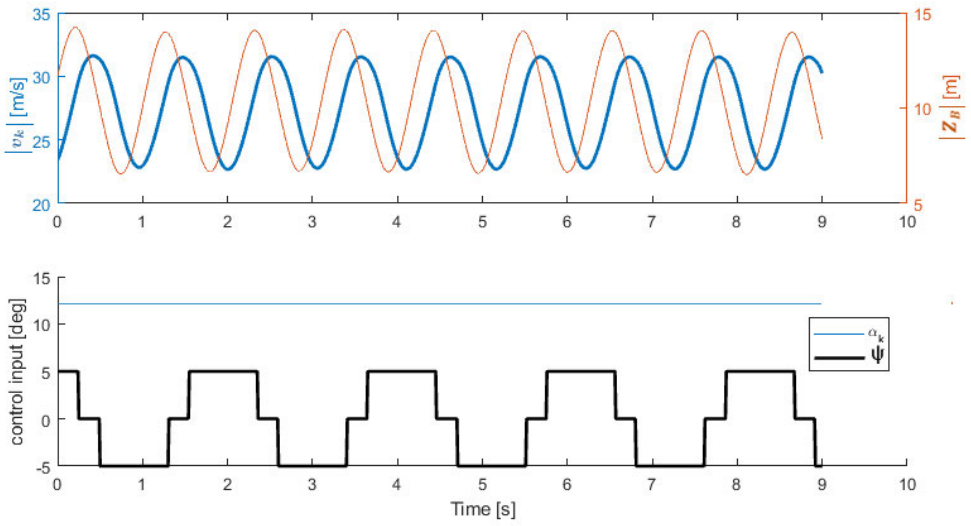

Figure 3.9: Kite controls and responses

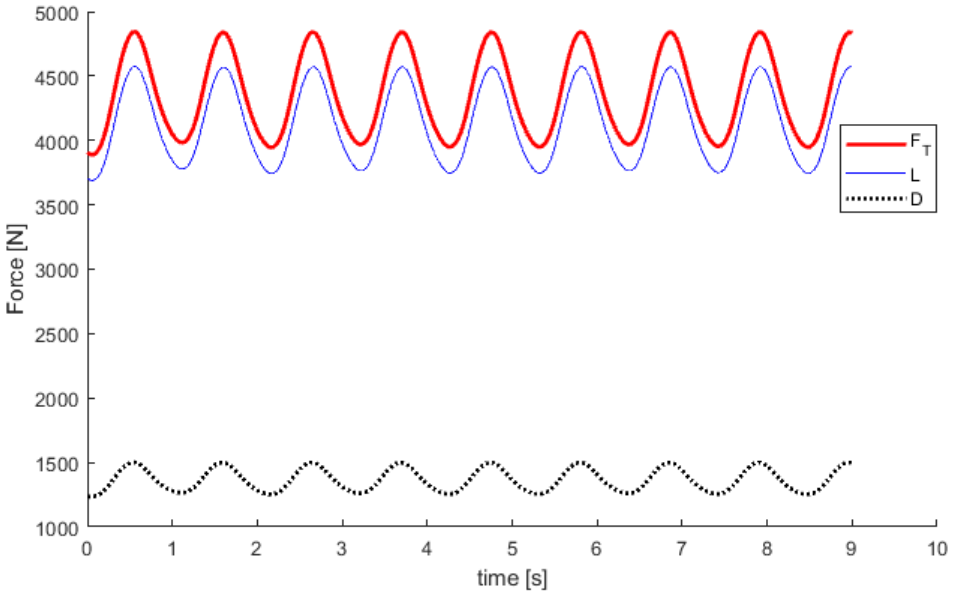

Figure 3.10: Forces due to kite motion

3.1.3.2 Carousel kite base

Adopting a similar control strategy for the moving carousel, as for the stationary kite base, results in a continual figure of eight pattern being flow as shown in figure 3.11. The resulting forces and power in figures 3.12, and 3.14 so that while power is being produced while the tether base is moving downwind, a large amount of power is required to pull the kite upwind. To provide further context it is indicated in figure 3.14 whether

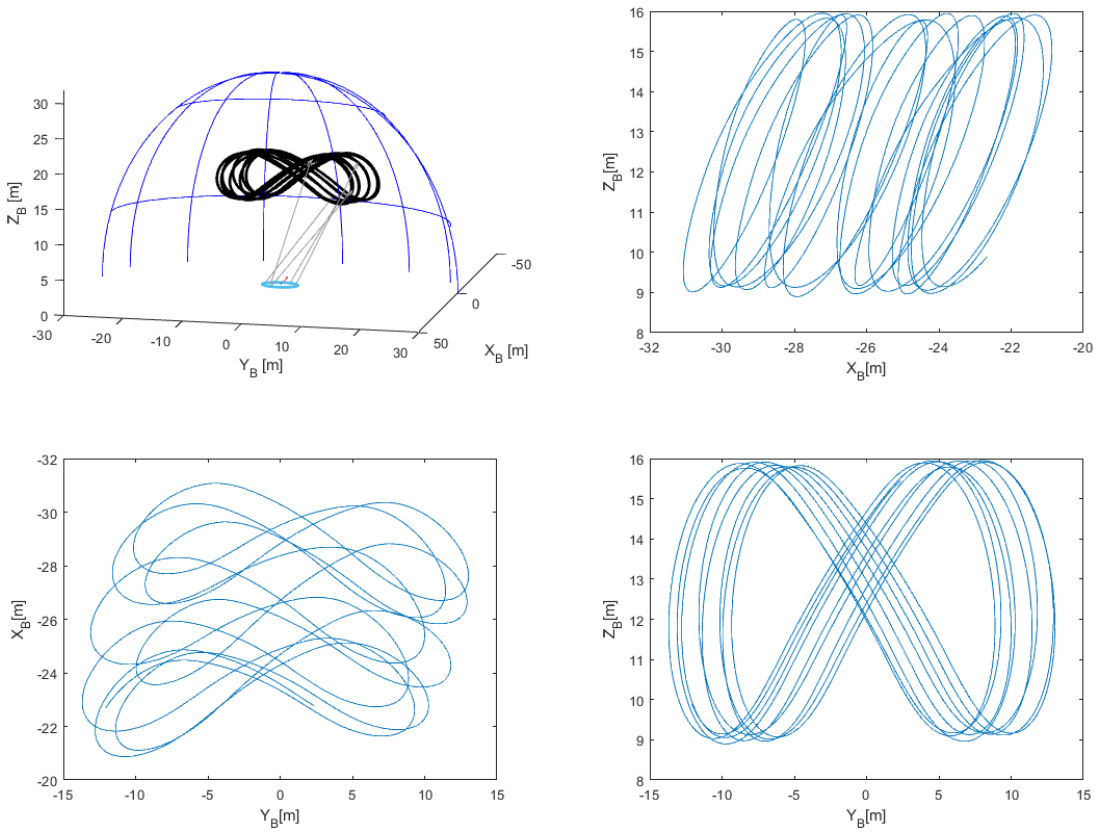

Figure 3.11: Figure 8 flightpath for moving carousel

the kite tether base attached to the carousel is moving up- or downwind. Figure 3.13 shows the controls used to produce this flightpath. The resulting cycle actually averages at -430 W produced; which means this device would require power input to be able to operate. In order to allow for a net power gain, a rough control strategy is introduced such that while the kite is exerting force on on the carousel, i.e. 'pulling', figure 8's are flown in order to maximize kite velocity and consequently force. When the kite is being towed upwind by the carousel, the angle of attack is adjusted to minimize the aerodynamic forces, and the kite is adjusted to fly at a higher altitude, further from the power zone. Additionally, the control input to initiate turns is reduced such that the kite will fly slower. The adjusted flightpath and forces in figures 3.15 and 3.16 respectively, show the result of the adjusted controls shown in figure 3.17. A substantial difference is seen in the power shown in figure 3.18, where while the positive power production remains similar the consumption during the 'towing' phase has reduced substantially. This resulted in a positive net power over a cycle of 660 W, assuming a 90% efficiency converting $\boldsymbol{F_p}$ to electricity.

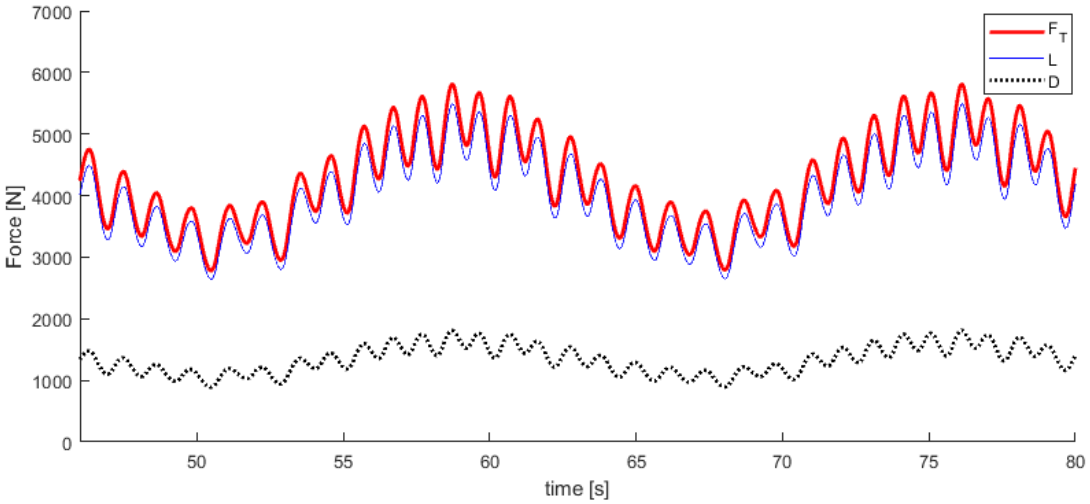

Figure 3.12: Forces due to kite motion for two cycles

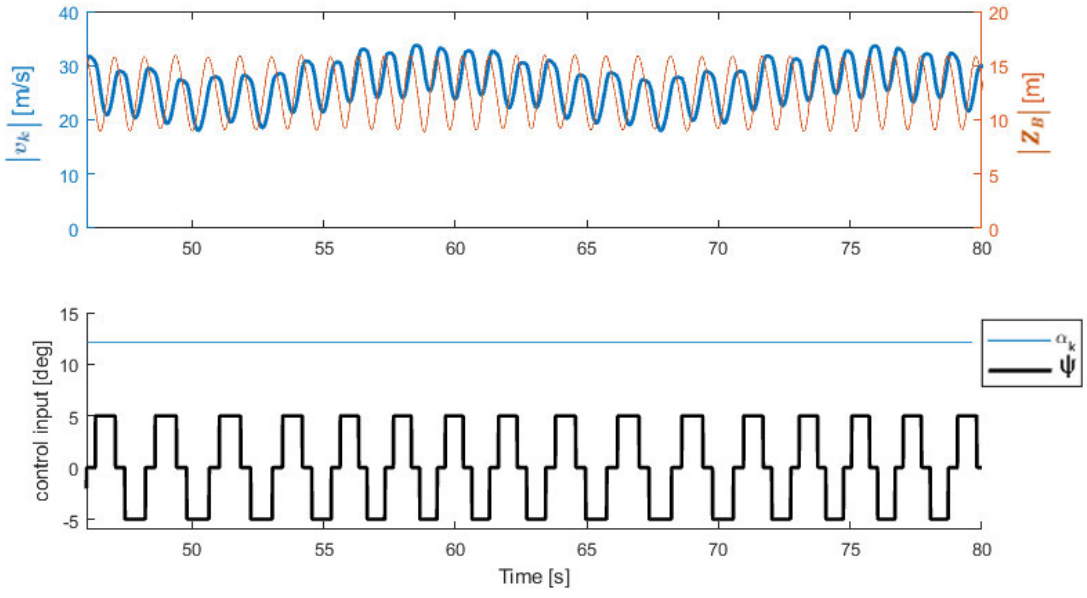

Figure 3.13: Kite controls and responses for two carousel cycles

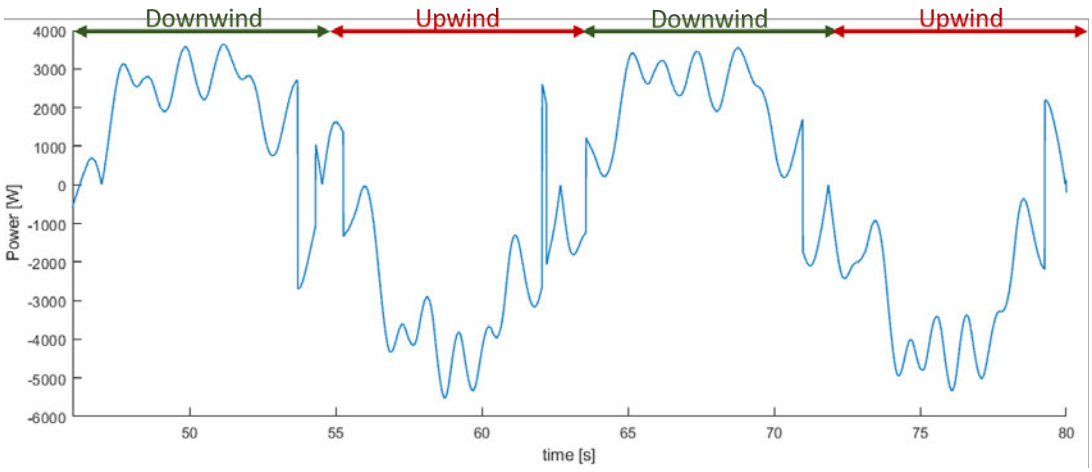

Figure 3.14: Power output for two carousel cycles

The sharp negative peaks in figure 3.18 indicate inefficiencies in transitioning between kite pulling and towing modes. This leaves room for improvement, but does clearly show a net power production with the kite carousel is possible.

Table 3.2: Parameters for initial kite model results

Symbol	Variable	Magnitude	unit
v_{f_r}	Flow velocity	8	m/s
A_k	Kite area	8	m^2
m_k	Kite mass	2.5	kg
Æ	Kite aspect ratio	4.3	–
l_T	tether length	30	m
ρ_f	flow density	1.225	kg/m^3

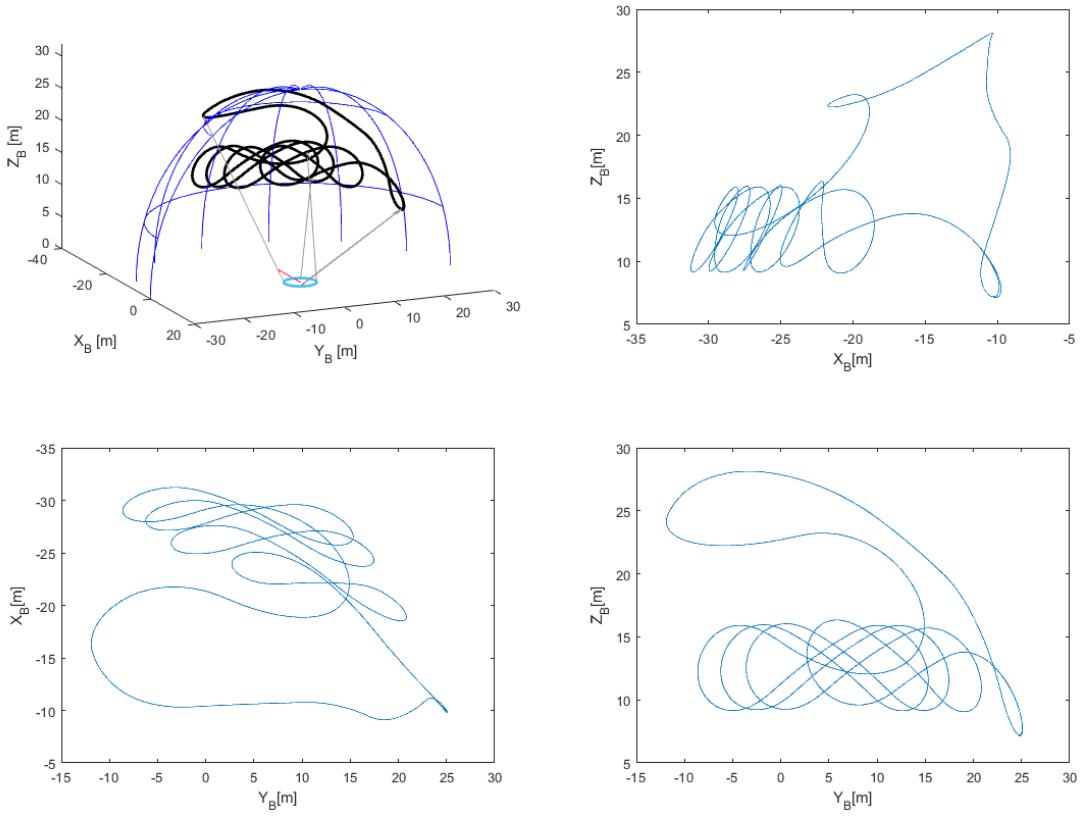

Figure 3.15: kite flightpath under rough control input

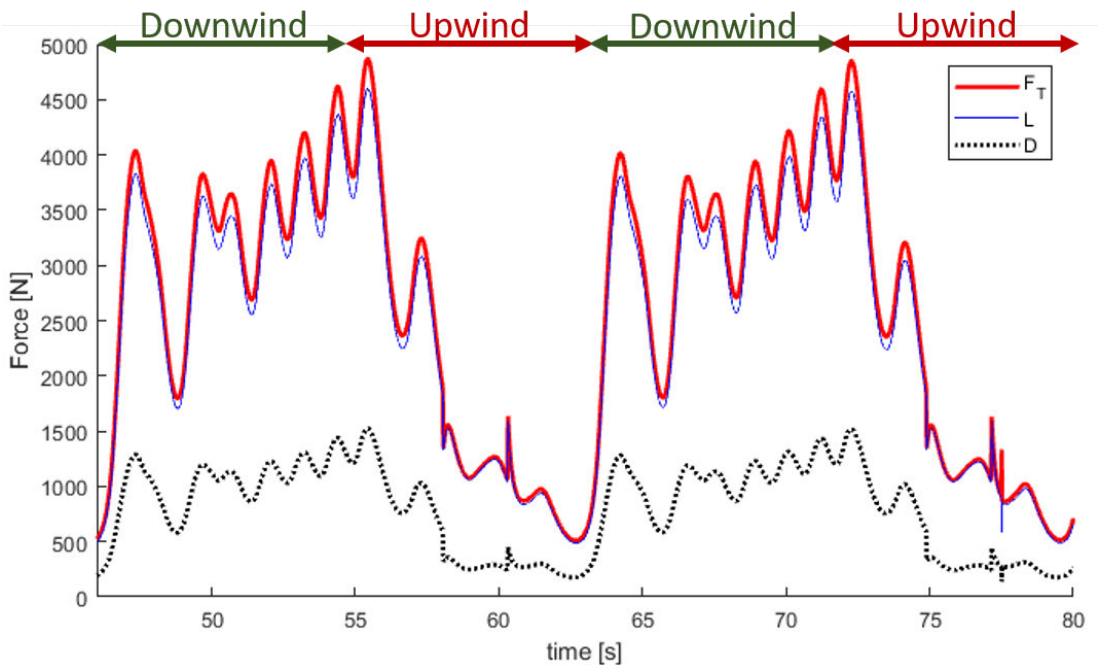

Figure 3.16: Forces due to kite motion for two cycles

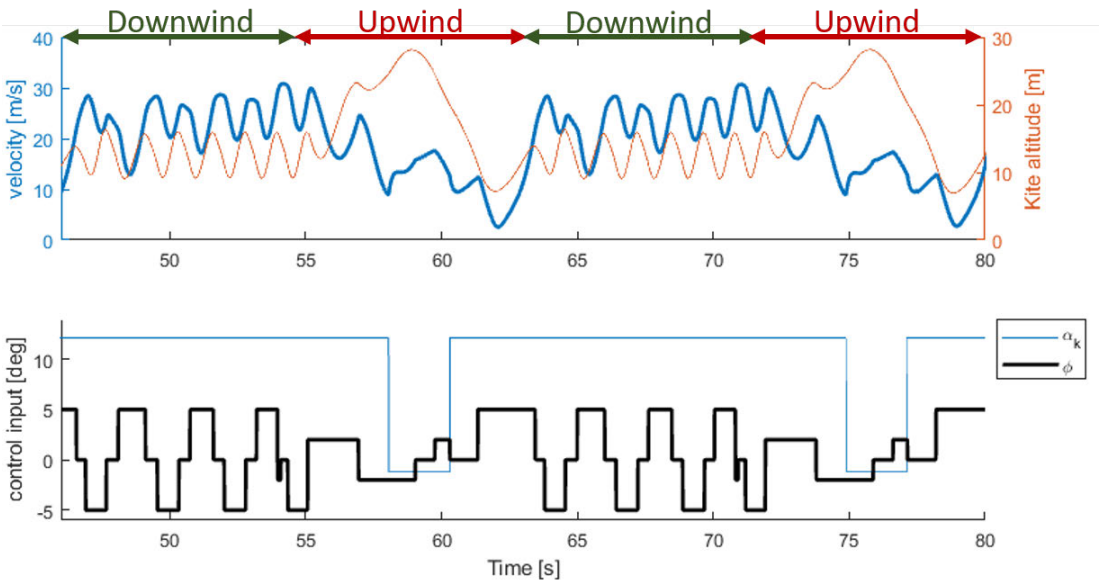

Figure 3.17: Kite controls and responses for two carousel cycles

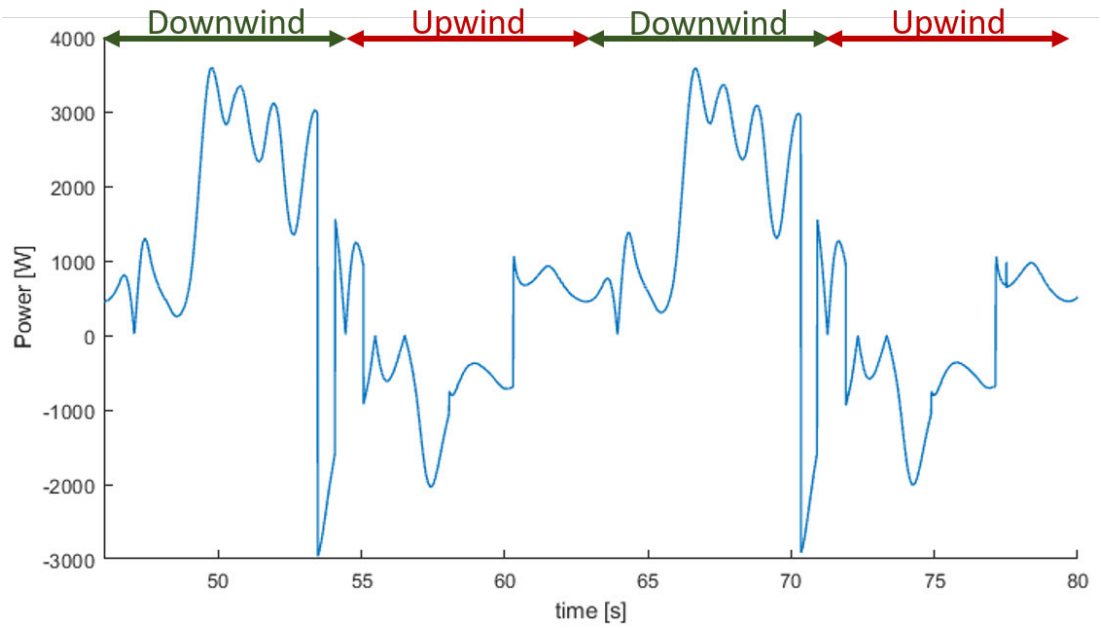

Figure 3.18: Kite controls and responses for two carousel cycles

3.2 State space representation

Here the model is represented as a set of ODEs to increase commputational efficiency with MATLAB and to smooth the way for implementation into optimization software. To simplify equations the system is represented in spherical coordinates as in Fagiano [33], this is described in section 3.2.1.

At this point further elements were included to increase the model accuracy, such as a tether drag contribution and variable aerodynamic coefficient input dependant upon Reynolds number. In doing so, the model can be used to represent a variety of flows including submerged in seawater, and flying through air.

The differential states $\boldsymbol{s}$ describe the kite motion as in:

$$\boldsymbol{u} = \begin{bmatrix} \alpha \\ \psi \end{bmatrix}, \qquad \boldsymbol{s} = \begin{bmatrix} s_1 \\ s_2 \\ s_3 \\ s_4 \\ s_5 \end{bmatrix} = \begin{bmatrix} \theta \\ \phi \\ \gamma \\ \dot{\theta} \\ \dot{\phi} \end{bmatrix}, \qquad \dot{\boldsymbol{s}} = \begin{bmatrix} s_4 \\ s_5 \\ \dot{s}_3 \\ \dot{s}_4 \\ \dot{s}_5 \end{bmatrix} = \begin{bmatrix} \dot{\theta} \\ \dot{\phi} \\ \dot{\gamma} \\ \ddot{\theta} \\ \ddot{\phi} \end{bmatrix} \tag{3.12}$$

These state representations are illustrated in figure 3.19. The states are controlled by adjusting the kite angle of attack(α), and roll angle(ψ). As in section 3.1 these elements change the kite orientation and subsequently the aerodynamic coefficients and forces which determine kite motion. The first time derivative of the state vector, resulting from solving the ODEs is $\dot{\boldsymbol{x}}$.

3.2.1 Coordinate system

In order to simplify the system of equations the coordinate was adjusted to a polar coordinate system as used by Fagiano [2]. All forces and accelerations are computed in a local polar coordinate system represented by $(\boldsymbol{e_\theta}, \boldsymbol{e_\phi}, \boldsymbol{e_T})$ as shown in figure 3.19. While this at first glance appears similar to the kite coordinate system from the previous section; $\boldsymbol{e_\theta}, \boldsymbol{e_\phi}$, and $\boldsymbol{e_T}$ do not depend on kite orientation, but rather its position with respect to the kite carousel and tether angles. In order to switch from the local kite coordinates to the overall global coordinates an intermediate coordinate system is used at the base of the kite tether, also indicated in figure 3.19. The conversion matrix from local to intermediate systems, $\boldsymbol{T_L}$, and from the intermediate to global coordinates, $\boldsymbol{T_G}$

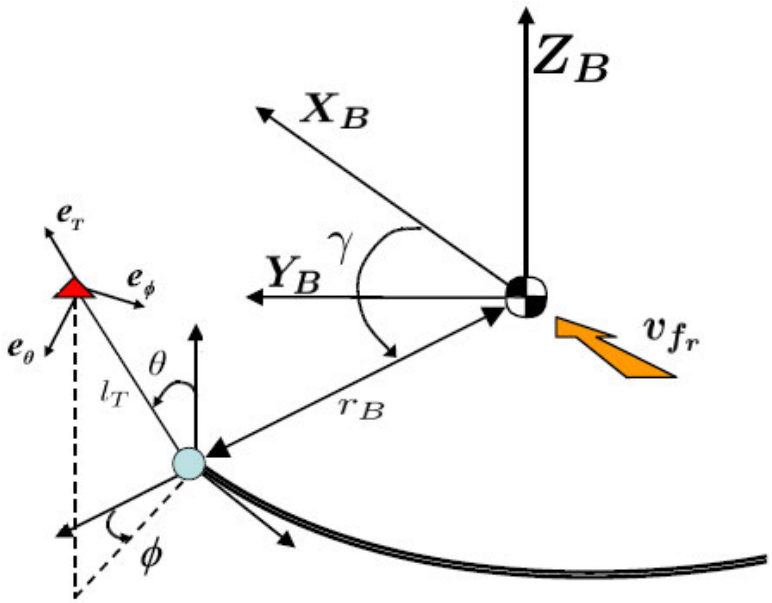

Figure 3.19: Polar coordinate system as represented in Fagiano [2]

are defined as follows:

$$\begin{aligned} \boldsymbol{T_G} &= \begin{bmatrix} \cos(\gamma) & -\sin(\gamma) & 0 \\ \sin(\gamma) & \cos(\gamma) & 0 \\ 0 & 0 & 1 \end{bmatrix} \\ \boldsymbol{T_L} &= \begin{bmatrix} \cos(\theta)\cos(\phi) & -\sin(\phi) & \sin(\theta)\cos(\phi) \\ \cos(\theta)\sin(\phi) & \cos(\phi) & \sin(\theta)\sin(\phi) \\ -\sin(\theta) & 0 & \cos(\theta) \end{bmatrix} \end{aligned} \tag{3.13}$$

These matrices are used to convert all relevant variables computed in the local coordinate system to the overall base reference frame $(\boldsymbol{X_B}, \boldsymbol{Y_B}, \boldsymbol{Z_B})$.

3.2.2 Differential equations

The differential equations describing the kite movement are shown as:

$$\begin{aligned} \ddot{\theta} &= \frac{F_\theta}{m_k l_T} \\ \ddot{\phi} &= \frac{F_\phi}{m_k l_T \sin(\theta)} \end{aligned} \tag{3.14}$$

Note that $\ddot{\gamma}$ is not included here as this is assumed to be zero in this model, as the full component of the tether force in this direction is assumed to be converted to electrical

power. The mass, m_k of the kite includes the added mass. The added mass represents the inertia added to an accelerating body because of the volume of fluid it must displace at moves, acting as additional damping to the system. While this may be negligible when modelling an object moving through air, the change in density when moving to a denser fluid such as water makes this a significant addition to the model. Added mass is approximated by the mass of fluid displaced by a cylinder with the same length and frontal area of the kite [35]. The individual computation of the gravity, aerodynamic, and apparent forces are shown in section 3.2.3

The resultant force components, F_θ, F_ϕ and F_T, along the relevant local coordinate axes are computed through,

$$\begin{aligned} F_\theta &= (\boldsymbol{F_g} + \boldsymbol{F_c} + \boldsymbol{F_{LD}}) \cdot \boldsymbol{e_\theta} \\ F_\phi &= (\boldsymbol{F_g} + \boldsymbol{F_c} + \boldsymbol{F_{LD}}) \cdot \boldsymbol{e_\phi} \\ F_T &= (\boldsymbol{F_g} + \boldsymbol{F_c} + \boldsymbol{F_{LD}}) \cdot \boldsymbol{e_T} \end{aligned} \tag{3.15}$$

The tether component of the resultant force, F_T, is used to compute the power extracted by the generator to keep the generator rotating at a constant velocity,

$$P = -\dot{\gamma} r_B F_T \sin\theta \sin\phi \tag{3.16}$$

3.2.3 Forces

The forces used to compute kite behaviour consist of those due to gravity, centrifugal, and aerodynamic forces. The computation of each these forces is given in this section.

3.2.3.1 Gravity

The computation of the gravity force enacting on the kite is computed through:

$$\boldsymbol{F_g} = \left(m_k + \frac{1}{4}\rho_T \pi (5 l_T) d_T^2\right) g \begin{bmatrix} \sin(\theta) \\ 0 \\ \cos(\theta) \end{bmatrix} \tag{3.17}$$

As previously mentioned it is assumed that both the kite and tether mass is applied at the point mass at the end of the tether. It is noted that this is not an entirely accurate representation due to the mass of the tether being distributed along the tether, as discussed in section 3.1.1. The tether mass is computed using $5l_T$, to account for the multiple tether lines used to maintain the inflatable kite shape.

3.2.3.2 Centrifugal force

Since the local coordinate system is not an inertial frame of reference, the centrifugal force is computed. This apparent force is evaluated as:

$$\boldsymbol{F_c} = m_k \begin{bmatrix} \left(\dot{\gamma}+\dot{\phi}\right)^2 l_T \sin(\theta)\cos(\theta) + \dot{\gamma}^2 r_B \cos(\theta)\cos(\phi) \\ -2l_T\left(\dot{\gamma}+\dot{\phi}\right)\dot{\theta}\cos(\theta) - \dot{\gamma}^2 r_B \sin(\phi) \\ l_T\left(\dot{\gamma}+\dot{\phi}\right)^2 \sin^2(\theta) + \dot{\gamma}^2 r_B \sin(\theta)\cos(\phi) + l_T\dot{\theta}^2 \end{bmatrix} \tag{3.18}$$

under the assumption that carousel velocity and tether length remain constant ($\ddot{\gamma}=0, \dot{r}=0$). In this instance the contribution of the tether mass is not included as in reality the distributed nature of this mass would further reduce its contribution, but again would require additional computational power to compute. As such at this time the centrifugal force is computed using m_k.

It is noted that due to the low kite mass contributing to the gravity and apparent forces on the kite remain small compared to the aerodynamic forces, and could be neglected in favour of reduced computational power requirements.

3.2.3.3 Aerodynamic forces

The resultant aero dynamic force is computed by summing the lift, $\boldsymbol{L}$, and drag forces, $\boldsymbol{D_k}$ and $\boldsymbol{D_t}$, as in:

$$\boldsymbol{F_{LD}} = \boldsymbol{L} + \boldsymbol{D_k} + \boldsymbol{D_t} \tag{3.19}$$

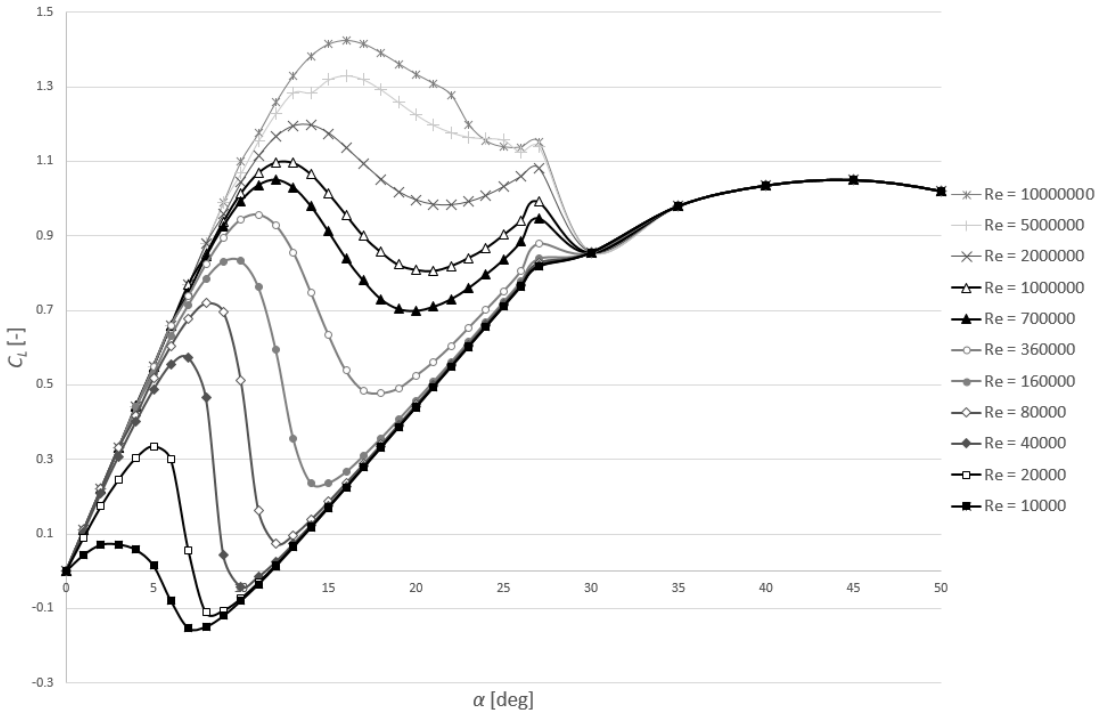

Figure 3.20: NACA0015 lift coefficients dependant on α and Reynolds number as per Sheldahl [6]

with,

$$\begin{aligned} \boldsymbol{L} &= -\frac{1}{2} C_L A_k \rho_f \left|\boldsymbol{v_a}\right|^2 \cdot \boldsymbol{z_w} \\ \boldsymbol{D_k} &= -\frac{1}{2} C_D A_k \rho_f \left|\boldsymbol{v_a}\right|^2 \cdot \boldsymbol{x_w} \\ \boldsymbol{D_t} &= -\frac{1}{8} \rho_f C_{D,T} d_T (5 l_T) \cos(\Delta\alpha) \left|\boldsymbol{v_a}\right|^2 \boldsymbol{x_w} \end{aligned} \tag{3.20}$$

and,

$$\Delta\alpha = \arcsin\left(\frac{\boldsymbol{e_T} \cdot \boldsymbol{v_a}}{|\boldsymbol{v_a}|}\right) \tag{3.21}$$

The tether drag coefficient $C_{D,T}$ is set to 1.1, as it is assumed to be a cylinder with length $5l_T$ and diameter d_T. A factor of 5 is applied to the length of the tether to account for the multiple steering and bridle lines that make up the tether construction. The apparent angle of attack $\Delta\alpha$ is measured as the angle between the apparent wind $\boldsymbol{v_a}$ and the plane perpendicular to the tether, as shown in equation 3.21. In order to further reduce model complexity tether drag can be incorporated as 30 % increase in kite drag as shown in by Paiva and Fontes [31].

The lift and drag coefficients, C_L and C_D respectively result from a lookup table

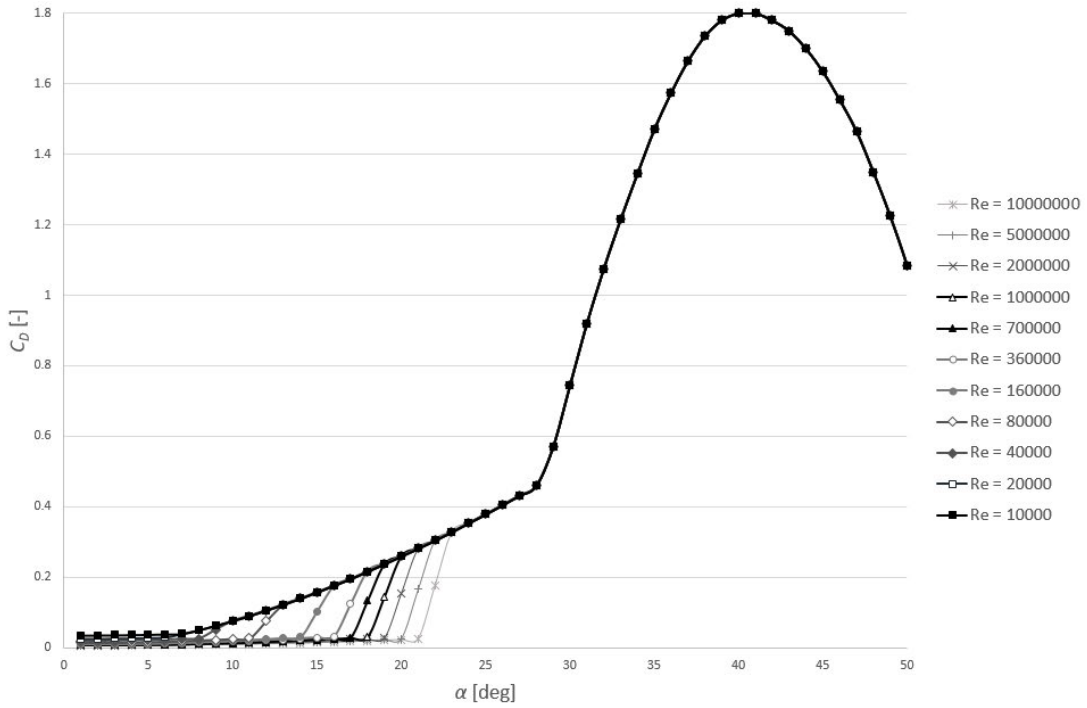

Figure 3.21: NACA0015 drag coefficients dependant on α and Reynolds number as per Sheldahl [6]

produced from data by Sheldahl [6]; which provides the aerodynamic coefficients for a NACA 0015 airfoil at various Reynolds numbers, for a full range of α. Figures 3.20 and 3.21 show the data used to produce the lookup tables. By determining the aerodynamic coefficients based on the Reynolds number the model can be used to represent cases in a range of velocity and fluids.

The Reynolds number is computed as a function of the relative velocity of the fluid with respect to the kite, v_a, the kite chord c_k, and the kinematic viscosity, ν of the fluid; as follows:

$$Re = \frac{c_k v_a}{\nu} \tag{3.22}$$

For an air-based kite as described in the previous section with $\nu = 14.88$ m^2/s, $c_k = 1.5$ m and 10 m/s $< v_a <$ 30 m/s; the Reynolds number ranges from 1×10^6 to 3×10^6. From figure 3.20 this shows that at angles of attack of $\alpha > 10°$ the lift coefficient would jump as the apparent kite velocity varies. The velocity dependant effect on the drag coefficient appears at higher angles of attack where the C_D, α-curves only deviate at $\alpha \approx 18°$. As the range of v_a increases, so does the effect on the aerodynamic coefficients at higher angles of attack. In reality this effect is mitigated by the fact that as kite

velocity increases, not only does the apparent velocity increase but α reduces.

3.2.4 Incoming flow

The apparent flow velocity seen by the kite is determined by the kite velocity and the onset flow speed, which varies dependant on height as per the logarithmic profile [87], computed in the global coordinate system, as per equations 3.2, and 3.1; where the kite height z_k is determined as:

$$z_k = l_T \cos(\theta) \tag{3.23}$$

The incoming wind is transposed to the kite local coordinate system through:

$$\boldsymbol{v_{f_k}}(\boldsymbol{s}) = \boldsymbol{T_L}'(\boldsymbol{s})\, \boldsymbol{T_G}'(\boldsymbol{s})\, \boldsymbol{v_{f_{k,B}}} \tag{3.24}$$

The kite velocity, $\boldsymbol{v_k}$, expressed as in equation 3.25. Finally the apparent velocity used to compute the lift and drag forces is computed through:

$$\boldsymbol{v_k} = \begin{bmatrix} \dot{\theta} l_T + \dot{\gamma} \cos(\theta) \sin(\phi) r_B \\ \left(\dot{\phi} + \dot{\gamma}\right) l_T \sin(\theta) + \dot{\gamma} \cos(\phi) r_B \\ \dot{\gamma} r_B \sin(\theta) \sin(\phi) r_B \end{bmatrix} \tag{3.25}$$

3.2.5 Kite coordinate system definition

The vectors along which the lift and drag forces act are determined by the apparent flow vector and the kite position. Drag is expressed in the kite point mass parallel to the incoming apparent flow. Lift is applied perpendicular to this vector, but is also perpendicular to the kite surface.

The tangential flow axis, $\boldsymbol{x_f}$, is used to determine the orientation of the drag force and is computed as:

$$\boldsymbol{x_f} = \frac{-\boldsymbol{v_a}}{|\boldsymbol{v_a}|} \tag{3.26}$$

The lift is presumed to act perpendicular to the apparent flow, and kite orientation. To this end the kite pitching axis, $\boldsymbol{y_{k\perp e_T}}$ is computed by:

$$\begin{aligned} \boldsymbol{x_{k\perp e_T}} &= \frac{\boldsymbol{x_w} - \boldsymbol{e_T}\left(\boldsymbol{e_T} \cdot \boldsymbol{x_w}\right)}{\left|\boldsymbol{x_w} - \boldsymbol{e_T}\left(\boldsymbol{e_T} \cdot \boldsymbol{x_w}\right)\right|} \\ \boldsymbol{y_{k\perp e_T}} &= \boldsymbol{x_{k\perp e_T}} \times \boldsymbol{e_T} \end{aligned} \tag{3.27}$$

where $\boldsymbol{y_{k\perp e_T}}$ is rotated around the kite roll axis, $\boldsymbol{x_{k\perp e_T}}$, by the turning angle ψ using the Rodrigues rotation formula, similar to Paiva and Fontes [78, 91];

$$\begin{aligned} \boldsymbol{y_k} = \; & \boldsymbol{y_{k\perp e_T}} \cos(\psi) \\ & + \left(\boldsymbol{x_{k\perp e_T}} \times \boldsymbol{y_{k\perp e_T}}\right) \sin(\psi) \\ & + \boldsymbol{x_{k\perp e_T}} \left(\boldsymbol{x_{k\perp e_T}} \cdot \boldsymbol{y_{k\perp e_T}}\right) \left(1 - \cos(\psi)\right) \end{aligned} \tag{3.28}$$

Finally the z-axis for the flow coordinate system is computed with:

$$\boldsymbol{z_f} = \boldsymbol{x_f} \times \boldsymbol{y_k} \tag{3.29}$$

Because $\boldsymbol{z_f}$ is downward facing and $\boldsymbol{x_f}$ faces into the wind a negative is added to the lift and drag calculations as seen in equation 3.20.

3.2.6 Controls

The kite is controlled through applying a roll and pitch throughout the simulation. In order to control the forces on the kite a desired angle of attack is assigned. It is assumed the kite is pitched appropriately such that this angle is met, a limit of 45 deg is set for allowed adjustment. As the angle of attack is directly related to the lift coefficient in the presumed case, the lift coefficient is effectively assigned.

To allow side ways motion of the kite the angle ψ is introduced. This angle represents a roll of the kite around its axis $\boldsymbol{x_{k\perp e_r}}$ this rotates the axis along which lift is applied and thus causes the kite to accelerate in that direction.

While in the initial model a version of figure 8's were flown to produce a net positive power throughout a cycle. At this point a smooth profile is produced to show its potential. In this way reducing the restrictions on producible flightpaths as with a

figure 8 type method.

3.2.7 Model Verification

For the purpose of producing a reference flightpath for optimization in chapter 4, an initial flightpath was created and is displayed in figure 3.22. The control applied is shown in figure 3.23, with the resulting differential states in figure 3.24. The relevant inputs used to initialise the system are shown in table 3.3.

Table 3.3: Parameters for carousel model results

Symbol	Variable	Magnitude	unit
v_{f_r}	Flow velocity	8	m/s
A_k	Kite area	10	m^2
l_T	tether length	30	m
ρ_f	flow density	1.225	kg/m^3
θ_0	starting azimuth angle	0.17	rad
ϕ_0	starting sweep angle	-0.79	rad
γ_0	starting carousel rotation angle	1.57	rad
$\dot{\theta}_0$	starting azimuth velocity	0	rad/s
$\dot{\phi}_0$	starting sweep velocity	0	rad/s
$\dot{\gamma}_0$	carousel angular velocity	0.52	rad/s

In order to provide a starting point, an initial flightpath is described and provided through a matrix providing all kite states for the 12 s period. The initial flightpath, controls used, and resulting outputs as shown in figures 3.22, 3.23, 3.24, and 3.25. The control input required to create the reference flightpath was obtained through an iterative process of manual control inputs in order to develop a periodic flightpath. The trajectory followed from modelling the kite over time as it was subjected to various adjustments to roll angle and α.

It is noted that the kite velocity increases up to 75 m/s during the initial dive into the powerzone, which is substantially high. One of the proposed benefits of the carousel design is a more uniform power generation. The results of this cycle shows a substantial

peak during the kite dive. It is proposed that including multiple kites on a single carousel would work to smooth out the overall power output throughout a cycle. However, even with the single kite this setup shows an overall power potential of 1 kW. This is again largely due to the high kite velocity during the initial dive.

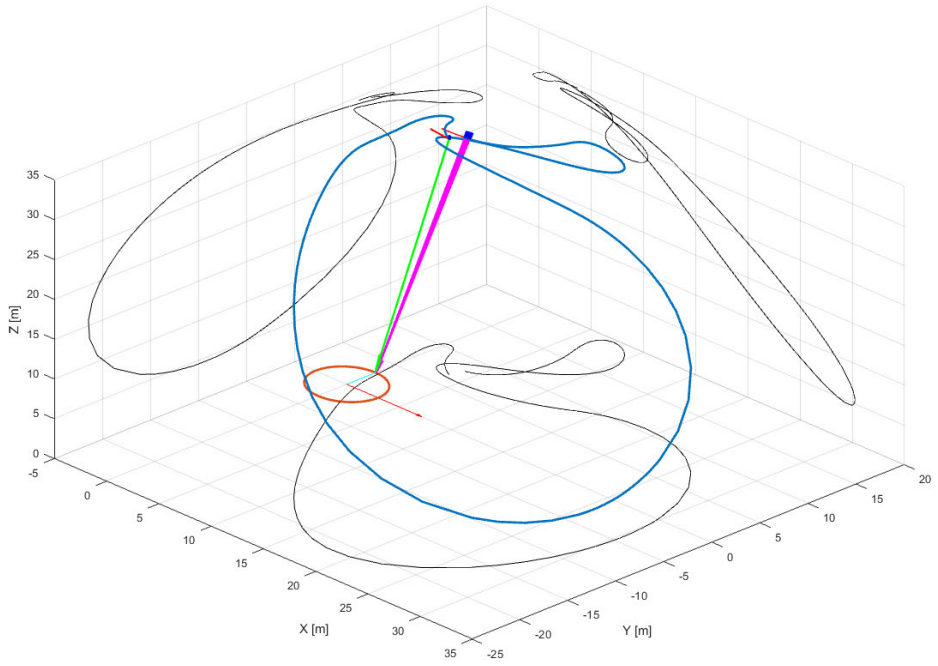

Figure 3.22: Flightpath due to controls applied, with start/end position indicated.

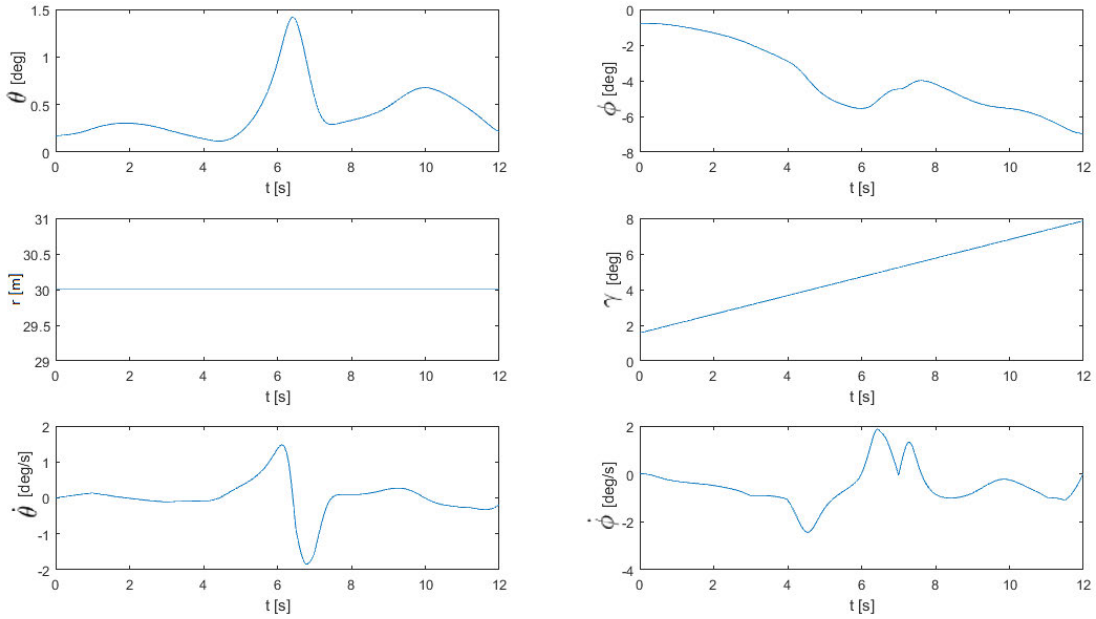

Figure 3.24: Differential states describing baseline flightpath

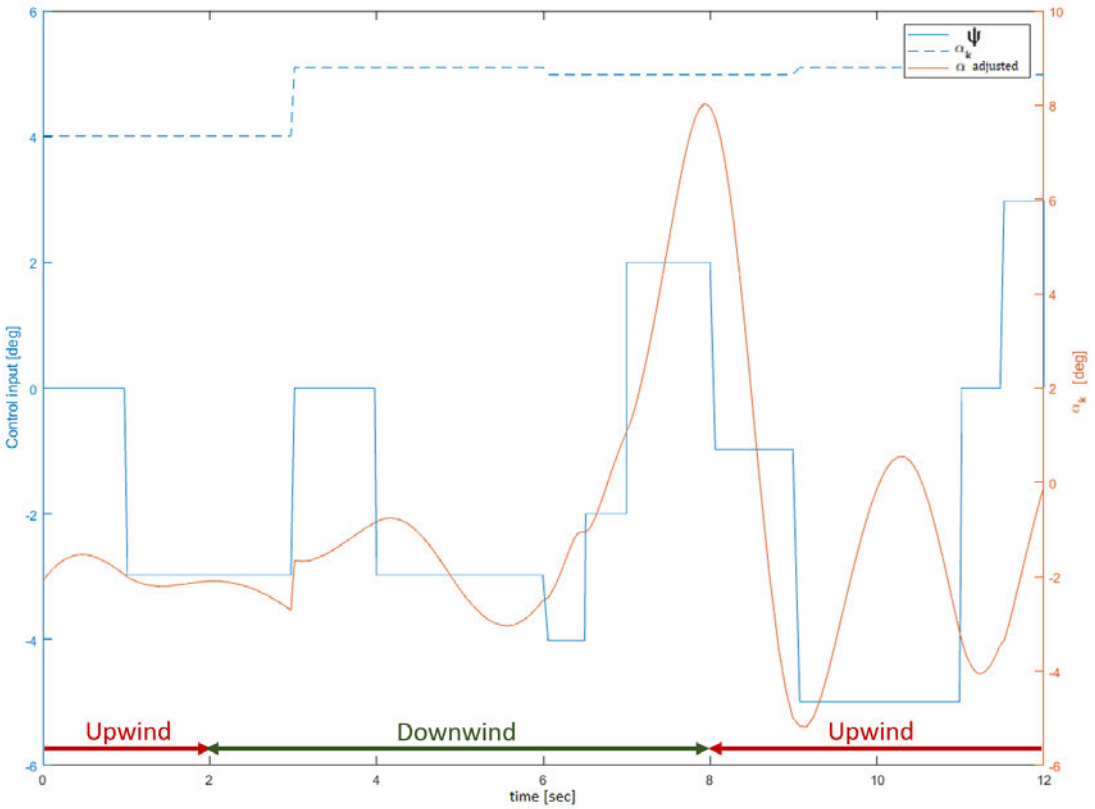

Figure 3.23: Controls to produce baseline flightpath.

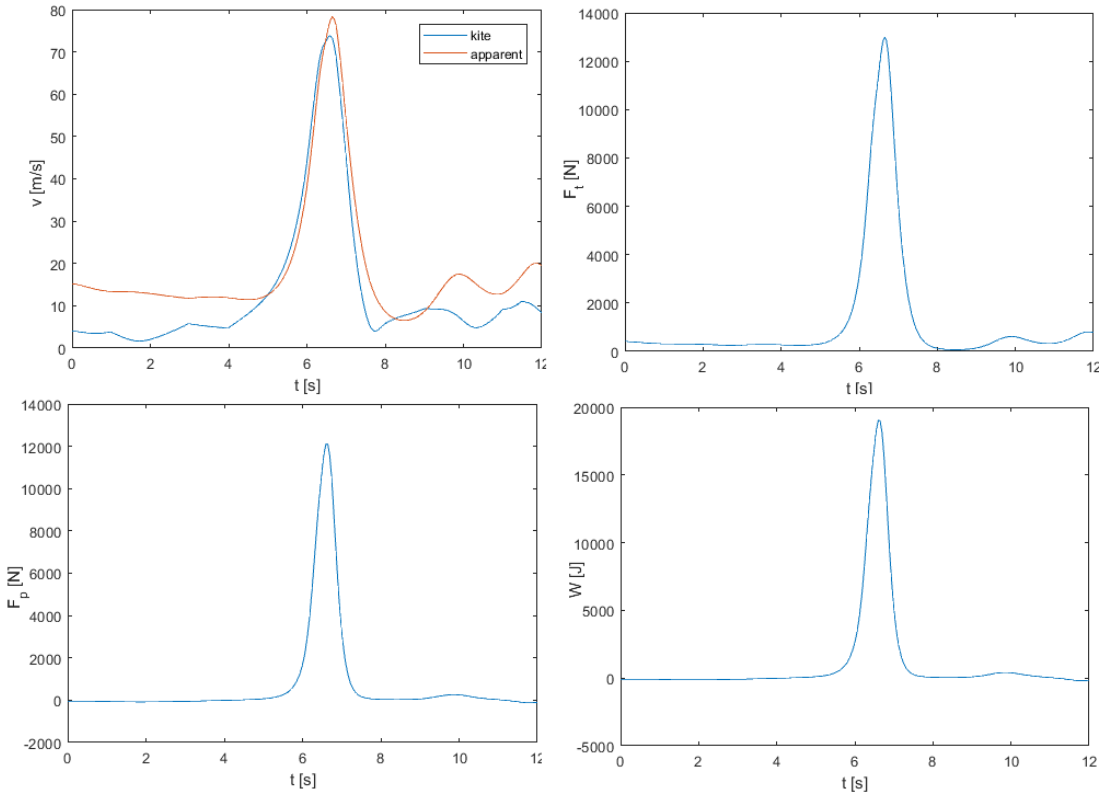

Figure 3.25: Resulting outputs attributed to baseline flightpath

3.3 Flightpath optimization

This section describes the process used to optimize the state space model presented in section 3.2.

3.3.1 Solution technique

Up to this point, the flightpaths were solved by discretizing the cycle into a set of first order differential equations which were solved for assuming linearity between timesteps. As such the timestep was chosen to be small enough to allow for smooth solutions. While this method is computationally effective, it becomes less accurate as the model is expanded to include aspects where assuming linearity introduces more inaccuracies. As mentioned in the literature review, a solution software called ACADO is used to solve the optimization problem presented here. ACADO allows for a variety of solution techniques to be applied to solve for an optimal control problem. In order to achieve this the function to be solved must be smooth and sufficiently often differentiable. It

was decided to use the included explicit Runge-Kutta integrator of the order 4/5. For discretization a multiple shooting method is used. In order for the problem to remain differentiable, a timestep was chosen to be small enough whilst still allowing for the optimization to be performed on a regular computer. In order for the effect of timestep adjustment to remain minimal the controllable variable was set to the rate of change of the roll and pitch angles, with a maximum rad/s limit.
This technique relies on a flightpath initialization which was achieved through manual control adjustments made to the model to find an initial flyable flightpath. In order to allow for flexibility around this flightpath an iterative process was used to allow for promising outcomes to further develop to minimize results representing local minimums found for the optimization problem. Despite efforts made, further efforts would be required to ensure that the solutions found are truly global optimizations and fully independent from the flightpath initialization.

Assumptions The optimization problem is a continuation of the model discussed in section 3.2. However the optimization software used requires a fully differentiable system to operate. As such the computation of the aerodynamic coefficients is reduced from a lookup table of known parameters to a single equation. Similarly the gravity and centrifugal forces are excluded to further reduce model complexity. Although the tether drag component was taken into account. In order to allow consistent handling of the control parameters, the control has been altered to fix the change rate of the roll angle and angle of attack. As such the roll angle and angle of attack are added to the state vector, allowing them to develop according to the control input.

3.3.2 Optimization problem formulation

The differential states $\boldsymbol{s}(t)$ and controls $\boldsymbol{u}(t)$ defined for the optimization problem are as follows:

$$\boldsymbol{u}(t) = \begin{bmatrix} \dot{\alpha}(t) \\ \dot{\psi}(t) \end{bmatrix}, \qquad \boldsymbol{s}(t) = \begin{bmatrix} s_1(t) \\ s_2(t) \\ s_3(t) \\ s_4(t) \\ s_5(t) \\ s_6(t) \\ s_7(t) \end{bmatrix} = \begin{bmatrix} \theta(t) \\ \phi(t) \\ \gamma(t) \\ \dot{\theta}(t) \\ \dot{\phi}(t) \\ \alpha(t) \\ \psi(t) \end{bmatrix}, \qquad \dot{\mathbf{s}}(t) = \begin{bmatrix} s_4(t) \\ s_5(t) \\ \dot{s}_3(t) \\ \dot{s}_4(t) \\ \dot{s}_5(t) \\ u_1(t) \\ u_2(t) \end{bmatrix} = \begin{bmatrix} \dot{\theta}(t) \\ \dot{\phi}(t) \\ \dot{\gamma} \\ \ddot{\theta}(t) \\ \ddot{\phi}(t) \\ \dot{\alpha}(t) \\ \dot{\psi}(t) \end{bmatrix} \tag{3.30}$$

The change in control variables $\boldsymbol{u}(t)$, and added state variables, $s_6(t)$ and $s_7(t)$, for the kite angle of attack and roll, are shown. These changes aside the states are identical to those in equation 3.12, however it is highlighted here that they are all time dependant, except for $\dot{\gamma}$ which is assigned to be constant. The state representations are illustrated in figure 3.19. The controls represent change in the angle of attack(α), and roll angle(ψ). This was chosen to prevent unrealistic control inputs when reducing timestep size for the optimization sequence. The first time derivative of the state vector, $\dot{\mathbf{s}}(t)$, is also represented in equation 3.30.

These vectors define the kite position and orientation for a full carousel period. The

optimization problem solved is defined by the cost function:

$$\min_{\boldsymbol{u}(t)} \quad \mathcal{J}(\boldsymbol{u}(t)) \;:=\; \int_0^{t_e} -\frac{P\left(\boldsymbol{u}(t),\boldsymbol{s}(t)\right)}{t_e}\mathrm{d}t.$$

s.t.

$$\dot{\mathbf{s}}(t) := \begin{cases} s_4(t) = \dot{\theta}(t), & \theta(t_0) = \theta_0 \;\; \dot{\theta}(t_0) = \dot{\theta}_0 \\ s_5(t) = \dot{\phi}(t), & \phi(t_0) = \phi_0 \;\; \dot{\phi}(t_0) = \dot{\phi}_0 \\ \dot{s_3}(t) = \dot{\gamma}(t), & \gamma(t_0) = \gamma_0 \;\; \dot{\gamma}(t_0) = \dot{\gamma}_0 \\ \dot{s}_4(t) = \ddot{\theta}(t) = \frac{F_\theta(\boldsymbol{u}(t),\boldsymbol{s}(t))}{m_k l_T}, & \theta(t_0) = \theta_0 \\ & \dot{\theta}(t_0) = \dot{\theta}_0 \\ \dot{s}_5(t) = \ddot{\phi}(t) = \frac{F_\phi(\boldsymbol{u}(t),\boldsymbol{s}(t))}{m_k l_T \sin(\theta(t))} & \phi(t_0) = \phi_0 \\ & \dot{\phi}(t_0) = \dot{\phi}_0 \\ \dot{u_1}(t) = \dot{\alpha}(t), & \alpha(t_0) = \alpha_0 \;\; \dot{\alpha}(t_0) = \dot{\alpha}_0 \\ \dot{u_2}(t) = \dot{\psi}(t), & \psi(t_0) = \psi_0 \;\; \dot{\psi}(t_0) = \dot{\psi}_0 \end{cases} \tag{3.31}$$

This cost function maximizes the net power output over a period of time from 0 to t_e. The termination time is determined by the carousel angular velocity, $\dot{\gamma}$, and the carousel radius, r_c; as $t_e = \dot{\gamma}/2\pi r$. When the kite is being pulled upstream this would show as a negative power output at that instance and would detract from the net power. The net power is computed by integrating the power function:

$$P\left(\boldsymbol{u}(t),\boldsymbol{s}(t)\right) = -\dot{\gamma} r_c F_T\left(\boldsymbol{u}(t),\boldsymbol{s}(t)\right)\sin\left(\theta(t)\right)\sin\left(\phi(t)\right) \tag{3.32}$$

over time. The kite mass m_k used here is the sum of the physical kite mass, and the added mass due to the fluid through which it moves. To allow for longer tether lengths, here the upper third of the tether mass, and added mass, is included as well.

The cost function is optimized subject to a number of constraints. The path constraints must be satisfied at each point throughout the optimizations. These concern elevation range of the kite z_{max} and z_{min} which determines the allowable θ; and the

limits to the control angles α and ψ. Similarly constraints are applied to the allowable control inputs $\dot{\alpha}$ and $\dot{\psi}$, to ensure that the kite control input is independent from the timestep used to solve this optimization problem These constraints are shown as:

Path constraints $\forall t \in [t_0, t_e]$

$$\begin{aligned} z_{\max}/l_T \leq \cos(\theta(t)) &\leq z_{\min}/l_T \\ \alpha_{\min} \leq \quad \alpha(t) \quad &\leq \alpha_{\max} \\ \psi_{\min} \leq \quad \psi(t) \quad &\leq \psi_{\max} \end{aligned} \tag{3.33}$$

Input bounds $\forall t \in [t_0, t_e]$

$$\begin{aligned} \dot{\alpha}_{\min} \leq \dot{\alpha}(t) \leq \dot{\alpha}_{\max} \\ \dot{\psi}_{\min} \leq \dot{\psi}(t) \leq \dot{\psi}_{\max} \end{aligned} \tag{3.34}$$

Finally a number of terminal constraints are applied to ensure a periodic result. This simply assures that the initial kite position and orientation is equal to the final kite position and orientation. The only exception here is for γ, which must complete a full circuit and thus have moved 2π ahead. These constraints ensure that the flightpath found is repeatable over time and are defined as follows:

Terminal constraints

$$\begin{aligned} \theta(t_0) &= \theta(t_e) & \dot{\theta}(t_0) &= \dot{\theta}(t_e) \\ \phi(t_0) &= \phi(t_e) & \dot{\phi}(t_0) &= \dot{\phi}(t_e) \\ \gamma(t_0) &= \gamma(t_e) - 2\pi & & \\ \alpha(t_0) &= \alpha(t_e) & \psi(t_0) &= \psi(t_e) \end{aligned} \tag{3.35}$$

Considering this cost function and the corresponding input, path, and terminal constraints; The dynamic optimization problem is solved by identifying the best control profile that maximizes performance while ensuring all constraints are satisfied.

3.3.2.1 Definition of forces

At this point only aerodynamic forces are considered, which reduces equation 3.15 to equation 3.36. In this case the model is reduced to consider only the aerodynamic forces, as they are the dominant contributing factors to kite behavior. The optimization problem is computed in the local coordinate system $(\boldsymbol{e_\theta}, \boldsymbol{e_\phi}, \boldsymbol{e_T})$, with the resultant force computed as follows:

$$\boldsymbol{F}\left(\boldsymbol{u}(t), \boldsymbol{s}(t)\right) = \begin{bmatrix} F_\theta\left(\boldsymbol{u}(t), \boldsymbol{s}(t)\right) \\ F_\phi\left(\boldsymbol{u}(t), \boldsymbol{s}(t)\right) \\ F_T\left(\boldsymbol{u}(t), \boldsymbol{s}(t)\right) \end{bmatrix}. \tag{3.36}$$

The aerodynamic forces are computed as in section 3.2, equation 3.20; through the following equation:

$$\boldsymbol{F}\left(\boldsymbol{u}(t), \boldsymbol{s}(t)\right) = \boldsymbol{L}\left(\boldsymbol{u}(t), \boldsymbol{s}(t)\right) + \boldsymbol{D_k}\left(\boldsymbol{u}(t), s(t)\right) + \boldsymbol{D_t}\left(\boldsymbol{s}(t)\right) \tag{3.37}$$

with,

$$\begin{aligned} \boldsymbol{L}\left(\boldsymbol{u}(t), \boldsymbol{s}(t)\right) &= -\frac{1}{2} C_L(\boldsymbol{u}(t)) A_k \rho_f \left|\boldsymbol{v_a}\left(\boldsymbol{s}(t)\right)\right|^2 \boldsymbol{z_f}\left(\boldsymbol{u}(t), \boldsymbol{s}(t)\right) \\ \boldsymbol{D_k}\left(\boldsymbol{u}(t), \boldsymbol{s}(t)\right) &= -\frac{1}{2} C_D(\boldsymbol{u}(t)) A_k \rho_f \left|\boldsymbol{v_a}\left(\boldsymbol{s}(t)\right)\right|^2 \boldsymbol{x_f}\left(\boldsymbol{s}(t)\right) \\ \boldsymbol{D_t}\left(\boldsymbol{s}(t)\right) &= -\frac{1}{8} \rho_f C_{D,T} d_T (5 l_T) \cos(\Delta\alpha\left(\boldsymbol{s}(t)\right)) \left|\boldsymbol{v_a}\left(\boldsymbol{s}(t)\right)\right|^2 \boldsymbol{x_f}\left(\boldsymbol{s}(t)\right) \\ \Delta\alpha\left(\boldsymbol{s}(t)\right) &= \arcsin\left(\frac{\boldsymbol{e_T}\left(\boldsymbol{s}(t)\right) \cdot \boldsymbol{v_a}\left(\boldsymbol{s}(t)\right)}{\left|\boldsymbol{v_a}\left(\boldsymbol{s}(t)\right)\right|}\right) \end{aligned} \tag{3.38}$$

The kite area A_k is a constant parameter of the kite carousel, and the fluid density,ρ, is presumed to constant throughout the simulation. The aerodynamic drag coefficient, C_D is derived from the lift coefficient, C_L, which is computed using the angle of attack, α, which is controlled by the control variable $u_1(t)$, as shown;

$$\begin{aligned} C_L(\boldsymbol{u}(t)) &= 4.4\alpha(\boldsymbol{u}(t)) \\ C_D(\boldsymbol{u}(t)) &= C_{D0} + K C_L(\boldsymbol{u}(t))^2 \end{aligned} \tag{3.39}$$

The negatives in equation 3.38 are necessary due to the definition of the flow axes in equations 3.44 to 3.47. The zero lift drag coefficient, C_{D0}, and induced drag coefficient, K are constant aerodynamic parameters determined by the kite shape.

3.3.2.2 Definition of velocities

The computation of the apparent flow speed in the local coordinate system is the same process as in section 3.2.4, however here the time dependencies are shown, and the flow is assumed to be constant across the height profile. The apparent flow is computed,

$$\boldsymbol{v_a}\left(\boldsymbol{s}(t)\right) = \boldsymbol{v_{f_k}}\left(\boldsymbol{s}(t)\right) - \boldsymbol{v_k}\left(\boldsymbol{s}(t)\right) \tag{3.40}$$

with the kite velocity:

$$\boldsymbol{v_k}\left(\boldsymbol{s}(t)\right) = \begin{bmatrix} \dot{\theta}(t) l_T + \dot{\gamma}\cos(\theta(t))\sin(\phi(t)) r_c \\ \left(\dot{\phi(t)} + \dot{\gamma}\right) l_T \sin(\theta(t)) + \dot{\gamma}\cos(\phi(t)) r_c \\ \dot{\gamma} r_c \sin(\theta(t))\sin(\phi(t)) r_c \end{bmatrix} \tag{3.41}$$

and the incoming flow converted from the global to the local coordinate system;

$$\boldsymbol{v_{f_k}}\left(\boldsymbol{s}(t)\right) = \boldsymbol{T_L}'\left(\boldsymbol{s}(t)\right) \boldsymbol{T_G}'\left(\boldsymbol{s}(t)\right) \boldsymbol{v_{f_r}} \tag{3.42}$$

The conversion from global coordinate system (X, Y, Z) to tether base coordinates, through is done using transformation matrix $\boldsymbol{T_G}'\left(\boldsymbol{s}(t)\right)$; and from the tether base to the local coordinates at the kite (e_θ, e_ϕ, e_r), through $\boldsymbol{T_L}'\left(\boldsymbol{s}(t)\right)$ as follows:

$$\begin{aligned} \boldsymbol{T_G}\left(\boldsymbol{s}(t)\right) &= \begin{bmatrix} \cos(\gamma(t)) & -\sin(\gamma(t)) & 0 \\ \sin(\gamma(t)) & \cos(\gamma(t)) & 0 \\ 0 & 0 & 1 \end{bmatrix} \\ \boldsymbol{T_L}\left(\boldsymbol{s}(t)\right) &= \begin{bmatrix} \cos(\theta(t))\cos(\phi(t)) & -\sin(\phi(t)) & \sin(\theta(t))\cos(\phi(t)) \\ \cos(\theta(t))\sin(\phi(t)) & \cos(\phi(t)) & \sin(\theta(t))\sin(\phi(t)) \\ -\sin(\theta(t)) & 0 & \cos(\theta(t)) \end{bmatrix} \end{aligned} \tag{3.43}$$

3.3.2.3 Definition of axes

The axis definition is again identical to that shown in section 3.2.5, adjusted here to show its time dependencies. The tangential flow axis, $\boldsymbol{x_f}$, is used to determine the orientation of the drag force and is computed as follows:

$$\boldsymbol{x_f}\left(\boldsymbol{s}(t)\right) = \frac{-\boldsymbol{v_a}\left(\boldsymbol{s}(t)\right)}{|\boldsymbol{v_a}\left(\boldsymbol{s}(t)\right)|} \tag{3.44}$$

The lift is presumed to act perpendicular to the apparent flow, and kite orientation. To this end the kite pitching axis, $\boldsymbol{y_{k\perp e_T}}$ is computed as follows:

$$\begin{aligned} \boldsymbol{x_{k\perp e_T}}\left(\boldsymbol{s}(t)\right) &= \frac{\boldsymbol{x_f}\left(\boldsymbol{s}(t)\right) - \boldsymbol{e_T}\left(\boldsymbol{e_T}\cdot\boldsymbol{x_f}\left(\boldsymbol{s}(t)\right)\right)}{|\boldsymbol{x_f}\left(\boldsymbol{s}(t)\right) - \boldsymbol{e_T}\left(\boldsymbol{e_T}\cdot\boldsymbol{x_f}\left(\boldsymbol{s}(t)\right)\right)|} \\ \boldsymbol{y_{k\perp e_T}}\left(\boldsymbol{s}(t)\right) &= \boldsymbol{x_{k\perp e_T}}\left(\boldsymbol{s}(t)\right) \times \boldsymbol{e_T} \end{aligned} \tag{3.45}$$

Where $\boldsymbol{y_{k\perp e_T}}$ is rotated around the kite roll axis,$\boldsymbol{x_{k\perp e_T}}$, by the turning angle ψ using the Rodrigues rotation formula, resulting in,

$$\begin{aligned} \boldsymbol{y_k}\left(\boldsymbol{u}(t),\boldsymbol{s}(t)\right) = \; & \boldsymbol{y_{k\perp e_T}}\cos(\psi(t)) \\ & + \left(\boldsymbol{x_{k\perp e_T}}\left(\boldsymbol{s}(t)\right) \times \boldsymbol{y_{k\perp e_T}}\left(\boldsymbol{s}(t)\right)\right)\sin(\psi(t)) \\ & + \boldsymbol{x_{k\perp e_T}}\left(\boldsymbol{s}(t)\right)\left(\boldsymbol{x_{k\perp e_T}}\left(\boldsymbol{s}(t)\right)\cdot\boldsymbol{y_{k\perp e_T}}\left(\boldsymbol{s}(t)\right)\right)\left(1-\cos(\psi(t))\right) \end{aligned} \tag{3.46}$$

Finally the z-axis for the flow coordinate system is computed with,

$$\boldsymbol{z_w}\left(\boldsymbol{u}(t),\boldsymbol{s}(t)\right) = \boldsymbol{x_w}\left(\boldsymbol{s}(t)\right) \times \boldsymbol{y_k}\left(\boldsymbol{u}(t),\boldsymbol{s}(t)\right) \tag{3.47}$$

Chapter 4

Results

4.1 Dimensional Analysis

A dimensional analysis was performed in order to illustrate the effect of varying device dimensions on output. It is important to remember that by using numerical methods it is possible that the solution found is a local minima, as the optimization problem depends heavily on the initial conditions used. Through this analysis, steps are taken to compute a realistically feasibly flightpath with a net power output. This is done in a number of steps. First, a start-up sequence is simulated to determine realistic starting conditions for the periodic flightpath. Here, the assumptions made regarding the carousel start-up procedure and how it would initiate a cycle are explained.
The starting conditions are used to compute an optimized flightpath. A dimensional analysis is performed to show the relationship between device dimensions and operation and ultimate power output.
Finally the results of this investigation are discussed through a case study of the potential of the kite carousel placed in a tidal stream.

In order to maintain consistency the input bounds, path and terminal constraints are kept constant throughout all runs.

Table 4.1: Initial conditions for start up sequence

Symbol	unit	Ground start	Suspended start
θ	rad	$\pi/2$	$\pi/36$
ϕ	rad	0	0
γ	rad	-$\pi/2$	-$\pi/2$
$\dot{\theta}$	rad/s	0	0
$\dot{\phi}$	rad/s	0	0
$\dot{\gamma}$	rad/s	$\pi/6$	0

4.1.1 Start-up sequence

When optimizing a flightpath the solutions depend heavily on the initial conditions used, which means it is important that these conditions are realistic. The flightpath assumes a starting condition of a flying, moving kite to initiate a periodic flightpath coinciding with the carousel rotation. To this end a start-up sequence is modelled to simulate the kite behaviour as movement is initiated. Here two start-up strategies are illustrated, representing common kite starting positions. First, a launch from ground level is shown, which would be a common procedure for airborne kites. Second, a start-up is illustrated from a kite at near zenith position. This strategy would apply to a submerged kite with regulated buoyancy such that at low flows the kite remains suspended at a low θ.
The initial conditions for each of the scenarios are displayed in table 4.1. Note that θ for the suspended start is taken as non-zero to allow for drift due to flow. All kite angular velocities are presumed to be negligible except for the carousel rotation itself in the ground start scenario. Here it is assumed a mechanical start-up is used for the initial upstream section to get the kite into position. For the suspended start it is presumed the carousel is kept stationary until the kite reaches its desired attitude and position, at which point carousel rotation is initiated. Here γ is defined as $-\pi/2$ for the carousel arm directed directly downwind. The parameters presented here were chosen as initial approximations of dimensioning of a possible real system. The environmental parameters such as flow and fluid density were similarly chosen to represent a realistic representation for both an air- and a water-based model. The environmental and device dimensional parameters are summarized in table 4.2. It is noted that the same kite area is used for either setup, however the flow characteristics vary, as do the tether lengths

Table 4.2: Initial conditions for start up sequence

Symbol	unit	Ground start	Suspended start
ρ	kg/m^3	1.225	1025
v_f	m/s	8	2.0
r_c	m	3	3
l_T	m	50	60
m_k	m/s	5	700
A_k	m^2	10	10
Æ	-	4.5	4.5

Table 4.3: Initial conditions for start carousel cycle following from ground start sequence

Symbol	unit	value
θ	rad	$\pi/18$
ϕ	rad	-$\pi/4$
γ	rad	0
$\dot{\theta}$	rad/s	-0.38
$\dot{\phi}$	rad/s	-1.15
$\dot{\gamma}$	rad/s	$\pi/6$

and kite mass. For the airborne ground start the tether length is set to 50 m, while for the suspended start in submerged conditions l_T increased to 60 m in anticipation of further case studies involving a longer tether. Due to the substantially higher forces exerted on the kite in a denser fluid it is assumed that the kite must be a rigid structure in order to sustain them. This results in a higher mass, compounded by the fact that the added mass due to the size of the wing is significantly higher than the airborne version.

4.1.1.1 Airborne start

Figure 4.1a, shows the path followed by an airborne kite to a point where the full cycle is initiated as shown in figure 4.1b . The starting conditions for this cycle, resulting from the start up are summarized in table 4.3

As stated the kite is presumed to start fully downwind from the generator as it starts to rotate. For a submerged type start, the kite starts in similarly stable conditions, but at low value of θ. Here the theta is taken as non-zero to allow for drift due to flow.

This example of a start-up sequence and resulting flightpath can be iterated further to adjust the starting conditions of the full flightpath and resulting power. Figure 4.2

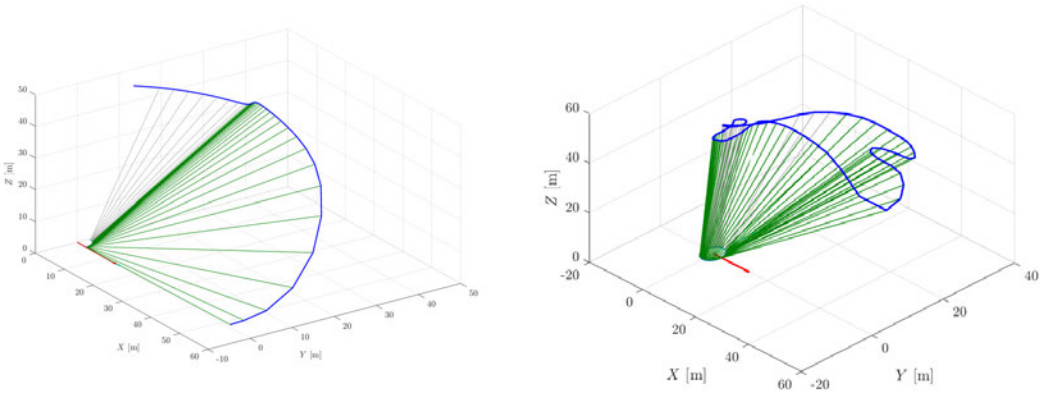

(a) Start-up

(b) Full cycle

Figure 4.1: Ground start sequence for an airborne kite results

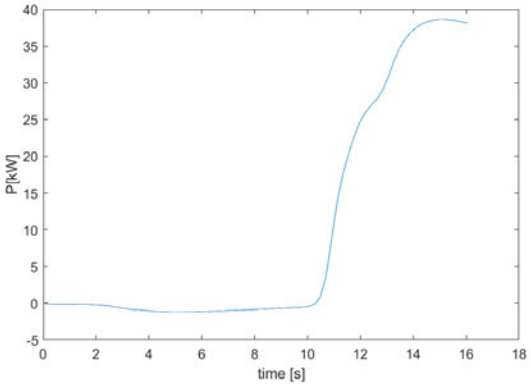

Figure 4.2: Power output over full cycle after ground start

shows the overall power output of this flightpath to be equal to 38 kW after a full 16 s cycle, equal to 0.17 kWh. The majority of the power resulting from the dive during the down wind phase of the cycle where the kite increases velocity and subsequently the additional loop used to maintain the tether tension during the crosswind phase.

4.1.1.2 Submerged start

For the suspended start a slightly more involved flightpath is used. In this case the carousel is kept stationary until the kite reaches the point of initiation of the periodic flightpath. This subsequently presumes an immediate acceleration to the set $\dot{\gamma}$. As with the ground start, the scenario presented here represents one possible iteration, through additional manoeuvring the kite can be directed to a variety of cycle initiation points. Figure 4.3 shows the start-up flightpath and the resulting generation cycle initialized

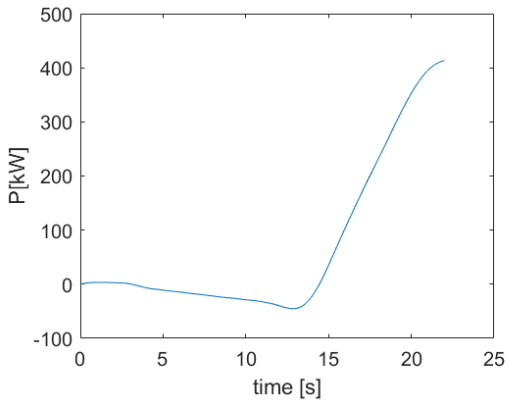

Figure 4.4: Power output over full cycle, following a suspended start

by the this sequence. It is noted here that despite the tether being longer than in the ground start scenario the overall flight path is substantially shorter. This is due to the higher kite mass and lower fluid velocity resulting in a lower kite velocity.

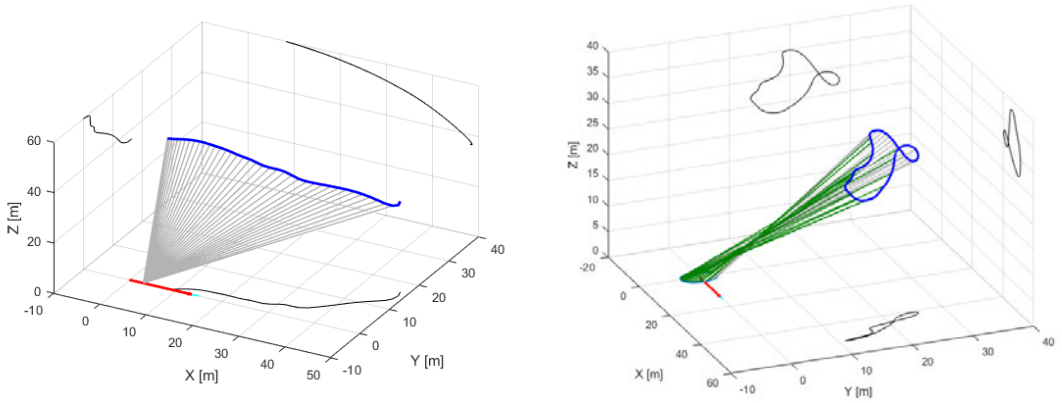

(a) Start-up

(b) Full cycle

Figure 4.3: suspended start sequence for a submerged kite results

The power produced by the full cycle shown in figure 4.3b is shown in Figure 4.4, which shows a total predicted power of 400 kW for this configuration over a 22 s cycle, equal to 2.44 kWh. Similar to the airborne cycle the power is generated as the base of the kite tether moves down and across the flow. Also, it is noted that during the entire cycle the kite remains down stream of the carousel. The starting conditions and consequently final startup conditions are shown in table 4.4.

Table 4.4: Initial conditions for start carousel cycle following from suspended start sequence

Symbol	unit	value
θ	rad	0.93
ϕ	rad	$\pi/9$
γ	rad	0
$\dot{\theta}$	rad/s	-0.02
$\dot{\phi}$	rad/s	0.03
$\dot{\gamma}$	rad/s	0.29

4.1.2 Parameter study

To analyse the carousel configuration two dimensionless parameters were chosen to judge their impact on performance. These parameters were r_c/l_T, and $|v_b|/|v_f|$; where r_c/l_T looks at sizing the carousel carousel and tether dimensions, and $|v_b|/|v_f|$ looks at operating points of carousel rotation to flow velocity. While investigating the effect of varying these parameters on carousel output all previous assumptions regarding control limits, kite dimensions, and lift and drag coefficients were kept constant. The optimization problem is as shown in section 3.3.2 with the coefficient limits set as in table 4.5. The results of this study are shown through a dimensionless parameter representing system power over a cycle.

The two methods of start-up introduced in the previous section provide examples of

Table 4.5: Optimization system limits

limit	minimum	maximum	unit
θ	0	1.23	rad
α	0.02	0.4	rad
ψ	-0.1	0.1	rad
$\dot{\alpha}$	-0.1	0.1	rad/s
$\dot{\psi}$	-0.2	0.2	rad/s

ways in which a kite can be manoeuvred into the starting position desired for a periodic flight path. Realistically each carousel configuration will have its own optimum initial conditions, and a specific launch procedure in which these starting conditions can be met. However, for the purpose of this study, the starting kite position is kept constant throughout all carousel configurations. The initial conditions used for the flightpath optimizations are shown in table 4.6. It is noted that while $\dot{\theta}$, and $\dot{\phi}$ are not explicitly

Table 4.6: Initial conditions for start carousel cycle following from suspended start sequence

Symbol	value	unit
$\theta(t_0)$	0.93	rad
$\phi(t_0)$	$\pi/9$	rad
$\gamma(t_0)$	0	rad
$\alpha(t_0)$	0.11	rad
$\psi(t_0)$	-0.01	rad

initialized, they are constrained to be periodic, and to limit the kite velocity at the start to ≤ 10 m/s. This provides some flexibility for the optimization software, but provides a realistic limit on initial conditions. It is noted that while this limit on kite velocity is in place, it was not reached in the optimizations run. The full numerical results of the parameter study are shown in appendix B.

4.1.2.1 Power trend and coefficient

In order to consistently represent the power output of each configuration, the power is made dimensionless with respect to the kinetic energy flux through a reference surface. The total kinetic energy flux is computed by:

$$P_f = \frac{1}{2}\rho v_f^3 A \tag{4.1}$$

where A is the swept area, and ρ and v_f are the average flow density and velocity. The definition of the swept area is crucial to the resulting dimensionless power by accounting for parameter change during the study performed. The swept area of a kite carousel can be accounted for in numerous ways. This analysis looks at three definitions of the swept area. First is the geometrically determined swept area, A_{geo} which is determined by defining a vertical polygon defined by the carousel dimensions as shown in figure 4.5 and:

$$A_{geo} = 2r_c l_T + 2l_T^2 \sin(\pi/8)\cos(\pi/8). \tag{4.2}$$

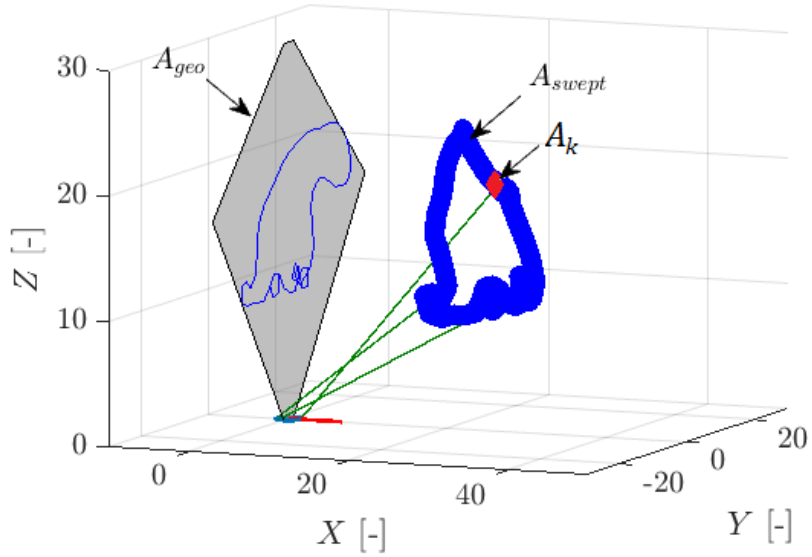

Figure 4.5: Illustration of different representative areas used to define swept area by kite

The area described by this polygon gives an estimate of the section of flow from which energy is extracted by the kite. Keeping the computation of this area consistent over the various flightpath optimizations gives an basis upon which to evaluate the outcomes. It must be mentioned that this computation of swept area is determined largely by the length of the tether. Hence a change in tether length would disproportionately influence the dimensionless power when comparing configurations of the same r_c/l_T ratio. While this method incorporates some of the device characteristics this geometric swept area is entirely independent of the actual kite area and thus further adjustment is required to account for changes in kite size.

To this end, the second method for determining the swept area that is investigated takes an approach more similar to that used when determining turbine swept area, A_{swept}. Here the area is determined by the cross section through which the working surface moves, ie the disc defined by the turbine diameter. Since the working surface of the carousel is the kite, the swept area could be interpreted as the area traversed by the kite over a cycle and is also illustrated in figure 4.5. This area is determined by the width of the kite trajectory multiplied by the length of the kite. This method is highly dependant on kite trajectory, which in part is a function of the carousel dimensions, but mainly depends on how the kite is controlled. It must be noted here that this method does not account for changes in kite aspect ratio

Finally, a third method of determining the area used to compute the potential power available is by using just the area of the kite A_k. As the kite itself is the source of generation of lift force from the flow, the size of the kite is likely to have a more scaleable impact than the lengths of r_c and l_T.

Figure 4.6 shows the power curve outcome for a carousel where $r_c = 0.05 l_T$ as a function of A_{geo} as this remains constant while A_{swept} varies for each resulting flightpath. This shows a peak extraction at $|v_b|/|v_f| = 0.29$, which is close to the 0.33 optimum derived by Loyd [20]. At higher rotational velocities, the power extracted reduces due to the fact that kite acceleration is limited by the kite mass, which has been increased from air-based examples to account for the higher forces occurring in the submerged state and to account for the added mass effect due to the higher fluid density. By maintaining constant carousel dimensions and flow velocity throughout runs, the period of the carousel is reduced to increase $|v_b|/|v_f|$. This allows less time for the kite to accelerate to increase power for the downstream section, and decelerate in time to reduce power for when it is being pulled upstream. This is further influenced by the limits assigned to $\dot{\alpha}$ which limits the change in lift to drag ratio, which influences the overall kite force and consequently acceleration and tether tension.

At very low $|v_b|/|v_f|$ ratios the power tends toward zero due to it being directly related to v_b. While the longer periods here allow for the kite velocity to develop over a longer period of time, this is mitigated by the increase in time that the kite is being pulled up wind. At a certain point the increase in generated power no longer increases the average power over a cycle.

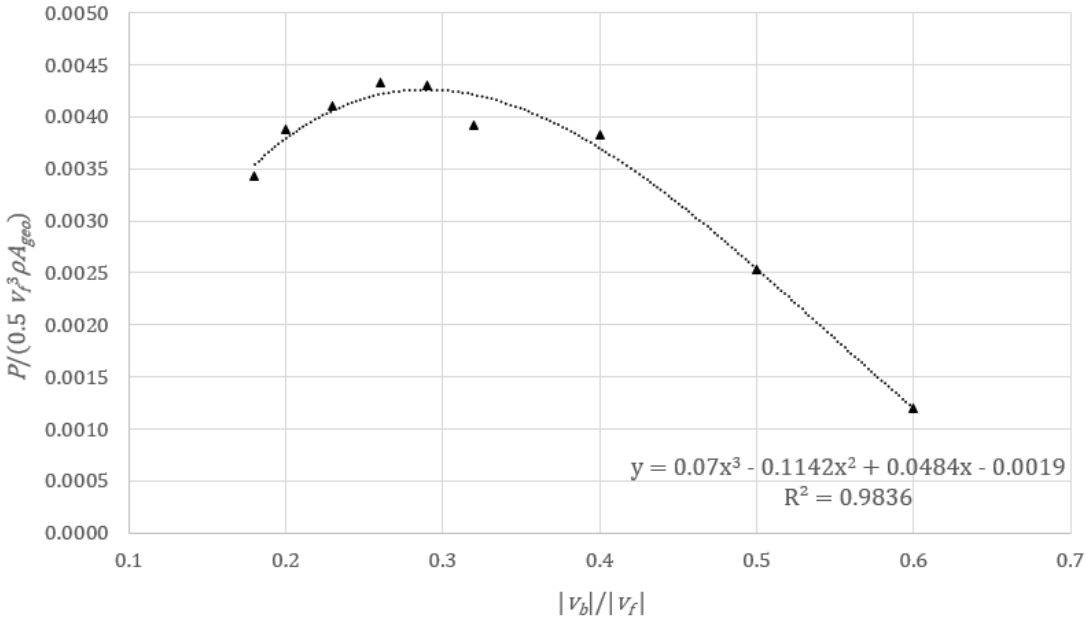

Figure 4.6: Results for $r_c/l_T = 0.05$

As mentioned, another way to define the dimensionless power output is by using a swept area defined by the length of the flightpath multiplied by the width of the kite. As such, the results of this method depend more on the flightpath used and less on the dimensions of the carousel. Figure 4.7, shows the power output results as a function of this swept area.

A distinct difference in location of peak power is seen here. While previously this was shown to be at $|v_b|/|v_f| = 0.29$, in this case it has shifted to 0.43. Although this may be a more accurate method of comparing kite efficiency by comparing power output to the power available in the area the working surface of the kite passes through; with regards to sizing a carousel it is less useful.

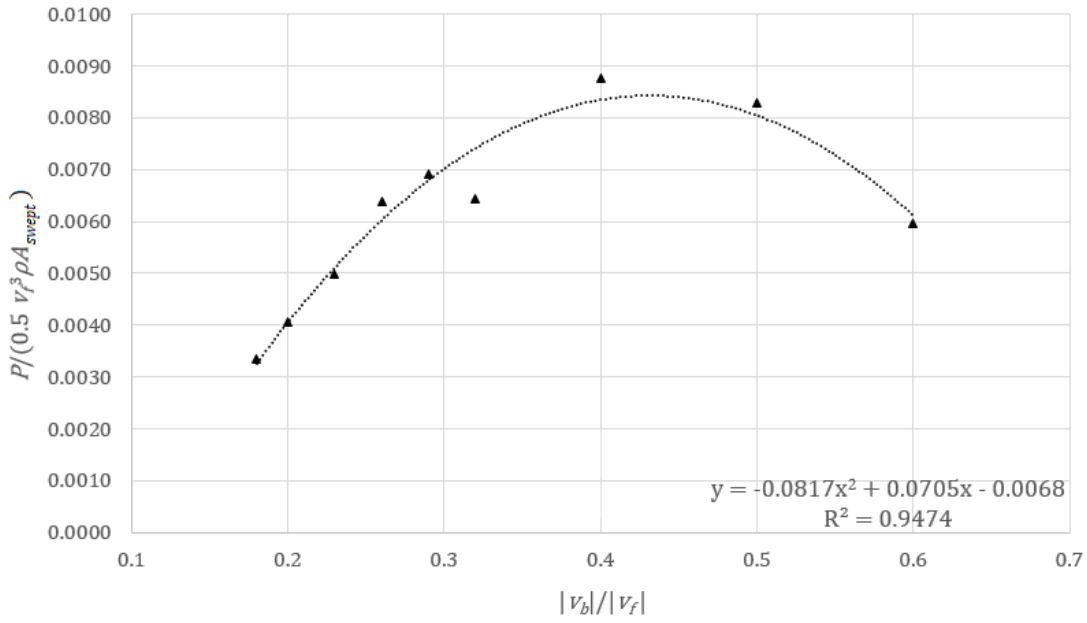

Figure 4.7: Results for $r_c/l_T = 0.05$, using alternative swept area definition

4.1.2.2 Flightpath outcomes

Figure 4.8 shows flight paths for six $|v_b|/|v_f|$ ratios, describing the development of the optimum flightpath through various operating set points. The carousel base is depicted as a circle at the base of the tether, with a red arrow indicating the direction of the flow. The thick line indicates the flightpath flown with a number of tether lines drawn in to show how the flightpath develps over a full carousel cycle. Portions of positive power generation are indicated with green tether lines whereas when depicted in grey this indicates a portion of the cycle where the kite is being dragged.

These figures show how as the carousel tip speed ratio increases the optimal flightpath reduces in length from a complex pattern for $|v_b|/|v_f| = 0.18$ to a small smooth figure 8 at $|v_b|/|v_f| = 0.6$. The change in tip speed ratio is modelled by adjusting the angular velocity of the carousel, effectively simulating control of the power take off. Subsequently higher tip speed ratios correlate with shorter carousel periods, which in turn allows less time for kite to fly complex patterns before returning to its starting point at the end of a rotation. Throughout these cases a couple of flightpath characteristics are identified. When possible during the down, and cross stream portion of the cycle the kite increases its velocity through a dive manoeuvre and maintains this through additional control

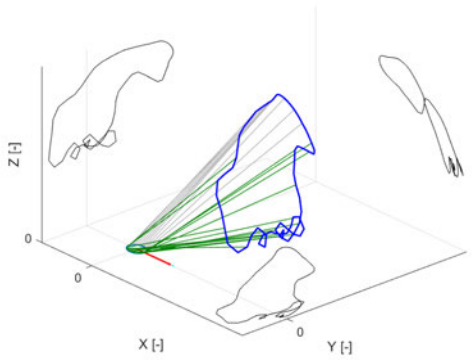

(a) $|v_b|/|v_f| = 0.18$

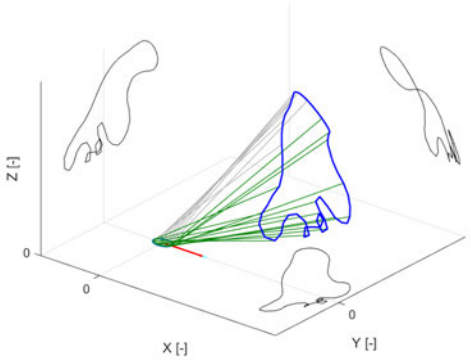

(b) $|v_b|/|v_f| = 0.20$

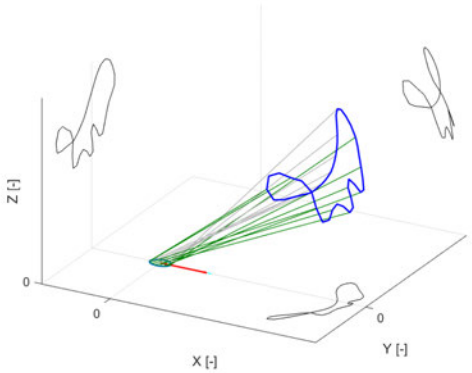

(c) $|v_b|/|v_f| = 0.29$

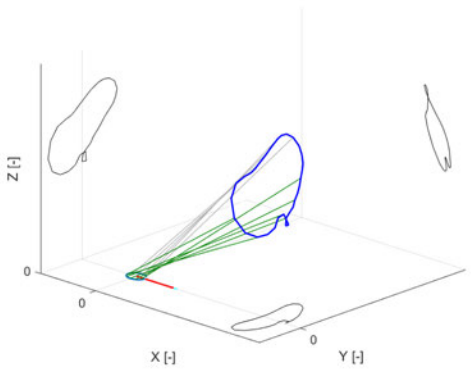

(d) $|v_b|/|v_f| = 0.40$

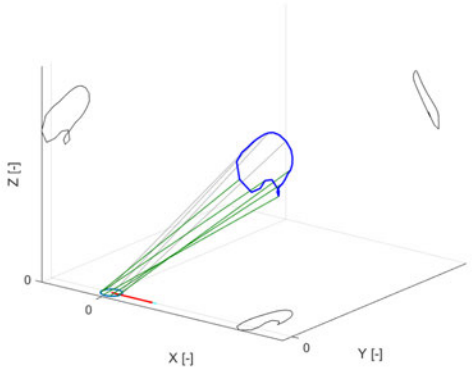

(e) $|v_b|/|v_f| = 0.50$

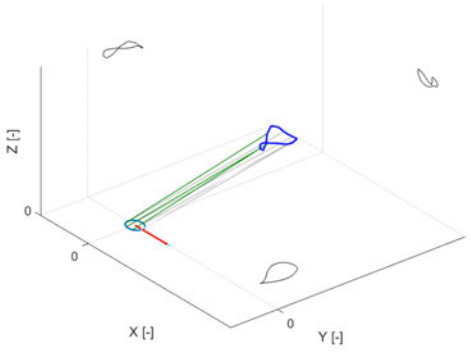

(f) $|v_b|/|v_f| = 0.60$

Figure 4.8: Flightpath evolution with $|v_b|/|v_f|$, for $r_c/l_T = 0.05$

inputs where possible, resulting in figure 8 patterns throughout the crosswind portion of the cycle in figures 4.8a and 4.8b. At a tip speed ratio of 0.29 in figure 4.8b, these figure 8 patterns disappear and the kite merely oscillates back and forth as it pulls the carousel around. This distinct difference in flightpath shape is seen in the dip in power in figure 4.6. Despite the lower overall power, figure 4.7 shows a jump in power coefficient due to the dependency here on flightpath length. Figure 4.9 shows the relative kite velocity throughout a carousel period. It is noted that while the generating portion of the cycle starts at roughly π rad, the kite pre-empts this by increasing velocity while moving cross stream and subsequently diving as the carousel rotates downstream. In the lower tip speed ratio configurations, this velocity is maintained through manoeuvres. However in figures 4.9a and 4.9b, with the shorter rotation periods, the loss of kite velocity is visible where the kite loops up, and gains velocity again as it decends further into the power zone. The instantaneous power produced over a cycle for each of the cases are shown in figure 4.10. This shows a similar trend of lower levels of power required during the first half of the cycle where the kite is dragged upstream by the carousel; followed by a spike in generation as the kite starts its dive and cross stream manoeuvres. This change in power is due to a combination of the increased kite velocity during the dive manoeuvre and the adjusted α. The slope of the spike determined by the control limit $\dot{\alpha}$. It is further noted that for the lower values of $|v_b|/|v_f|$, the power consumed by the carousel on the upstream portions of the cycle are proportionally smaller than for high values of $|v_b|/|v_f|$. Which confirms that a relatively slower moving carousel requires less power to pull the kite upstream. Due to the limits placed on $\dot{\alpha}$ and the shorter rotational period of the carousel at higher values of $|v_b|/|v_f|$ it is clear, particularly in figure 4.8f that the maximum α of 0.4 is not reached to due the need to reduce power in time for the upstream portion of the cycle.

The trends in figure 4.11 further show a similar strategy for the control of α, which minimizes the lift and drag coefficients during the first half of the cycle and maximizes during power generation. These trends similarly show how the turning control of ψ smoothes out for $|v_b|/|v_f| = 0.6$ whereas at $|v_b|/|v_f| = 0.18$ the control is far more erratic.

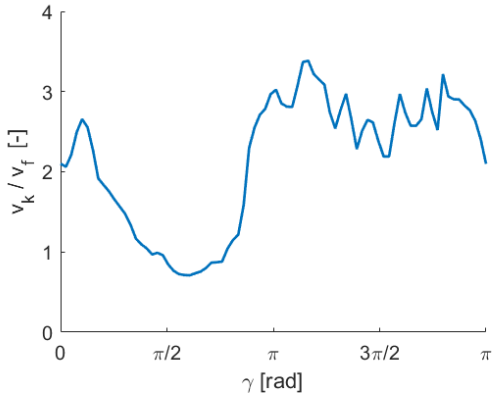

(a) $|v_b|/|v_f| = 0.18$

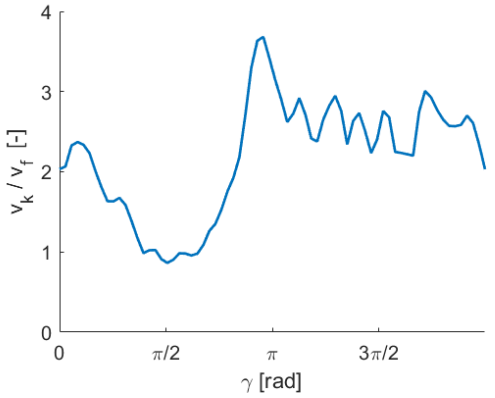

(b) $|v_b|/|v_f| = 0.20$

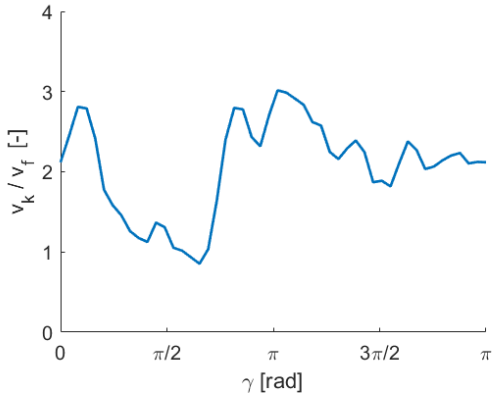

(c) $|v_b|/|v_f| = 0.29$

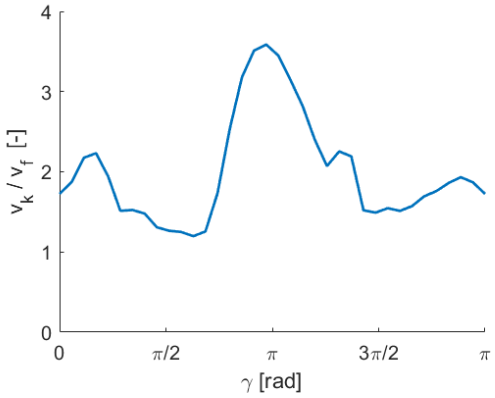

(d) $|v_b|/|v_f| = 0.40$

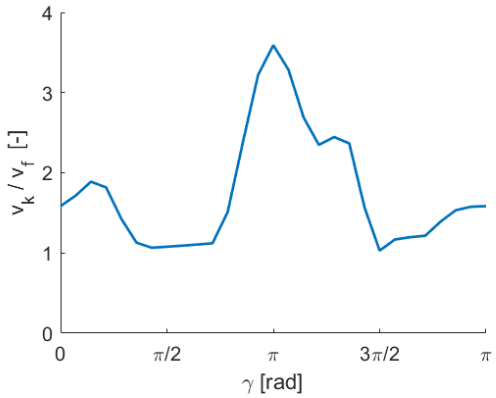

(e) $|v_b|/|v_f| = 0.50$

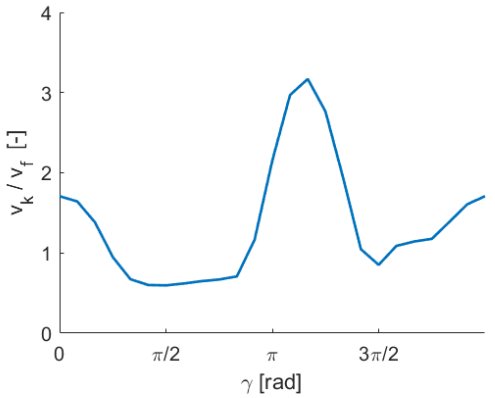

(f) $|v_b|/|v_f| = 0.60$

Figure 4.9: Kite velocity evolution with $|v_b|/|v_f|$, for $r_c/l_T = 0.05$

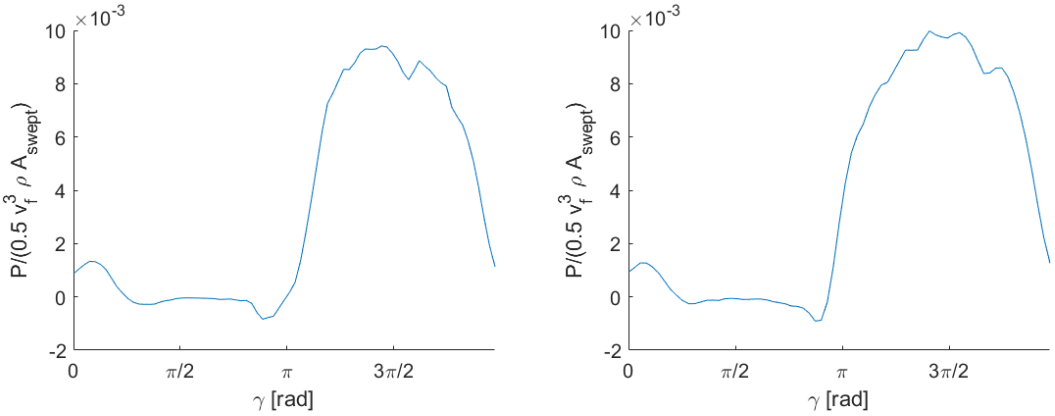

(a) $|v_b|/|v_f| = 0.18$

(b) $|v_b|/|v_f| = 0.20$

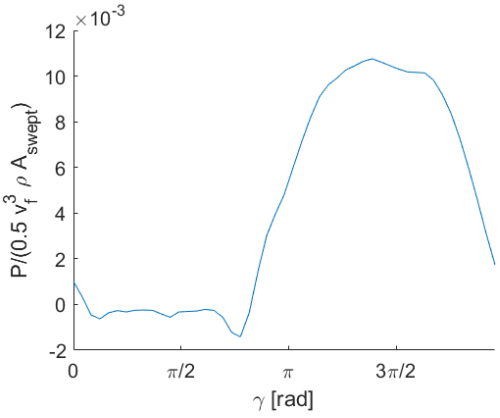

(c) $|v_b|/|v_f| = 0.29$

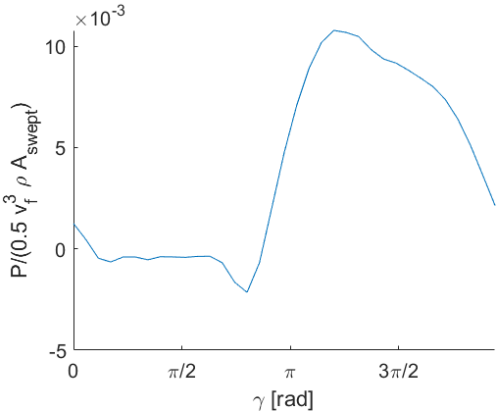

(d) $|v_b|/|v_f| = 0.40$

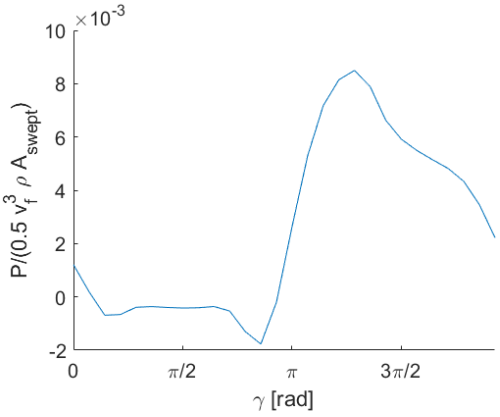

(e) $|v_b|/|v_f| = 0.50$

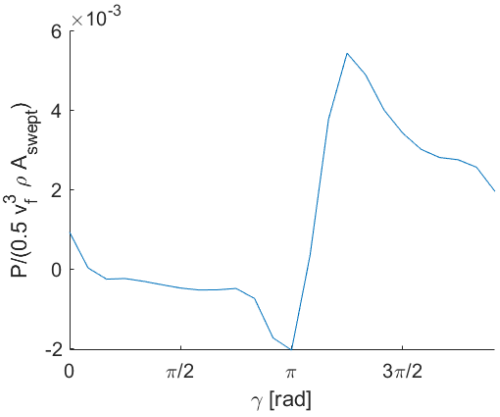

(f) $|v_b|/|v_f| = 0.60$

Figure 4.10: Carousel power throughout cycle for , for $r_c/l_T = 0.05$

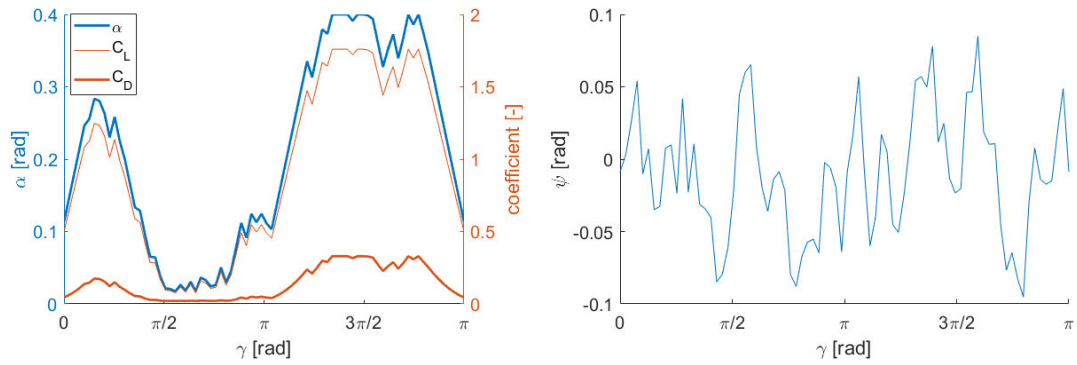

(a) $|v_b|/|v_f| = 0.18$

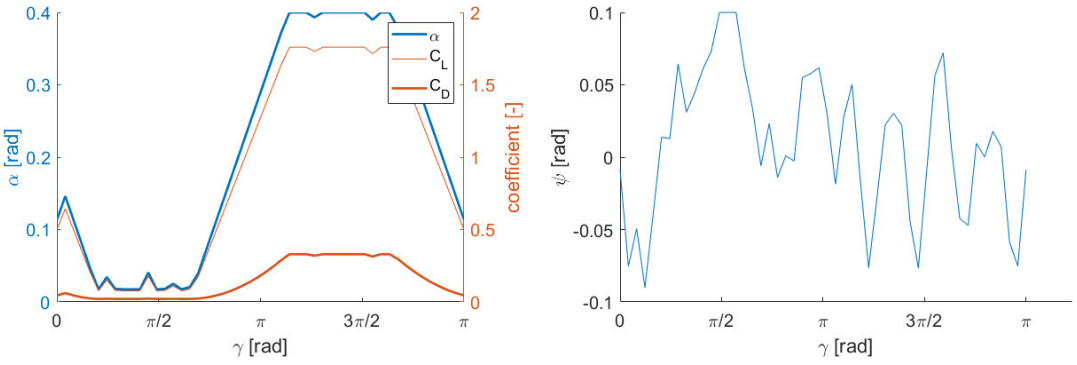

(b) $|v_b|/|v_f| = 0.29$

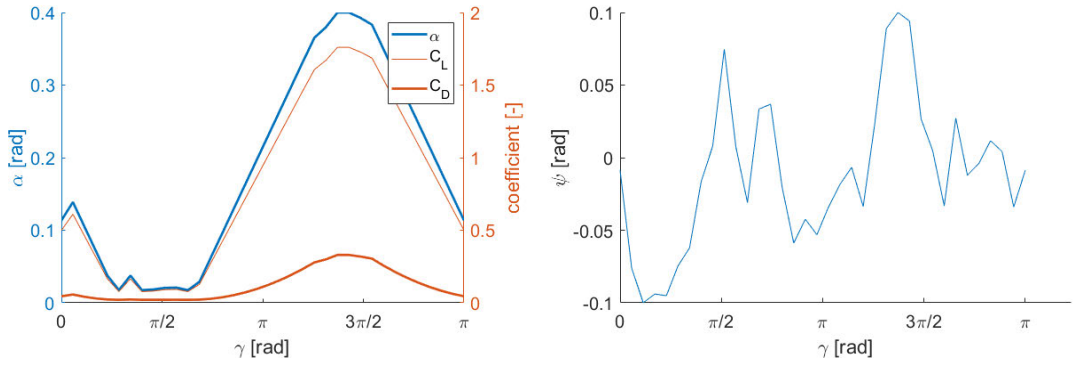

(c) $|v_b|/|v_f| = 0.4$

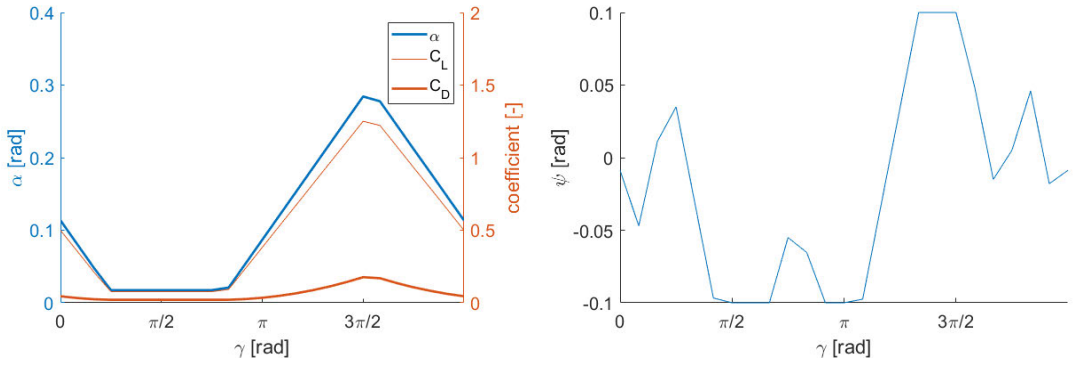

(d) $|v_b|/|v_f| = 0.6$

Figure 4.11: Carousel controls for optimum flightpath throughout cycle for, for $r_c/l_T = 0.05$

4.1.2.3 Initial position dependency

As stated, the overall outcome of the flightpath optimization is dependant on the starting conditions assumed at the initialisation of the optimization software. Here, a brief examination of the effect of varying this starting point is given for the flightpaths shown in figures 4.8a and 4.8f, to show opposite ends of the spectrum investigated here. This is done by varying the kite starting position defined by applying a 10% adjustment to θ_0 and ϕ_0 as shown in table 4.7, which also shows the change in the resulting average power coefficient resulting from the simulations, compared to the initial case in figure 4.8a. The power coefficient $C_{P_{geo}} = P/0.5v_f^3 A_{geo}$ is taken with the swept area A defined as A_{geo} in figure 4.5. While a 10% adjustement to position is substantial, this range checks the effect of small deviations on how the optimization problem is interpreted and solved. The aim of this exercise is not to find a global optimum which would involve investigating far larger boundaries regarding starting conditions.

Table 4.7: Factors applied to initial kite position and effect on power coefficient

			$\lvert v_b\rvert/\lvert v_f\rvert = 0.18$		$\lvert v_b\rvert/\lvert v_f\rvert = 0.60$	
Case	θ/θ_0	ϕ/ϕ_0	$\Delta C_{P_{geo}}[\%]$	$\Delta C_{P_{geo}}$ $[10^{-3}]$	$\Delta C_{P_{geo}}$ [%]	$\Delta C_{P_{geo}}$ $[10^{-3}]$
1	1.1	1.1	1.90%	0.0708	-2.33%	-0.0263
2	0.9	1.1	0.11%	0.0041	26.80%	-0.3017
3	1.1	0.9	0.55%	0.0204	-10.52%	-0.1184
4	0.9	0.9	-6.97%	-0.2595	-12.78%	-0.1439

The resulting flightpaths with the instantateous power and kite velocity throughout the cycles are shown in figure 4.12. While these figures clearly show adjusted flightpaths for each individual starting point the overall power coefficient in table 4.7, and both the power and kite velocity trends remain similar. The carousel behaviour shown in figure 4.12 shows similar characteristics for the various starting points. Although the flightpaths for the two tip speed ratio's in 4.12a and 4.12d appear substantially different, the power and kite velocity curves show similar attributes. As the carousel starts it upstream movement, the kite moves horizontally to allow for a positive power contribution due to the crossflow motion. The kite then ascends and moves across, fol-

lowing the tether base attached to the carousel as the it moves further upstream while minimizing kite velocity as it moves along with the carousel. The dive is initiated once the base of the tether starts its downstream motion, this coincides with a rapid increase in kite velocity and power coefficient. It is noted that, where possible, the dive portions of the flightpath are oriented in the same direction as the carousel rotation. As such, in figure 4.12, the flightpaths tend to have the kite abort the dive by turning to the right, allowing the kite to gain altitude before initiating cross flow flight.
For the lower tip speed ratio carousel, the velocity is maintained through a series of complex loops and figure 8 type manoeuvres. The higher tip speed ratio sacrifices his extended period of generation in order to move the kite back into starting position.

An additional matter that was investigated is the effect of different starting kite orientations, defined by α_0 and ψ_0. Due to the limits imposed on the control inputs $\dot{\alpha}$ and $\dot{\psi}$ there is a limit to how quickly α and ψ can be adjusted. Table 4.8 shows the 4 cases modelled for the varying initial kite orientation, with the corresponding power coefficients for each case. Although 10% margins applied to α_0 and ψ_0 are the same as those applied to θ_0 and ϕ_0, due to the smaller value for the original results this results in a smaller change in the real angles applied. Additionally, with $\dot{\alpha}$ and $\dot{\psi}$ being directly controlled through the control variable, there resulting similarity in results is as expected.

Table 4.8: Factor applied to initial kite orientation and effect on power coefficient

			$\lvert v_b\rvert/\lvert v_f\rvert = 0.18$		$\lvert v_b\rvert/\lvert v_f\rvert = 0.60$	
Case	α/α_0	ψ/ψ_0	$\Delta C_{P_{geo}}$[%]	$\Delta C_{P_{geo}}$ [10^{-3}]	$\Delta C_{P_{geo}}$ [%]	$\Delta C_{P_{geo}}$ [10^{-3}]
1	1.1	1.1	2.80%	0.1041	4.39%	0.0494
2	0.9	1.1	0.75%	0.0277	-3.64%	0.0411
3	1.1	0.9	1.60%	0.0595	-2.54%	0.0286
4	0.9	0.9	1.05%	0.0392	-2.48%	0.0279

Figure 4.13 shows the results of the adjustments to initial kite orientation. It is noted here that the graphs for the 5 cases are substantially more in line with each other here than when the initial starting point was changed. this is attributed to the fact that

the limits set for control adjustment are high enough that the effect of the adjusted kite orientation is mitigated substantially.

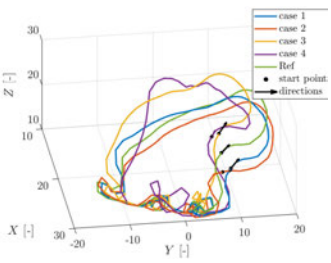

(a) Flightpath
$|v_b|/|v_f| = 0.18$

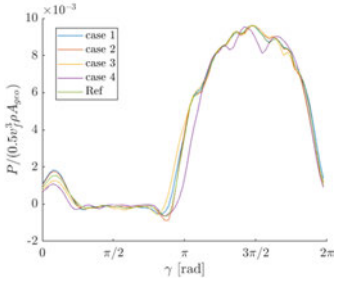

(b) power coefficient
$|v_b|/|v_f| = 0.18$

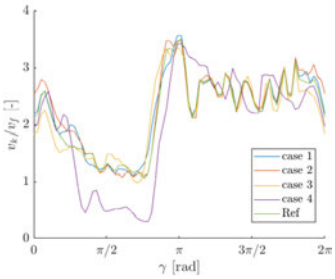

(c) Kite velocity
$|v_b|/|v_f| = 0.18$

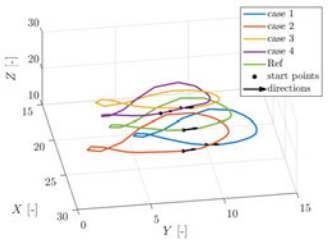

(d) Flightpath
$|v_b|/|v_f| = 0.60$

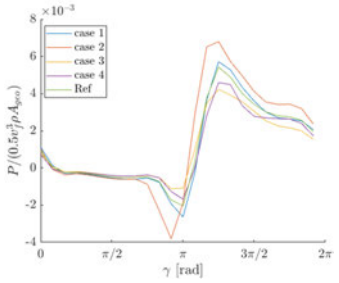

(e) power coefficient
$|v_b|/|v_f| = 0.60$

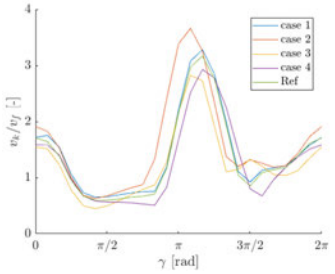

(f) kite velocity
$|v_b|/|v_f| = 0.60$

Figure 4.12: Results for alternative initial kite position

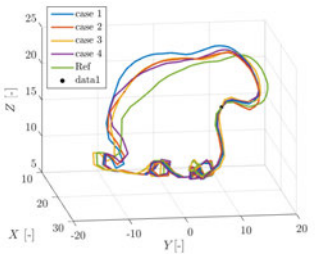

(a) Flightpath
$|v_b|/|v_f| = 0.18$

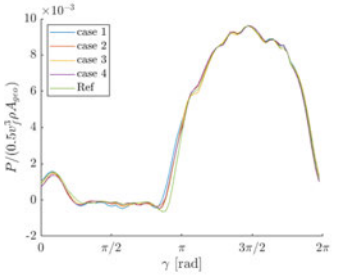

(b) power coefficient
$|v_b|/|v_f| = 0.18$

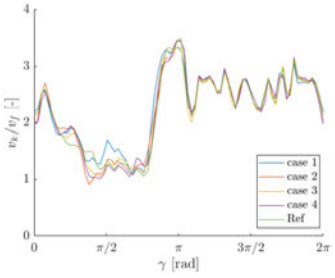

(c) Kite velocity
$|v_b|/|v_f| = 0.18$

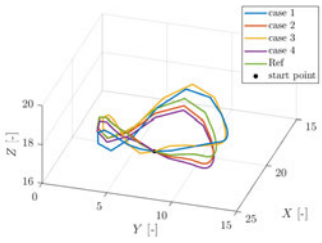

(d) Flightpath
$|v_b|/|v_f| = 0.60$

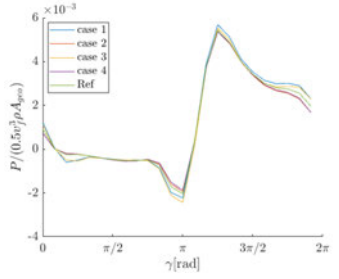

(e) power coefficient
$|v_b|/|v_f| = 0.60$

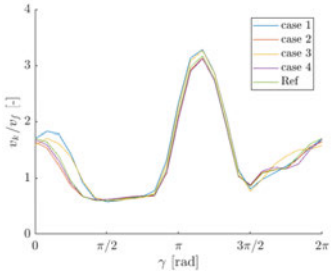

(f) kite velocity
$|v_b|/|v_f| = 0.60$

Figure 4.13: Results for alternative initial kite orientation

4.1.3 Validation with literature

The potential of the kite carousel has been investigated twice before in literature [1, 2]. Due to the dimensional analysis performed in the previous section it is possible to compare the results from these papers with the outcomes of the parameter study. Table 4.9 shows the dimensionless parameters resulting from the data provided in these papers. Whereas most parameters were explicitly stated, s_k was estimated in both cases, as was the carousel period T, from which v_f is derived, from the Williams paper. Here the dimensionless power is defined using two different swept areas. First, for $C_{P_{geo}}$, the swept area is as used in the previous section; defined by the device parameters as per figure 4.5. For $C_{P_{swept}}$ the swept area is defined using the area of the flightpath itself, computed as the product of the kite flightpath s_k and the kite width d_k.

Table 4.9: Dimensionless parameters resulting from literature data

Variable	Lit 1	Lit 2
$C_{P_{geo}}$	1.3×10^{-5}	3.5×10^{-3}
$C_{P_{swept}}$	1.7×10^{-3}	6.8×10^{-3}
C_{P_k}	0.39	7.75
$\lvert v_b \rvert / \lvert v_f \rvert$	0.25	0.33
r_c/l_T	0.01	0.33

While the power coefficients for the two lit cases are within a similar range for $C_{P_{swept}}$, for the geometric and kite area based power coefficients there is a substantial range between values. Although there are differences in optimization strategies and kite model characteristics; the difference in power coefficients based on these alternative areas is primarily attributed to the substantial difference in scale. These results suggest that there are limits to using $C_{P_{geo}}$ and C_{P_k} without further corrections to adjust for device scaling. Whereas when looking at the traversed flightpath area through $C_{P_{swept}}$, the two results appear to be less dependant on device dimensions. The scale of the devices modelled in literature is shown in figure 4.14, where the devices are shown with rough estimations of the area used to describe the flightpath. The model dimensions

used in the dimensional analysis are similarly included to show the difference in scale. These estimates are based on the graphical results presented in 'Lit 1' [1] and 'Lit 2' [33]. The corresponding dimensions are summarized in table 4.9.

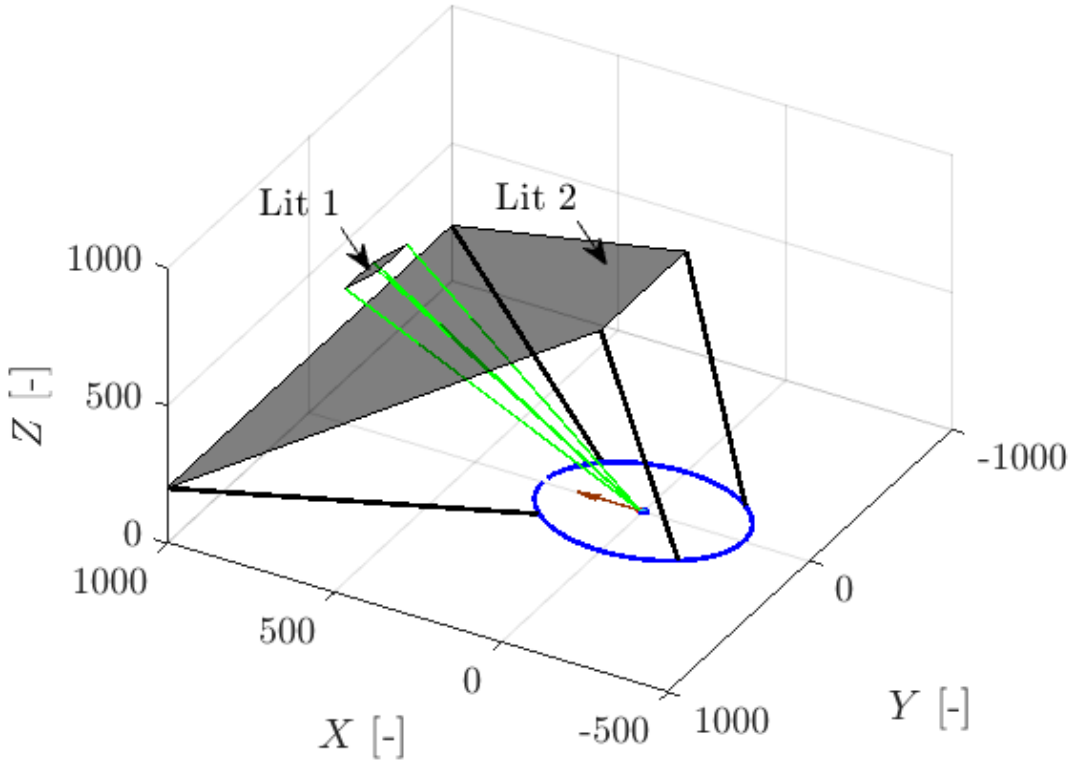

Figure 4.14: Representation of scale of literature dimensions, and definition of s_k

Table 4.10: Carousel dimensions from literature

Variable	unit	Lit 1	Lit 2
ρ	kg/m^3	1.225	1.225
v_f	m/s	15	9
A_k	m^2	25	500
m_k	kg	50	300
l_T	m	1000	900
r_c	m	10	300
T	s	17	630
s_k	m	530	3500

In Lit 1 the proposed flightpath ranges from a figure 8 type shape to an oval. As such s_k is deduced as the perimeter of an oval fitting into the area indicated in figure 4.14, as follows:

$$s_{k_{Lit1}} = 2\pi\sqrt{\frac{50^2 + 70^2}{2}} \tag{4.3}$$

where 50 and 70 represent the lengths of the oval major and minor axes. Due to the size of the generator and the period of over 10 minutes for Lit 2, the flightpath is modelled as three separate elements, with a smooth ascend to zenith while moving upstream, and dive to continual figure 8 type loops during down and cross stream. From the literature results presented, s_k was derived as the sum of: two straight diagonals for the dive and climb section; a semicircle at zenith while transitioning from up stream to down stream; and 28 loops while moving cross stream. This is shown numerically as follows:

$$s_{k_{Lit2}} = 2\sqrt{600^2 + 1000^2} + 300\pi + 28(2\pi \times 50) \tag{4.4}$$

4.1.3.1 Device dimensioning

The parameter analysis of the kite carousel was expanded to investigate the effect of different carousel dimensions on optimal flightpath and power output. In order to maintain consistency the same parameters are used for the parameters study as in section 4.1.2.1. This section will refer back to the results available in literature and how they compare with the flightpath outcomes of this study. To this extend the range of carousel dimensions and operating conditions investigated were taken to fit between the cases presented in literature. The curves in figure 4.15 show the resulting power curves for various carousel dimensions. Here the power coefficient is taken wit respect to A_{geo} as this is directly dependant on carousel dimensions and thus can potentially be used to determine device performance based on size. For clarity the datapoints for each device dimension r_c/l_T have a spline fitted through to show how the power curves develop. As such the maximum $C_{p_{geo}}$ for each carousel dimension is taken and used to produce figure 4.16; which shows a peak $C_{p_{geo}}$ of 0.0047 at $r_c/l_T \approx 0.065$. While this powerfactor may appear extremely low at first glance, it is important to realize that it is only used here to show the effect of device dimensions on output. For a more accurate

representation of the percentage of available power extracted from the flow, one should refer to the swept area, A_{swept}.

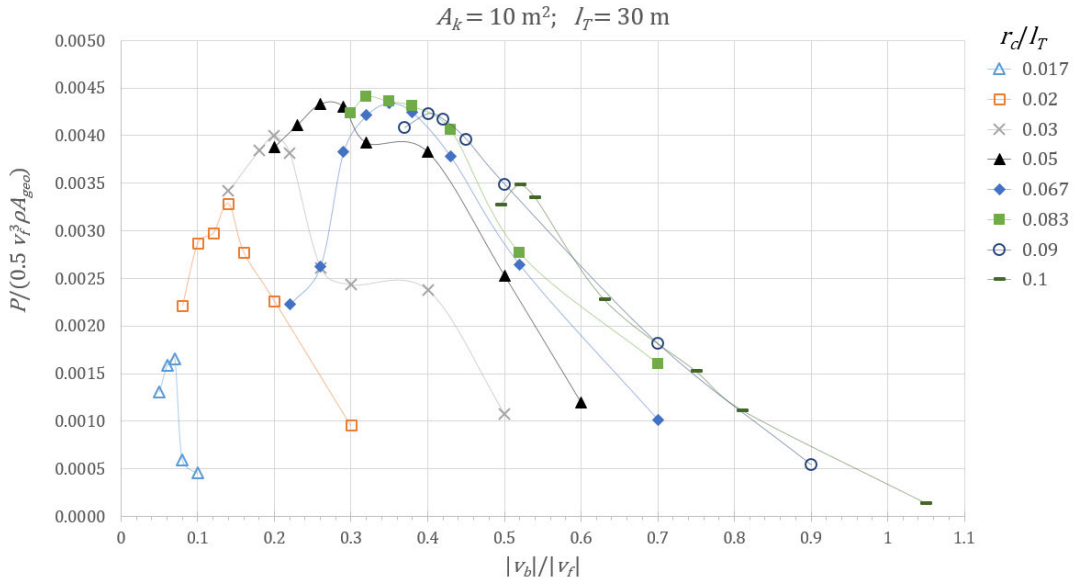

Figure 4.15: Power curves for $|v_b|/|v_f|$ range 0.017 - 0.14

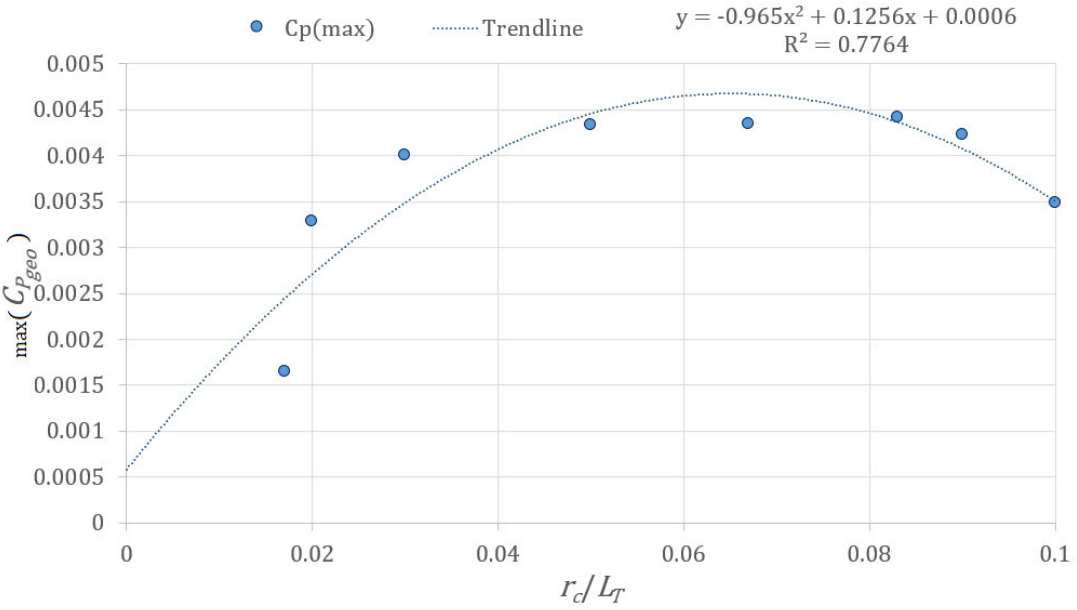

Figure 4.16: Trend of maximum $C_{P_{geo}}$ for carousel dimensions

Similarly, the optimal tip speed ratio, $|v_b|/|v_f|$, for each carousel dimension was evaluated and is shown in figure 4.17. This figure shows a linear relationship between carousel sizing and tip speed ratio. Showing that as the relative carousel radius increases the optimum tip speed ratio does as well.

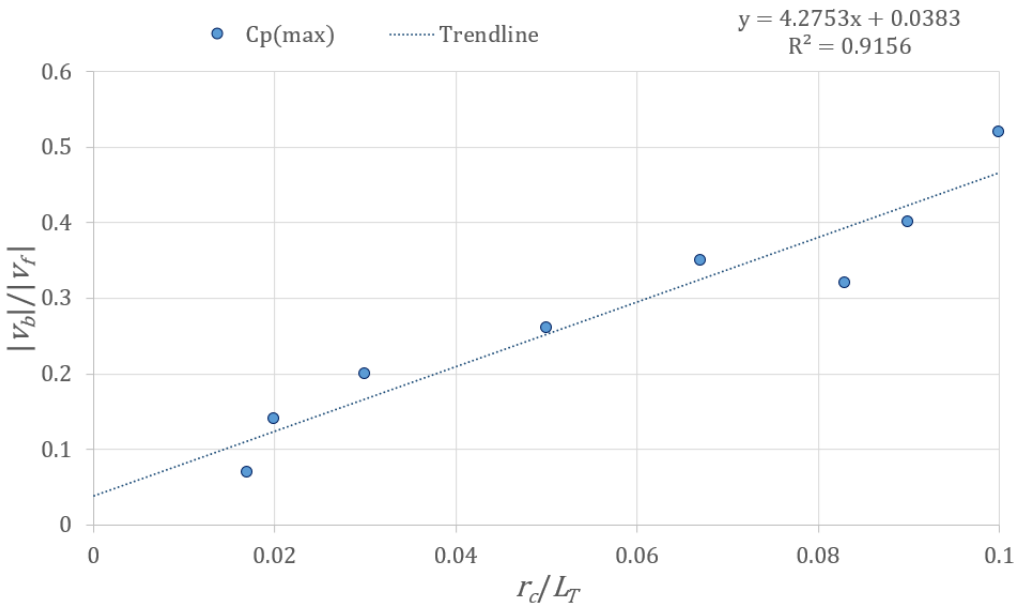

Figure 4.17: Trend of optimal tip speed ratio for carousel dimensions

Although there is a noticeable progression in power curves between carousel dimensions in figure 4.15, it is noted that the progression in flightpath shape shows similar characteristics as discussed regarding figure 4.8. Particularly regarding at points of maximumum power coefficients, as shown in figure 4.18, for $|v_b|/|v_f| = 0.35$ with $l_T/r_c = 0.083$.

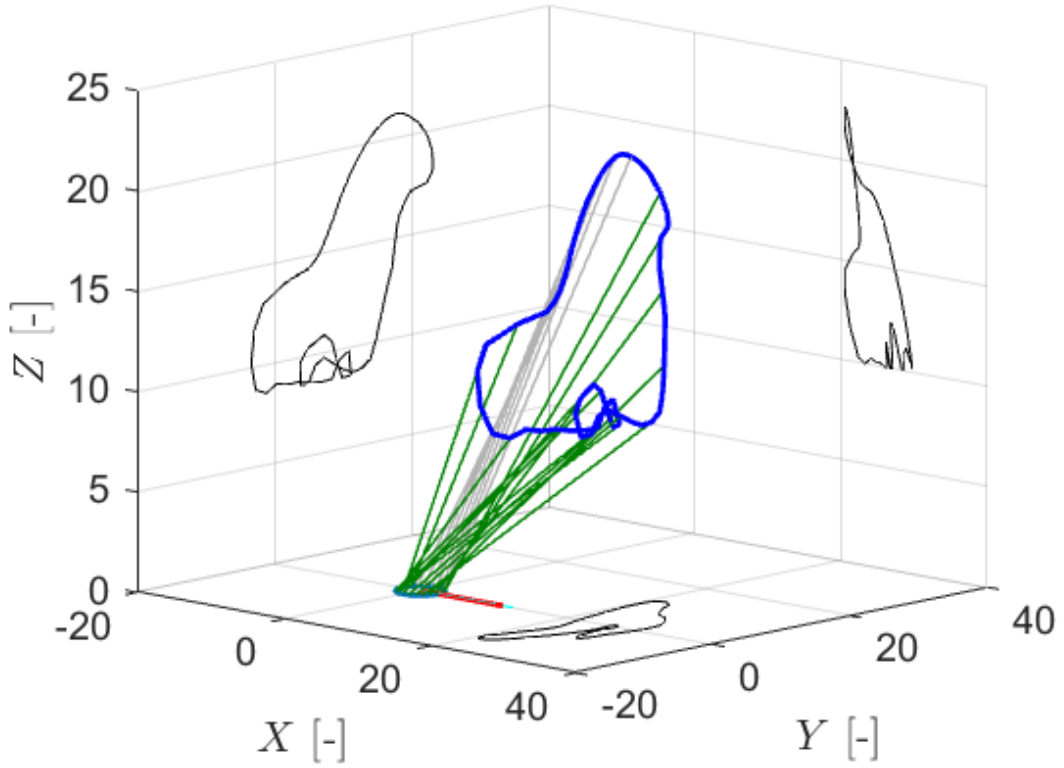

Figure 4.18: Optimum flightpath for $|v_b|/|v_f| = 0.35$ with $l_T/r_c = 0.083$

This figure clearly shows how during the upstream portion of carousel movement the kite ascends to minimize the effective resistance, and subsequently dives and maintains its velocity through flying figure 8's during the down stream portion of the carousel cycle, until it reduces kite velocity ones again in preparation of the upstream portion. These effects on power and kite velocity are shown in figure 4.19. Here the clear correlation between reduced kite velocity during the upstream portion of the carousel rotation is shown. The increase of the velocity during it's dive while positioning for crosswind flight during the cross- and downstream portions is also visible. Although the majority of the increase in power during the second half of the carousel period in figure 4.19b is due to the adjustments to α as in figure 4.11.

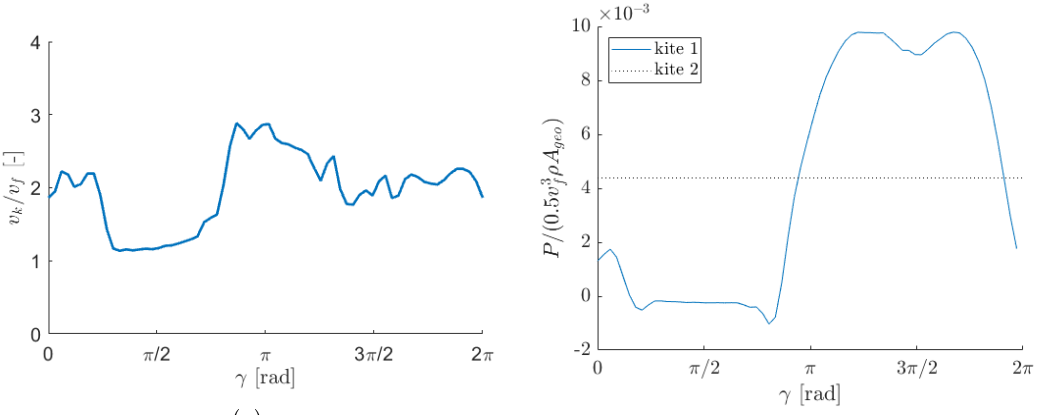

(a) (b)

Figure 4.19: Kite velocity and power for $|v_b|/|v_f| = 0.35$ with $l_T/r_c = 0.083$

4.1.3.2 Flightpath comparison with literature results

Comparing these results with those found in literature as per table 4.9, it is apparent that when determining the power coefficient of a carousel scaling remains an issue. Due to the substantial difference in scale highlighted in figure 4.14, and the potential dependency of the power coefficients defined by A_{geo} and A_k on device scale indicated in section 4.1.3; additional runs were done for a carousel with a tether length of 60 m, albeit still in a submerged flow of 2 m/s and a kite area of 10 m^2. Figures 4.21, 4.20, and 4.22 show these results. For clarity all the results for the various values of r_c/l_T are shown according to the actual tether length used to compute the results. In order to compare the simulation results with those available in literature, the results are scaled to a ratio of $\sqrt{A_k}/l_T = 0.0875$, as equal to the device scaling in figure 4.18.

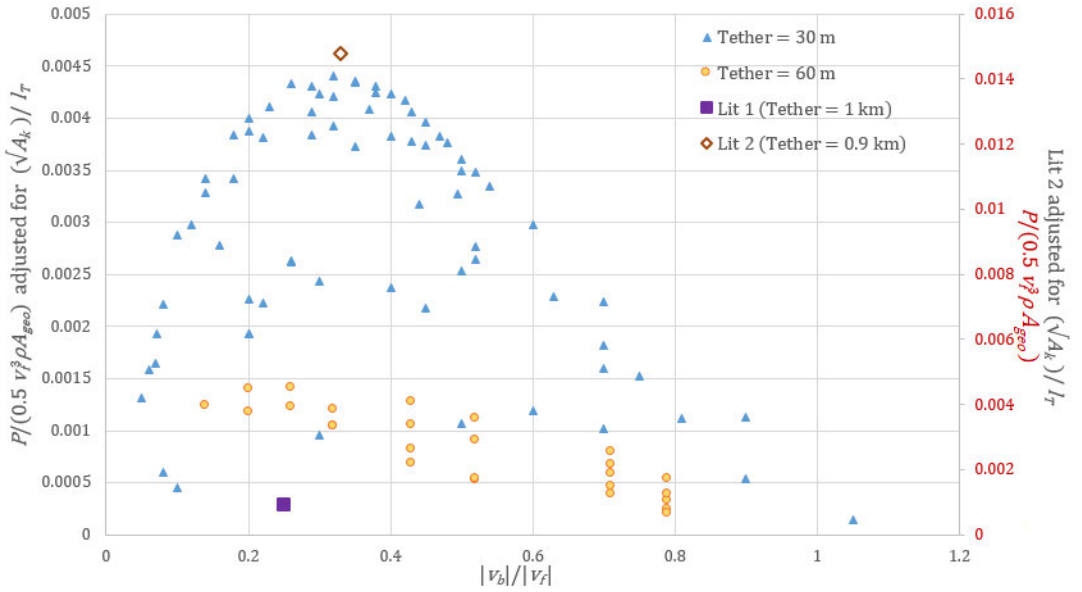

Figure 4.20: Effect of scale on full results, using $C_{P_{,geo}}$, adjusted for kite area

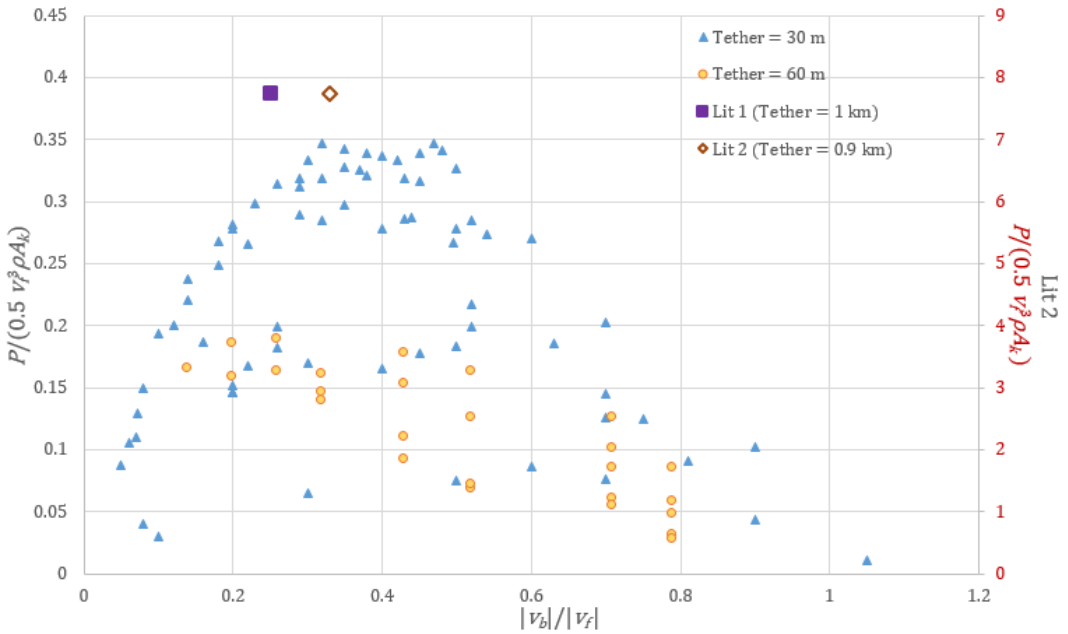

Figure 4.21: Effect of scale on full results, using C_{P_k}

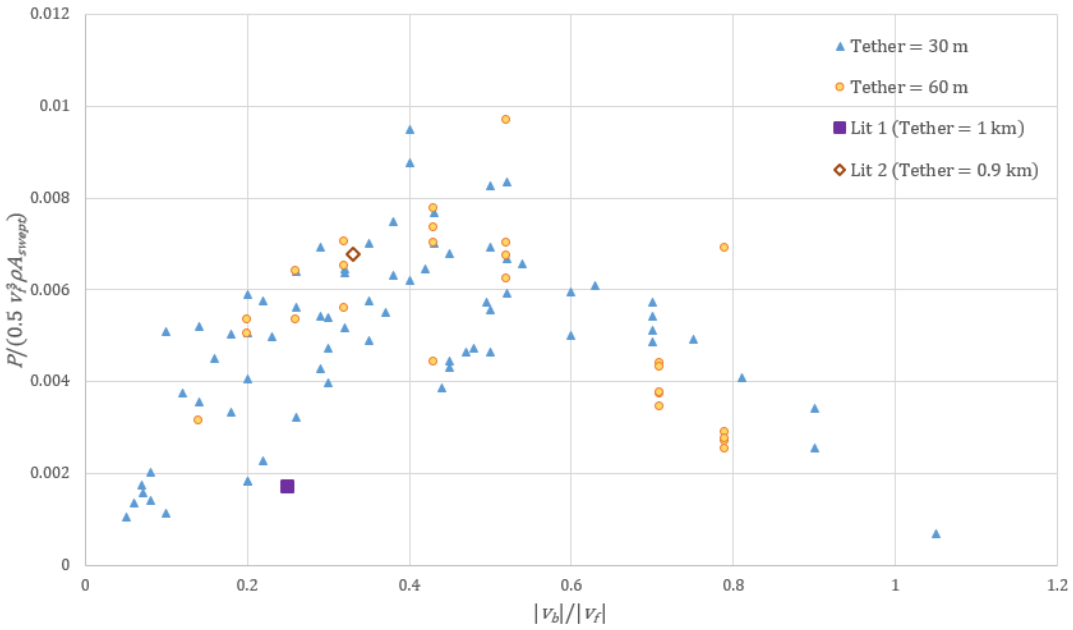

Figure 4.22: Effect of scale on full results, $C_{P_{swept}}$

While figures 4.20, 4.21 show bias in $C_{P_{geo}}$ and C_{p_k} due to tether length, particularly with respect to the Lit 2 results; using A_{swept}, as in figure 4.22 to define the carousel power coefficient produces scalable results. As this definition uses the swept area described by only the kite, it provides a more objective version of the power coefficient that is not directly dependent on device dimensions, but does account for the effect of kite size. While this is a more accurate definition of the device efficiency, it is not effective as a design tool as it is based on the outcome of the flightpath optimizations resulting from device parameters, rather than the parameters themselves. Hence, for the purpose of device sizing for the duration of this chapter the focus will be on the optimum device with a 30 m tether. Despite the various definitions of power coefficient, in each case the overall optimum operating condition appears to lie at $|v_b|/|v_f| \approx 0.4$.

The flightpaths resulting in $C_{P_{swept}}$'s of > 0.008 in figure 4.22 are shown in figure 4.23. These appear to have similar shapes, particularly when compared in the same figure in 4.23f there is a similar trend seen in how the kite moves upward in preparation of being pulled upstream and descends while moving cross stream into a dive as the carousel rotates upstream, with a single loop before moving back into starting position. This aligns with the presumptions made regarding results in figure 4.12. Although here the initial position remained constant the different carousel operating conditions and

dimensions show a similarity in flightpaths regarding power coefficient based on area swept by the kite.

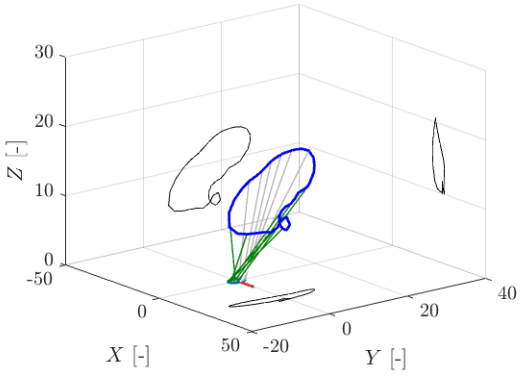

(a) $C_{P_{swept}} = 0.0096$, $|v_b|/|v_f| = 0.52$, $r_c/l_T = 0.017$

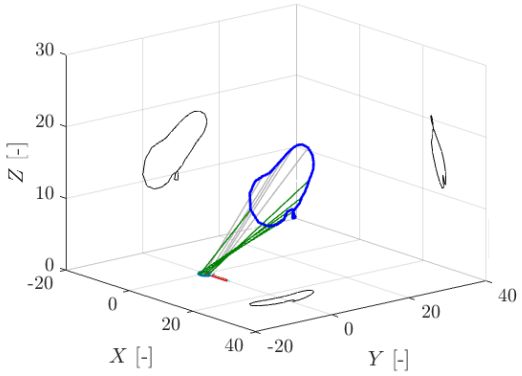

(b) $C_{P_{swept}} = 0.0087$, $|v_b|/|v_f| = 0.4$, $r_c/l_T = 0.05$

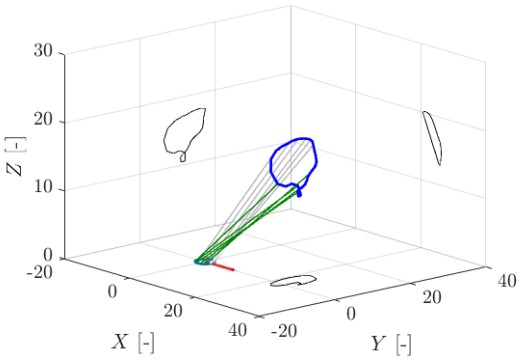

(c) $C_{P_{swept}} = 0.0084$, $|v_b|/|v_f| = 0.52$, $r_c/l_T = 0.067$

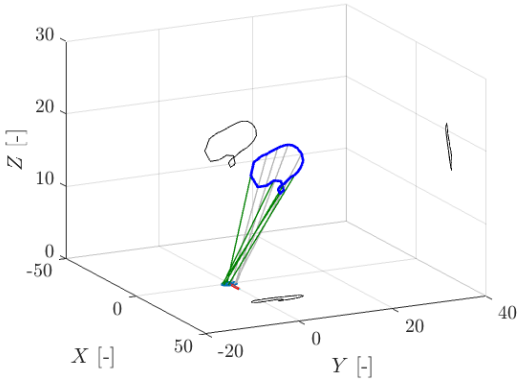

(d) $C_{P_{swept}} = 0.0083$, $|v_b|/|v_f| = 0.5$, $r_c/l_T = 0.05$

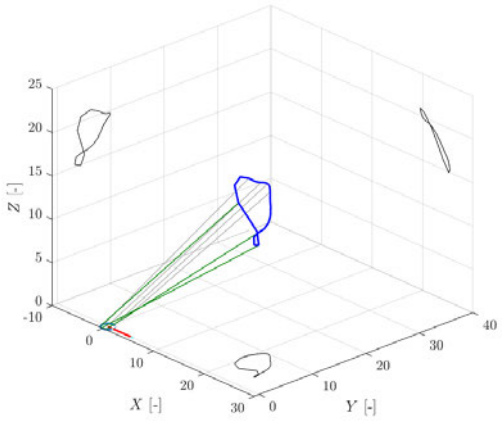

(e) $C_{P_{swept}} = 0.0095$, $|v_b|/|v_f| = 0.4$, $r_c/l_T = 0.033$

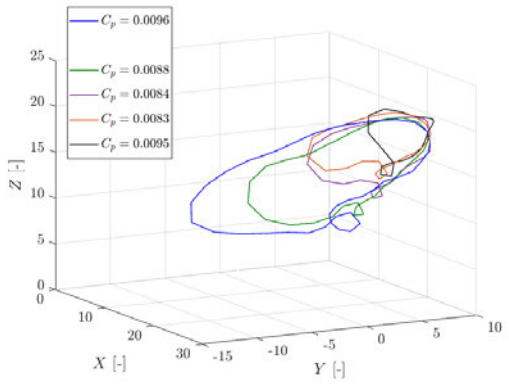

(f) all

Figure 4.23: Flightpath results for high power coefficient

4.1.4 Multiple kites

One of the benefits of the carousel design is that multiple kites can be added to a single device to increase and smooth device output. Here a crucial limit to number of kites is the risk of collision and entanglement. To this end it may be beneficial to look into high values of r_c/l_T for large scale devices as done in [2], which although a single kite may have a lower relative power output, this is mitigated by the fact that more kites can be used.
In this section the effect of having up to ten kites attached to the carousel is investigated. To this end it is presumed that the kites all fly the same flight path and the spacing is large enough that there is no interference from kite wakes.

For the purpose of this study the optimum carousel configuration based on figure 4.15, with its flightpath shown in figure 4.18, is used. Figure 4.24 shows the addition of kites throughout a carousel cycle. The equal phasing of the kites is clear here. It is noted that with multiple kites starting at various locations, a more robust start-up procedure would be required to result in the overall periodic run displayed here.

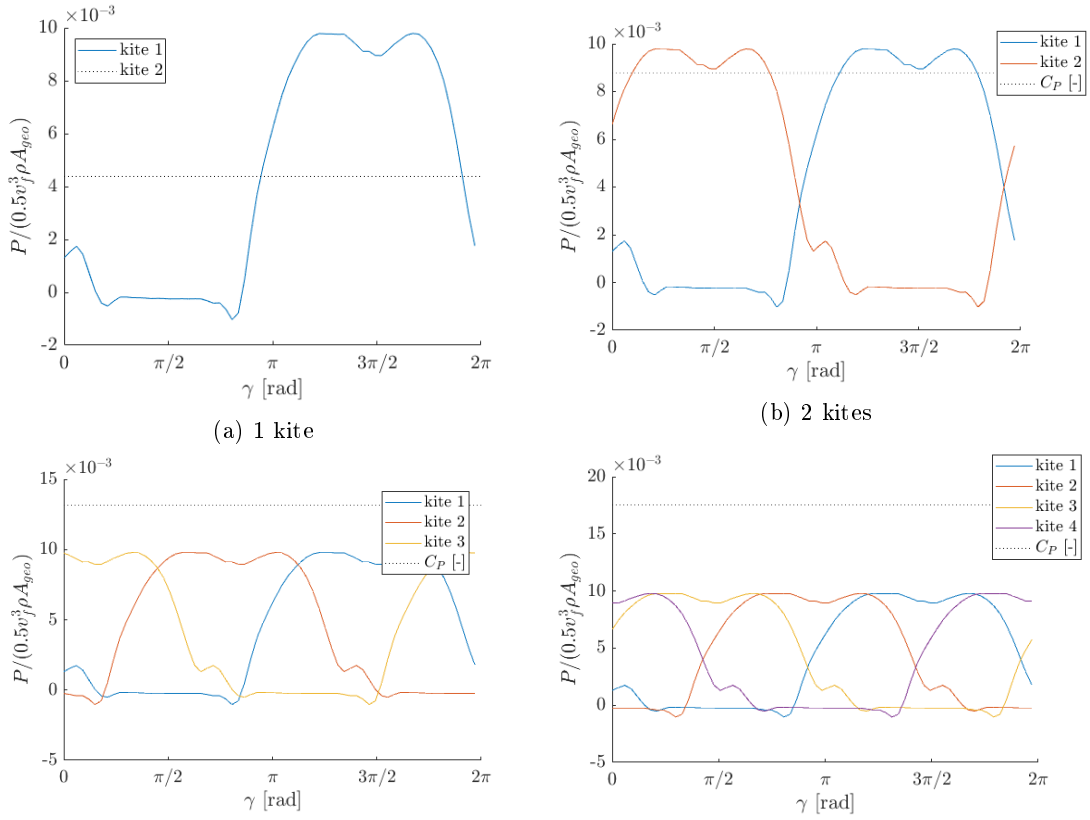

(a) 1 kite

(b) 2 kites

(c) 3 kites

(d) 4 kites

Figure 4.24: Power output for carousel with multiple kites

The overall power output and average power over a cycle is shown for comparison in figure 4.25. This figure includes up to 10 kites to illustrate the smoothing effect as kites are added and clearly shows the average power increasing with the number of kites. However due to the periodic nature of the generated power, the smoothest output is seen where they the number equals to a powerfunction with base 2, ie. 2, 4, 8, and further. This is due to the periodicity of the cycles where with an uneven number of kites there will be moments when more kites are pulling a single kite upstream and vice versa, leading to a less stable overall power. However, as soon as the carousel includes more than one kite, if evenly spaced, there is no need to switch the generator from generating to motoring part of the cycle as the additional kites would provide the force needed to pull a kite upstream.

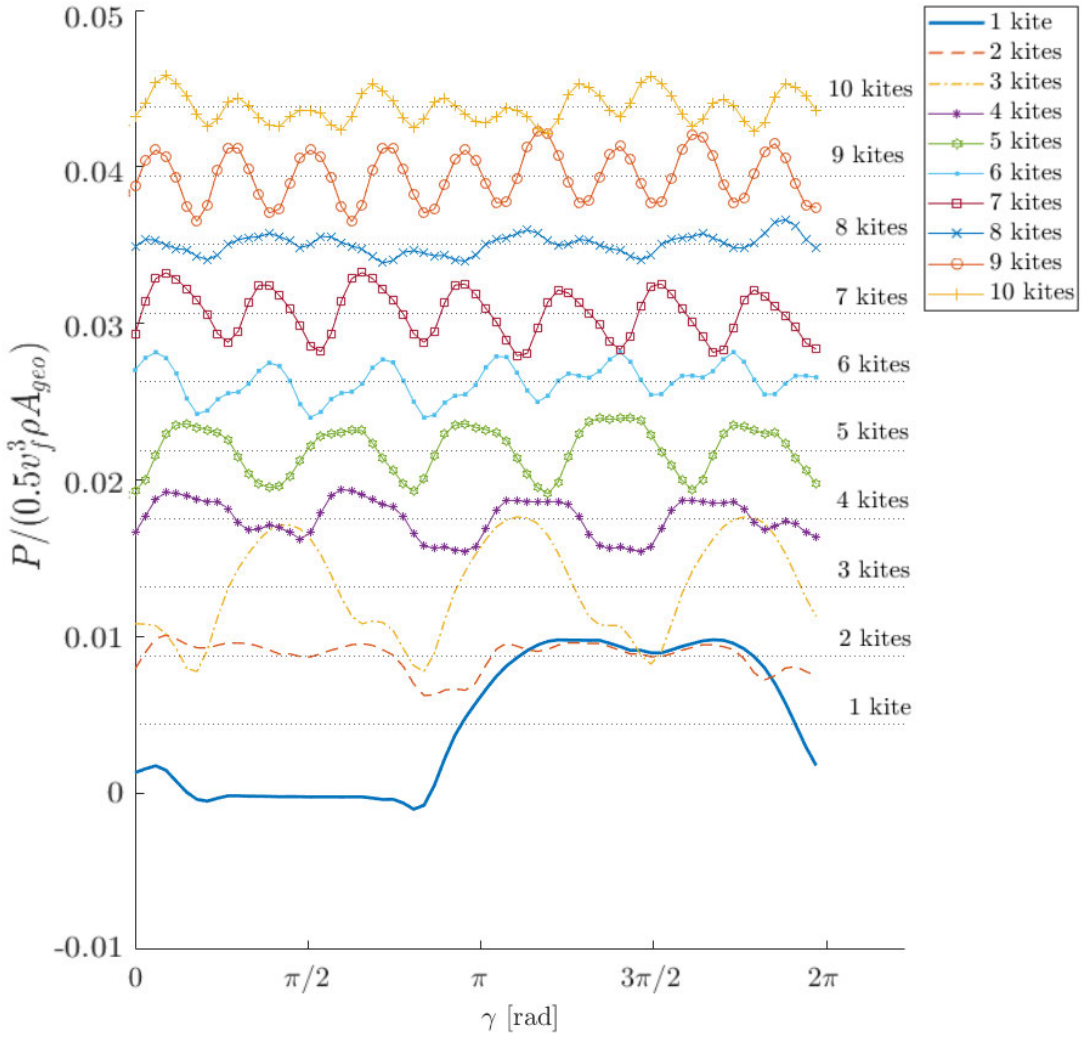

Figure 4.25: Sum and average output for carousel with multiple kites, with $r_c/l_T = 0.083$

As figure 4.25 shows one could theoretically continue adding kites to a carousel to increase the power output. However, in practice eventually interference effects between kites would have to be taken into account. More importantly though is the risk of entanglement. In practice the kites would not be flying with perfect control in an ideal constant flow. As such the limit to the number of kites feasibly added to a carousel depends on their location with respect to one another throughout a full carousel period. To illustrate this the tethers for the 4 scenarios of figure 4.24 were divided into 100 discrete sections of 0.3m each, allowing for a check of the distance between points on each tether. Table 4.11 shows an initial computation of the minimum distance

between tethers throughout a cycle. As the kites follow the same flightpath the minimum distance kites with the same angle between the tether base attachments to the carousel, $\Delta\gamma$, will be equal as they are presumed to follow the same flightpath. Due to the nature of this flightpath the minimum distance between kites would occur in adjacent kites during the dive and cross stream sections where the kite is flying in figure 8's to maintain its velocity. In scenarios where a flightpath crosses itself with a large loop as in 4.8c, or the length of the flightpath is substantially shorter as in 4.8f this minimum will reduce even further. For the purpose of this section, the focus is the overall minimum distance between the kites and how this relates to the chance of tether crossing or entanglement throughout a cycle; instead of where and when this minimum distance occurs.

Table 4.11: Minimum distance between tether lines for multikite carousel, with $\Delta t = 0.3$ s

Number of kites	$\Delta\gamma$[rad]	Minimum distance [m]
2	π	2.55
3	$2\pi/3$	1.52
4	$\pi/2$	1.06
5	1.257	0.62
5	2.513	2.01
6	$\pi/3$	0.21
7	0.89	0.18
7	1.798	1.20
7	2.688	2.31
8	$\pi/4$	0.17
9	0.698	0.12
9	2.793	2.40
10	0.628	0.20
10	1.885	1.27

In figure 4.19 it is shown that the kite reaches a maximum velocity of three times the flow velocity, which in this case corresponds with $3 \times 2 = 6$ m/s. The minimum

distances evaluated here were computed with the simulation timestep of $\Delta t = 0.3$ s, which corresponds to a potential distance travelled of 2 m. To this end all the scenarios except the two kites could indicate a potential line crossing.

To provide further clarity further analysis is done by interpolating tether positions with a timestep of $\Delta t = 0.03$ s, where the potential distance travelled in a timestep is 0.2 m. The results of this analysis are shown in table 4.12, where it shows that for the larger $\Delta\gamma$ cases the changes are minimal. However for a higher number of kites, the smallest $\Delta\gamma$ results in at times far smaller numbers. With the adjusted minimum crossing distance of 0.2 m it can be assumed that any carousel configuration with more than 5 kites runs the risk of getting their lines crossed throughout a cycle.

Table 4.12: Minimum distance between tether lines for multikite carousel

		minimum computed distance [m]		
Kites	$\Delta\gamma$ [rad]	$\Delta t = 0.3$ [s]	$\Delta t = 0.03$ [s]	between bases
2	π	2.55	2.54	5.00
3	$2\pi/3$	1.52	1.48	4.33
4	$\pi/2$	1.06	1.04	3.54
5	1.257	0.62	0.56	2.94
5	2.513	2.01	2.02	4.76
6	$\pi/3$	0.21	0.04	2.50
7	0.89	0.18	0.04	2.15
7	1.798	1.20	1.21	3.91
7	2.688	2.31	2.32	4.87
8	$\pi/4$	0.17	0.02	1.91
9	0.698	0.12	0.14	1.71
9	2.793	2.40	2.41	4.92
10	0.628	0.20	0.03	1.55
10	1.885	1.27	1.29	4.05

Figure 4.26 illustrates how the minimum crossing distance and minimum distance between tethers at different angles of tether attachment to the carousel relate. This figure clearly shows the benefit of a larger distance between kite attachment points to with regards to tether proximity. As per this graph a maximum of 8 kites should not be exceeded for this size of carousel.

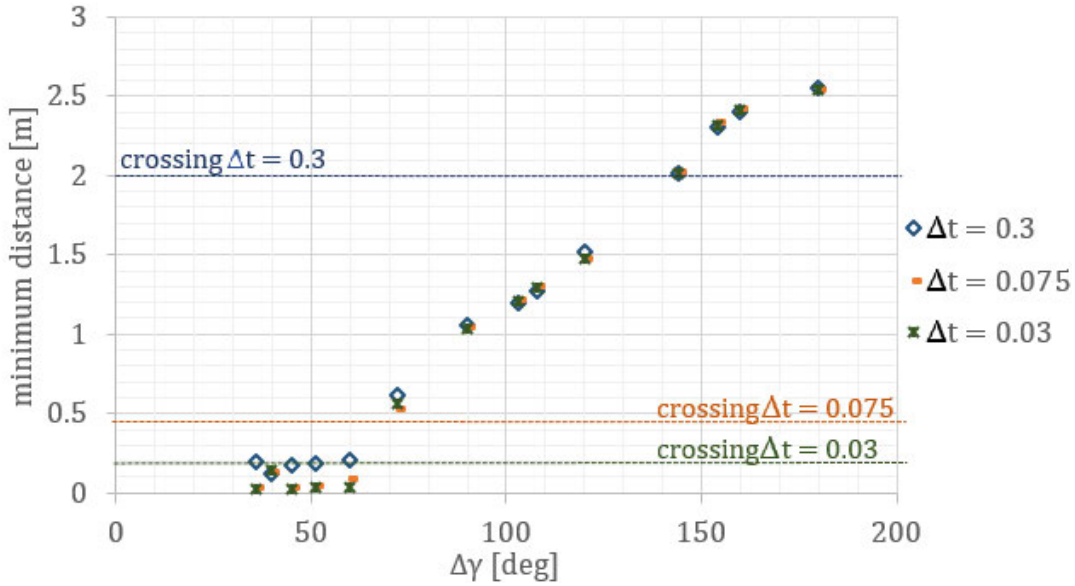

Figure 4.26: Minimum distance between tether lines for multikite carousel

4.2 Case Study

The case study presented here was designed to illustrate how the methods developed can be applied to provide indications of a sized device output in a flow. To this end a submerged carousel is shown in conditions similar to those found at a low speed tidal site. The results from the parameter study will be used to size a carousel device and show the effect of varying operating conditions throughout a tidal cycle.

4.2.1 Environmental parameters

For model inputs, an flow velocity v_f with a range of 0.5-2.2 m/s is used, as indicated in table 4.13. It is further presumed that the kite would be operating sufficiently below the surface such that the wave effect on v_f is negligible.

Table 4.13: Parameters used for simulating case study situations

Parameter	unit	value
z	m	80-100
v_f	m/s	0.5-2.2

A logarithmic profile is applied as shown in figure 4.27. The flow modelled is smooth and uni-directional.

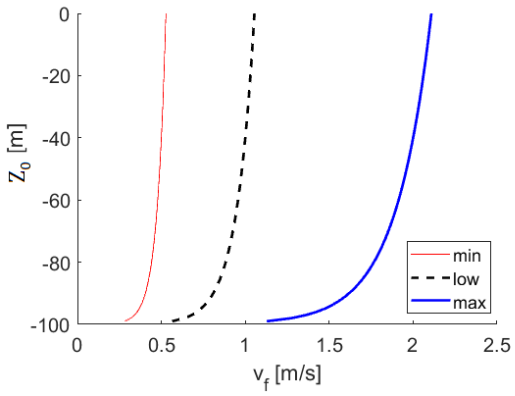

Figure 4.27: Flow profile assumed for case study

4.2.2 Resulting output

Due to the limits of this model with respect to scalability, the results of this case study are given using a carousel with a 30 m tether, as used for the parameter study in section 4.1.3.1. Table 4.14 shows the carousel dimensions used to simulate the carousel at peak flow and the resulting swept area and predicted power output. Here a portion of the tether mass is included in the estimation for kite mass, to account for weight of the tether required to support the kite forces produced.

Table 4.14: Carousel dimension and output

Variable	unit	value
ρ	kg/m^3	1025
v_f	m/s	2.2
A_k	m^2	10
m_k	kg	580
l_T	m	30
r_c	m	2.5
T	s	22.4
s_k	m	88.6
A_{sweep}	m^2	786.4
$P_{1\ kite}$	kW	14.1
$P_{8\ kites}$	kW	64

Figure 4.28 shows a rough estimate of a representative tidal cycle. It is noted that when the tide switches direction, the carousel adjusts it's period with respect to the flow direction. As such the generator would continue to rotate in a single direction.

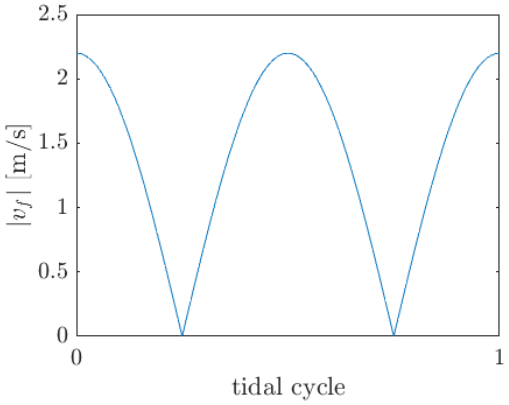

Figure 4.28: Simple tidal cycle flow velocity

Using the flow velocities from this cycle, it is presumed that the generator period is controlled such that $|v_b|/|v_f|$ remains constant. Subsequently the average power output over a cycle is reduced to 8 kW, for a single kite carousel, and 64 kW for a carousel with 8 kites. These results assume the carousel continues rotating with a tip speed

ratio of 0.35 up until the flow velocity reaches zero. Realistically a generator would have operational limits that would limit the minimum rotation velocity. At low flows this limit would be reached, at which point, the flightpath can be adjusted to operate optimally at a higher tip speed ratio. Alternatively, to reduce operational complexity at very low flows the carousel could be stopped with the kites held in a stationary position.

4.3 Discussion

As briefly indicated in the previous section the 64 kW average output resulting from the case study is an optimistic estimation due to the high level assumptions made to power conversion. First off, the resulting power represents the mechanical power potential of the carousel, the losses during conversion are not included. As a perfect generator this result shows optimal operating conditions from the perspective of the kite. In reality, generator specifications and limits may result in alternative results. However, determining the optimum flightpaths would form an essential base of this further study. This model indicates the potential for a carousel type device to generate power at a low flow tidal site, which may not be exploitable with horizontal axis turbines. Furthermore Minesto [92] with their DeepGreen technology have demonstrated that generation in such conditions is possible using hydrofoils to operate as kites in cross flow conditions. It is important to remember the trade-off introduced by using ACADO as optimization tool between reducing the stepsize to allow for smoother curves; and allowing for more development of the flightpath track by increasing the stepsize. Ideally, this initial pass will be followed up with further iterations using smaller time steps to create smoother flightpaths.

In section 4.1.4, it is demonstrated that adding more kites to a carousel will increase the device power coefficient, but is limited due to collision risk between kites. This collision risk is further enhanced with flightpath complexity where kites may end up crossing resulting in tangled lines. This can be mitigated by adjusting the flightpath to a larger smoother loop. While the resulting would be less efficient for a single kite, the potential for including additional kites could potentially result in an overall higher power coefficient. The sizing of the carousel in this study was limited to the data

produced throughout the parameter study, due to the indicated bias of the results to device scaling. As such for a similar case where further depth is available to allow for longer tethers it may prove to be beneficial to investigate larger devices.

Chapter 5

Conclusions

5.1 Conclusions

Through this work a number of conclusions were reached.

Chapter 3 showed the development process of the numerical kite model used for the parameter study. In doing so it demonstrated that with rudimentary control of kite power and turning settings it is possible to show net power generation. However, it is important to consider the numerous variables influencing kite behaviour other than merely the control inputs, such as orientation and velocity. As one can reasonably expect considering a system of this complexity it is confirmed that an optimization strategy is required for accurate analysis of varying system dimensions.

Addressing the second thesis objective stated in section 1.2.2; the dimensionless analysis of kite flightpaths optimized for power generation concludes that a 5 m diameter carousel with eight kites could produce an average of 64 kW of power in a representative tidal cycle with a peak flow of 2.2 m/s at an average depth of 90 m. Although more kites would allow for a higher power output the number of kites is limited to 8 due to limits added to prevent entanglement. The power output was computed using aerodynamic coefficients represented in literature, which considering the assumptions made may be optimistic. Additionally, it is assumed that there are no mechanical losses due to a perfect generator. In reality generator design will be impactful on overall device efficiency.

The parameter study performed investigated the impact of altering two critical de-

vice dimensions, carousel radius ,r_c, and tether length, l_T; satisfying the first thesis objective. These dimensions were made dimensionless as the ratio r_c/l_T. Operational parameters were also included in the study as the ratio between absolute flow velocity $|v_f|$ and the velocity of the base of the tether attached to the carousel $|v_b|$.

Flighpath optimization throughout the parameter study showed trends in how an optimum flightpath develops depending on device dimension and operation. It is shown that as the tether attached to the carousel moves upstream tether tension is minimized by increasing kite altitude and slowing kite velocity, once the carousel rotates cross-stream the kite dives in the same direction to maximize positive tether tension, while looping around to match carousel movement and adding some figure 8 type manoeuvres, where the $|v_b|/|v_f|$ ratio is low enough to maximize the projection of the tether tension vector along v_b while moving downstream. The novelty of this finding is that this optimized flightpath for a kite carousel has very similar manoeuvres found in the pumping kite type generator device switching between tether extension and retraction [38, 39].

Results from this analysis showed a peak in power coefficient of $C_{p_{geo}} = 0.0047$ at $r_c/l_T = 0.065$. $C_{p_{geo}}$ is a function of the geometric area, determined by the physical dimensions of the carousel, rather than the actual area swept by the kite during a carousel period. Due to this geometric area being an order of magnitude larger than the actual swept area, this representation of the power coefficient leads to power coefficient that is an order of magnitude smaller than if it were defined by the kite swept area. Although the area directly swept by the kite produces a more accurate representation of the fraction of power extracted by the kite throughout a carousel period, the geometric area was used to determine the power coefficient used to make design considerations due to its direct relationship to device dimensions. With regards to carousel operation, a trend is shown between carousel sizing and tip speed ratio. As the carousel radius increases relative to the tether length, the optimum tip speed ratio of the carousel base does so as well.

A comparison with literature and additional model runs shows a strong dependency of the computation of dimensionless power on the length of the tether due to definition of the geometric swept area used. An alternative definition of swept area dependant on

the length of the flightpath shows to be less subjective to this scaling issue. However, as it is dependant on flightpath length, this is less appropriate for carousel design purposes. Similarly the kite area A_k is not factored into the computation for A_{geo}, thus a scaled ratio, $\sqrt{A_k}/l_T$ applied to the power factor results in order to allow for comparison between the parameter study results and those presented in literature. Despite these attempts at creating a truly dimensionless expression of power output to objectively compare results of different device sizes; scaling remains an issue due to the dependence of power output on attainable flightpaths and kite size, as evidenced through comparison of results with those concluded in other studies. It is shown that expressing the power output as a function of flightpath does show alignment of results from the parameter study with two different tether lengths, as well as with the literature examples used as references. While this allows for comparison of device efficiency, the separation between dimensionless power and carousel dimensions excludes this as a viable method for determining device parameters. Looking at the power expressed as a function of the kite swept area shows an alignment in optimum flightpath shape, where the flightpath is kept as small as possible while still providing as much positive input into the net power as possible. However, as ultimately one would desire the highest overall power output possible for a certain device dimension it is suggested to refer to the results gained expressing power as a function of the device dimensions. Doing this would lead one to design a device that makes the most use out of the flow available. In most tidal sites this would likely be limited by the minimum channel depth, subsequently the carousel radius could be determined through the optimum r_c/l_t ratio for that tether length

One of the main advantages of the carousel design is the ability to add multiple kites to a single carousel to increase the overall power yield and smooth the power output. This is illustrated by a cumulative power output of a number of kites equally spaced around the carousel. The assumption of ideal flow and control conditions are maintained throughout this demonstration, allowing for identical flight paths to be flown by each kite attached to the carousel. It is important to realize that due to the definition of power with A_{geo}, the power coefficient increases with the number of kites as the geometric area is determined by the carousel dimension and independant of the number of kites attached. To this end each kite added increases the overall power output

without the device taking up more space in the flow, leading to the conclusion that the higher number of kites you can add to a carousel, the more beneficial to the overall device performance. The number of kites added to the carousel is limited by the risk of entanglement. As such a check is made looking at the minimum distance between tether lines for a multi-kite carousel, leading to the conclusion that for a carousel with a 30 m tether and a 2.5 m carousel radius no more than 8 kites should be attached to avoid lines entangling.

Finally, to answer the overarching research question of this thesis, the kite carousel can be considered a realistic design for power extraction from a fluid flow. Through the numerical model and flightpath optimization it has been shown that through correct control it is possible to produce a net power with a kite carousel in a fluid flow in terms of engineering. However, it must be acknowledged that although economic and environmental feasibility were beyond the scope of this thesis, these are important factors to consider in the overall feasibility of the kite carousel as a design. A case study has shown a power output of 64 kW would be possible; this must be put in context by considering within the framework of alternative technologies in development. For example, in Scotland's Pentland Firth, Meygen is installing turbines with 1.5 MW capacities [93], and in Wales Minesto's Deep Green technology [92] has shown commercial output of 500 kW. In order to address the 'true' feasibility of the kite carousel as a viable design for further development the economic case must be combined with the engineering output, while considering environmental impacts, to see how it compares to alternative designs.

5.2 Limitations and further work

This thesis highlights the potential of the kite carousel as a renewable energy device. Due to the high level nature of this model it can be view of the ground work for further model iterations where allowances can be made to reduce the model assumptions made. With real-world data being fed into the model through additional kite testing as shown in chapter **??**, the numerical model can incorporate specific kite-flying characteristics. Similarly, expanding the carousel model with a power take off unit would show the greater smoothing effect of adding multiple kites to a carousel. Finally, work can be

done on including a variable flow field input at which point a kite controller would be applied to illustrate kite capabilities to following the optimised flightpath.

5.3 Industry impact

The model presented in this thesis as illustrated through the case study in chapter 4 can be used by industry as a tool for preliminary investigations of potential tidal sites where a submerged kite carousel is being considered.

This thesis has highlighted both benefits and difficulties of the carousel model being applied in a fluid flow. The range and flexibility of flightpath gives it a large operating window with the ability to adjust to changes in flow conditions. However, the size and complexity of the device presents concerns; particularly when looking to install a device in a more hostile environment such as a tidal flow. In a tidal flow maintenance and repairs are exponentially more involved than with land-based devices, due to the small windows of accessibility and additional equipment required to access submerged structures. While this thesis has shown beneficial flight patterns capable of producing energy, these are highly reliant on a finely tuned control system capable of following such complex patterns. As such, it is important to focus on developing robust systems to ensure operational success. At the time of writing this thesis the industry is not yet at that point. Progression in development of simpler, single kite systems is a good step towards potentially one day revisiting a design of this magnitude.

Bibliography

[1] P. Williams, B. Lansdorp, and W. Ockels. Optimal Trajectories for Tethered Kite Mounted on vertical axis generator. In *AIAA Modeling and Simulation Technologies Conference and Exhibit*, Hilton Head, South Carolina, August 2007.

[2] L. Fagiano. *Control of Tethered Airfoils for High-Altitude Wind Energy Generation.* PhD Thesis, Politecnico di Torino, 2009.

[3] A. Ghasemi, D.J. Olinger, and G. Tryggvason. Simulation of thethered underwater kites: three dimensional trajectories for power generation. In *ASME Power & Energy*, Charlotte, USA, June 2016.

[4] U. Fechner. A Methodology for the Design of Kite-Power Control Systems. 2016.

[5] D. A. Spera. Models of lift and drag coefficients of stalled and unstalled airfoils in wind turbines and wind tunnels. NASA nasa/cr -2008-215434, 2008.

[6] R E Sheldahl and P C Klimas. Aerodynamic characteristics of seven symmetrical airfoil sections through 180-degree angle of attack for use in aerodynamic analysis of vertical axis wind turbines. Technical Report SAND-80-2114, 6548367, March 1981.

[7] Richard Manasseh, S A Sannasiraj, Kathleen L McInnes, V Sundar, and Purnima Jalihal. Integration of wave energy and other marine renewable energy sources with the needs of coastal societies. *The International Journal of Ocean and Climate Systems*, page 1759313116683962, January 2017.

[8] Tabbi Wilberforce, Zaki El Hassan, A. Durrant, J. Thompson, Bassel Soudan, and A. G. Olabi. Overview of ocean power technology. *Energy*, March 2019.

[9] A. Cherubini, A. Papini, R. Vertechy, and M. Fontana. Airborne Wind Energy Systems: A review of the technologies. *Renewable and Sustainable Energy Reviews*, 51:1461 – 1476, 2015.

[10] M.J. Khan, G Bhuyan, M T. Iqbal, and J E. Quaicoe. Hydrokinetic Energy Conversion Systems and Assessment of Horizontal and Vertical Axis Turbines for River and Tidal Applications: A Technology Status Review. *Applied Energy*, 86:1823–1835, October 2009.

[11] Anny Key de Souza Mendonça, Caroline Rodrigues Vaz, Álvaro Guillermo Rojas Lezana, Cristiane Alves Anacleto, and Edson Pacheco Paladini. Comparing Patent and Scientific Literature in Airborne Wind Energy. *Sustainability*, 9(6):915, June 2017. Number: 6 Publisher: Multidisciplinary Digital Publishing Institute.

[12] Anny Key de Souza Mendonça and Antonio Cezar Bornia. Electric power generation in wind farms with pumping kites: levelized cost of energy and sensitivity analysis. *Research, Society and Development*, 9(7):666974528, June 2020.

[13] M. Nachtane, M. Tarfaoui, I. Goda, and M. Rouway. A review on the technologies, design considerations and numerical models of tidal current turbines. *Renewable Energy*, 157:1274–1288, September 2020.

[14] Stephen Joseph Sangiuliano. Turning of the tides: Assessing the international implementation of tidal current turbines. *Renewable and Sustainable Energy Reviews*, 80:971–989, December 2017.

[15] E. C. Malz, F. Hedenus, L. Göransson, V. Verendel, and S. Gros. Drag-mode airborne wind energy vs. wind turbines: An analysis of power production, variability and geography. *Energy*, 193:116765, February 2020.

[16] Alireza Mahdavi Nejad and Gretar Tryggvason. Power Generation Using Kites in a GroundGen Airborne Wind Energy System: A Numerical Study. *Journal of Energy Resources Technology*, 142(6), June 2020. Publisher: American Society of Mechanical Engineers Digital Collection.

[17] Simon Watson, Alberto Moro, Vera Reis, Charalampos Baniotopoulos, Stephan Barth, Gianni Bartoli, Florian Bauer, Elisa Boelman, Dennis Bosse, Antonello Cherubini, Alessandro Croce, Lorenzo Fagiano, Marco Fontana, Adrian Gambier, Konstantinos Gkoumas, Christopher Golightly, Mikel Iribas Latour, Peter Jamieson, John Kaldellis, Andrew Macdonald, Jimmy Murphy, Michael Muskulus, Francesco Petrini, Luca Pigolotti, Flemming Rasmussen, Philippe Schild, Roland Schmehl, Nafsika Stavridou, John Tande, Nigel Taylor, Thomas Telsnig, and Ryan Wiser. Future emerging technologies in the wind power sector: A European perspective. *Renewable and Sustainable Energy Reviews*, 113:109270, October 2019.

[18] Sarah M. Jordaan, Elizabeth Romo-Rabago, Romaine McLeary, Luke Reidy, Jamal Nazari, and Irene M. Herremans. The role of energy technology innovation in reducing greenhouse gas emissions: A case study of Canada. *Renewable and Sustainable Energy Reviews*, 78:1397–1409, October 2017.

[19] Jacob Ladenburg, Pablo Hevia-Koch, Stefan Petrović, and Lauren Knapp. The offshore-onshore conundrum: Preferences for wind energy considering spatial data in Denmark. *Renewable and Sustainable Energy Reviews*, 121:109711, April 2020.

[20] M. L. Loyd. Crosswind Kite Power. *Journal of Energy*, 4(3):106 – 111, 1980.

[21] A. Ghasemi, David J. Olinger, and Gretar Tryggvason. Computational Simulation of the Tethered Undersea Kites for Power Generation. November 2015.

[22] D.J. Olinger and Y. Wang. Hydrokinetic energy harvesting using tethered undersea kites. *Journal of Renewable and Sustainable Energy*, 7(4), 2015.

[23] A. E. Smentek-Duerr. *A Hydrockinetic Resource Assessment of the Flordia Current.* PhD Thesis, Florida Atlantic University, 2012.

[24] Magnus Landberg. The future of renewable energy | Minesto. http://minesto.com/our-technology.

[25] KiteGen looks to get wind-power off the ground. http://newatlas.com/kitegen-high-altitude-wind-turbine/20335/.

[26] Massimo Ippolito. KiteGen Research » KiteGen Carousel, April 2009. http://www.kitegen.com/en/products/kite-gen-carousel/.

[27] B. Houska and M. Diehl. Optimal Control of Towing Kites. In *Proceedings of the 45th IEEE Conference on Decision and Control*, pages 2693–2697, December 2006.

[28] C. Jehle and R. Schmehl. Applied tracking control for kite power systems. *Journal of Guidance, Control, and Dynamics*, 37(4):1211 – 1222, 2014.

[29] M. Diehl, H. Bock, and J. Schlöder. A Real-Time Iteration Scheme for Nonlinear Optimization in Optimal Feedback Control. *SIAM Journal on Control and Optimization*, 43(5):1714–1736, January 2005.

[30] J. Alvarez-Gallegos, R. Castro-Linares, and M.A. Zempoalteca-Jimenez. Robust Nonlinear flight Control of a Power-Generating tethered kite. In *2019 16th International Conference on Electrical Engineering, Computing Science and Automatic Control (CCE)*, pages 1–6, September 2019. ISSN: 2642-3766.

[31] Luís Paiva and Fernando A. C. C. Fontes. Optimal Control Algorithms with Adaptive Time-Mesh Refinement for Kite Power Systems. *Energies*, 11:475, February 2018.

[32] W. I. Ibrahim, M. R. Mohamed, and R. M. T. R. Ismail. Direct Power Control Method of Maximum Power Point Tracking (MPPT) Algorithm for Pico-Hydrokinetic River Energy Conversion System. In *InECCE2019*, Lecture Notes in Electrical Engineering, pages 691–703, Singapore, 2020. Springer.

[33] L. Fagiano, M. Milanese, and D. Piga. Optimization of airborne wind energy generators. *Int, J. Robust. Nonlinear Control*, 22:2055 – 2083, 2012.

[34] Zeashan Khan and Muhammad Rehan. Harnessing Airborne Wind Energy: Prospects and Challenges. *Journal of Control, Automation and Electrical Systems*, pages 1–13, July 2016.

[35] Shubham Tandon, Sathvik Divi, Michael Muglia, Christopher Vermillion, and Andre Mazzoleni. Modeling and dynamic analysis of a mobile underwater turbine system for harvesting Marine Hydrokinetic Energy. *Ocean Engineering*, 187:106069, September 2019.

[36] I. Argatov, P. Rautakorpi, and R. Silvennionen. Apparent wind load effects on the tether of a kite power generator. *Journal of Wind Engineering and Industrial Aerodynamics*, 99(10):1079 – 1088, 2011.

[37] Allert Bosch, Roland Schmehl, Paolo Tiso, and Daniel Rixen. Dynamic Nonlinear Aeroelastic Model of a Kite for Power Generation. *Journal of Guidance, Control, and Dynamics*, 37(5):1426–1436, 2014.

[38] Uwe Fechner, Rolf van der Vlugt, Edwin Schreuder, and Roland Schmehl. Dynamic Model of a Pumping Kite Power System. *arXiv:1406.6218 [cs]*, June 2014. arXiv: 1406.6218.

[39] R. van der Vlugt, A. Bley, M. Noom, and R. Schmehl. Quasi-Steady Model of a Pumping Kite Power System. *arXiv:1705.04133 [cs, math]*, May 2017. arXiv: 1705.04133.

[40] A. Pastor-Rodríguez, G. Sánchez-Arriaga, and M. Sanjurjo-Rivo. Modeling and Stability Analysis of Tethered Kites at High Altitudes. *Journal of Guidance, Control, and Dynamics*, 40(8):1892–1901, 2017.

[41] L. Salord Losantos and G. Sánchez-Arriaga. Flight Dynamics and Stability of Kites in Steady and Unsteady Wind Conditions. *Journal of Aircraft*, 52(2):660–666, 2015.

[42] B. Cadalen, P. Lanusse, J. Sabatier, F. Griffon, and Y. Parlier. Modeling and control of a tethered kite in dynamic flight. In *Innov'Sail 2017*, Lorient, France, June 2017.

[43] Nick H. Geschiere. Dynamic modelling of a flexible kite for power generation. Master's thesis, TU Delft, January 2014.

[44] Alireza Mahdavi Nejad, David J. Olinger, and Gretar Tryggvason. Numerical Modeling of Kites for Power Generation. American Society of Mechanical Engineers Digital Collection, December 2014.

[45] E. Schmidt, M. De Lellis Costa de Oliveira, R. Saraiva da Silva, L. Fagiano, and A. Trofino Neto. In-Flight Estimation of the Aerodynamics of Tethered Wings for Airborne Wind Energy. *IEEE Transactions on Control Systems Technology*, 28(4):1309–1322, July 2020. Conference Name: IEEE Transactions on Control Systems Technology.

[46] G. M. Dadd, D. A. Hudson, and R. A. Shenoi. Comparison of Two Kite Force Models with Experiment. *Journal of Aircraft*, 47(1):212 – 224, 2010.

[47] Antonello Cherubini. *Advances in Airborne Wind Energy and Wind Drones*. PhD Thesis, Sant'Anna University of Pisa, 2017.

[48] M. Canale, L. Fagiano, and M. Milanese. KiteGen: A revolution in wind energy generation. *Energy*, 34(3):355–361, March 2009.

[49] L. Fagiano, A. U. Zgraggen, M. Morari, and M. Khammash. Automatic Crosswind Flight of Tethered Wings for Airborne Wind Energy: Modeling, Control Design, and Experimental Results. *IEEE Transactions on Control Systems Technology*, 22(4):1433–1447, July 2014.

[50] P. Williams, B. Lansdorp, R. Ruiterkamp, and W. Ockels. Modeling, Simulation, and Testing of Surf Kites for Power generation. In *AIAA Modeling and Simulation Technologies Conference and Exhibit*, Honolulu, Hawaii, August 2008.

[51] P. Williams, B. Lansdorp, and W. Ockels. Optimal Cross-Wind Towing and Power Generation with Tethered Kites. *Journal of Guidance, Control, and Dynamics*, 31(1):81 – 93, 2008.

[52] J. H. Baayen. Automatic trajectory tracking control of kites. Master's thesis, 2011.

[53] C. Jehle. Automatic flight control of tethered kites for power generation. Master's thesis, Technische Universität München, 2012.

[54] Thomas Gehrmann. A Development of an open-source wind drone. Master's thesis, Rheinischen Friedrich-Wilhelms-Universitat, Bonn, November 2016.

[55] Philip Bechtle, Thomas Gehrmann, Christoph Sieg, and Udo Zillmann. AWEsome: An open-source test platform for airborne wind energy systems. *arXiv:1704.08695 [cs]*, April 2017. arXiv: 1704.08695.

[56] M. Kehs, C. Vermillion, and H. Fathy. Online Energy Maximization of an Airborne Wind Energy Turbine in Simulated Periodic Flight. *IEEE Transactions on Control Systems Technology*, PP(99):1–11, 2017.

[57] T. A. Wood, H. Hesse, A. Zgraggen, and R. Smith. Model-based flight path planning and tracking for tethered wings. In *IEEE Conference on Decision and Control*, pages 6712 – 6717, Osaka, Japan, December 2015.

[58] Michael Erhard and Hans Strauch. Flight control of tethered kites in autonomous pumping cycles for airborne wind energy. *Control Engineering Practice*, 40:13–26, July 2015. arXiv: 1409.3083.

[59] Haocheng Li, D. J. Olinger, and M. A. Demetriou. Attitude tracking control of an Airborne Wind Energy system. In *2015 European Control Conference (ECC)*, pages 1510–1515, July 2015.

[60] M. Jansson. Hydrodynamic analysis and simulation of a tidal energy converter. Master's thesis, Lund University, Sweden, 2013.

[61] Louise Kregting, Pal Schmitt, Ross Culloch, and Liliam Liber. Environmental monitoring baseline report (PDF Download Available). Technical Report D2.4, September 2016.

[62] Pál Schmitt, Ross Culloch, Lilian Lieber, Sverker Molander, Linus Hammar, and Louise Kregting. A tool for simulating collision probabilities of animals with marine renewable energy devices. *PLOS ONE*, 12(11):e0188780, November 2017. Publisher: Public Library of Science.

[63] Steven Benjamins, Violette Harnois, Helen Smith, Lars Johanning, Lucy Greenhill, Caroline Carter, and Ben Wilson. *Understanding the potential for marine megafauna entanglement risk from marine renewable energy developments.* January 2014.

[64] Clive J. Fox, Steven Benjamins, Elizabeth A. Masden, and Raeanne Miller. Challenges and opportunities in monitoring the impacts of tidal-stream energy devices on marine vertebrates. *Renewable and Sustainable Energy Reviews*, 81:1926–1938, January 2018.

[65] H. Li, D.J. Olinger, and M.A. Demetriou. Control of a tethered undersea kite energy system using a six degree of freedom model. In *CDC*, pages 688–693. IEEE, 2015.

[66] E Ahbe, T Wood, and R.S. Smith. Transverse Contraction-Based Stability Analysis for Periodic Trajectories of Controlled Power Kites with Model Uncertainty. In *Proceedings of the 57th IEEE Conference on Decision and Control*, Miami Beach, FL, USA, 2018. IEEE.

[67] Sean Costello, Grégory François, and Dominique Bonvin. Real-Time Optimization for Kites. *IFAC Proceedings Volumes*, 46(12):64–69, January 2013.

[68] Moritz Diehl, H. Georg Bock, Johannes P. Schlöder, Rolf Findeisen, Zoltan Nagy, and Frank Allgöwer. Real-time optimization and nonlinear model predictive control of processes governed by differential-algebraic equations. *Journal of Process Control*, 12(4):577–585, June 2002.

[69] Greg Horn, Sébastien Gros, and Moritz Diehl. Numerical Trajectory Optimization for Airborne Wind Energy Systems Described by High Fidelity Aircraft Models. In Uwe Ahrens, Moritz Diehl, and Roland Schmehl, editors, *Airborne Wind Energy*, Green Energy and Technology, pages 205–218. Springer Berlin Heidelberg, 2013.

[70] I. Argatov and R. Silvennoinen. Asymptotic modeling of unconstrained control of a tethered power kite moving along a given closed-loop spherical trajectory. *Journal of Engineering Mathematics*, 72(1):187–203, May 2011.

[71] S. Gros, M. Zanon, and M. Diehl. A relaxation strategy for the optimization of Airborne Wind Energy systems. In *European Control Conference (ECC)*, pages 1011 – 1016, Zurich, Switzerland, 2013.

[72] Sean Costello, Gregory Francois, and Dominique Bonvin. Crosswind Kite Control - A Benchmark Problem for Advanced Control and Dynamic Optimization. *European Journal of Control*, March 2017.

[73] Tarek N. Dief, Uwe Fechner, Roland Schmehl, Shigeo Yoshida, Amr M. M. Ismaiel, and Amr M. Halawa. System identification, fuzzy control and simulation of a kite power system with fixed tether length. *Wind Energy Science*, 3(1):275–291, May 2018.

[74] Michael Erhard, Greg Horn, and Moritz Diehl. A quaternion-based model for optimal control of the SkySails airborne wind energy system. *ZAMM - Journal of Applied Mathematics and Mechanics / Zeitschrift für Angewandte Mathematik und Mechanik*, 97(1):7–24, January 2017. arXiv: 1508.05494.

[75] M. De Lellis, R. Saraiva, and A. Trofino. Turning angle control of power kites for wind energy. In *52nd IEEE Conference on Decision and Control*, pages 3493–3498, December 2013.

[76] Haocheng Li, David J. Olinger, and Michael A. Demetriou. Modeling of Airborne Wind Energy Systems: Extended Apparent Attitude Tracking Approach. *Journal of Guidance, Control, and Dynamics*, 43(4):847–853, 2020. Publisher: American Institute of Aeronautics and Astronautics _eprint: https://doi.org/10.2514/1.G004366.

[77] H. Li, D. J. Olinger, and M. A. Demetriou. Passivity based control of a Tethered Undersea Kite energy system. In *2016 American Control Conference (ACC)*, pages 4984–4989, July 2016.

[78] L. T. Paiva and F. A. C. C. Fontes. Optimal control of underwater kite power systems. In *2017 International Conference in Energy and Sustainability in Small Developing Economies (ES2DE)*, pages 1–6, July 2017.

[79] Sebastian Rapp and Roland Schmehl. Enhancing Control System Resilience for Airborne Wind Energy Systems Through Upset Condition Avoidance. *arXiv:2004.02730 [cs, eess]*, April 2020. arXiv: 2004.02730.

[80] M. Erhard amd H. Strauch. Control of Towing Kites for Seagoing Vessels. *ArXiv e-prints*, February 2012.

[81] Tony A. Wood, Henrik Hesse, and Roy S. Smith. Predictive Control of Autonomous Kites in Tow Test Experiments. *IEEE Control Systems Letters*, 1(1):110–115, July 2017. arXiv: 1703.07025.

[82] B. Houska and M. Diehl. Optimal control for power generating kites. In *European Control Conference (ECC)*, pages 3560 – 3567, July 2007.

[83] F. Logist, M. Vallerio, B. Houska, M. Diehl, and J. Van Impe. Multi-objective optimal control of chemical processes using ACADO toolkit. *Computers & Chemical Engineering*, 37:191–199, February 2012.

[84] R. Quirynen, M. Vukov, M. Zanon, and M. Diehl. Autogenerating microsecond solvers for nonlinear MPC: A tutorial using ACADO integrators. *Optimal Control Applications and Methods*, 36(5):685–704, 2015. _eprint: https://onlinelibrary.wiley.com/doi/pdf/10.1002/oca.2152.

[85] B. Houska, H.J. Ferreau, and M. Diehl. ACADO toolkit-An opensource framework for automatic control and dynamic optimization. *Optimal Control Applications and Methods*, 32(5):298–312, 2011.

[86] K N Luttik, P S Anderson, L Johanning, and I M Viola. On the dynamics of the kite carousel. In *the 3rd International Conference on Renewable Energy Offshore*, page 9, Lisbon, Portugal, October 2018.

[87] Roland B. Stull. *Meteorology for Scientists and Engineers*. Brooks/Cole, 2000. Google-Books-ID: QrYRAQAAIAAJ.

[88] Marcelo De Lellis Costa de Oliveira. *Airborne Wind Energy with Tethered Wings: Modeling, Analysis and Control*. PhD Thesis, September 2016.

[89] Michael Erhard and Hans Strauch. Theory and Experimental Validation of a Simple Comprehensible Model of Tethered Kite Dynamics Used for Controller Design. In *Airborne Wind Energy*, Green Energy and Technology, pages 141–165. Springer, Berlin, Heidelberg, 2013.

[90] G. M. Dadd, D. A. Hudson, and R. A. Shenoi. Determination of kite forces using three-dimensional flight trajectories for ship propulsion. *Renewable Energy*, 36(10):2667 – 2678, 2011.

[91] Fernando Fontes and Luís Paiva. Optimization–based control of constrained nonlinear systems with continuous–time models: Adaptive time–grid refinement algorithms. volume 1776, page 090009, October 2016.

[92] Minesto. Power to change the future | Minesto, 2017. http://minesto.com.

[93] Pentland Firth Tidal Power Plant, Scotland. www.power-technology.com.

Appendix A

Publications

[1] K.N. Luttik, P.S. Anderson, L.Johanning, and I.M. Viola. On the dynamics of the kite carousel. In *the 3rd International Conference on Renewable Energy Offshore*, Page 9, Lisbon, Portugal, October 2018.

On the dynamics of the kite carousel

K.N. Luttik
Industrial Doctoral Centre for Offshore Renewable Energy, UK

P.S. Anderson
Scottish Association for Marine Science, Oban, UK

L. Johanning
University of Exeter, Exeter, UK

I.M. Viola
School of Engineering, University of Edinburgh, Edinburgh, UK

ABSTRACT: Kite based generators are being developed as the next iteration of offshore renewable energy converters. One such design is based on generating power using kites to induce movement in a vertical axis ground based generator, referred to as a kite carousel. This paper introduces a minimum-order model of such a kite and indicates the key scales and parameters that affect the performance of this kite-based generator. The model is validated using experimentally gained data. A physical model is used to determine the aerodynamic coefficients of a high performance kite. The resulting numerical model shows a potential power delivery of 360 W, with substantial room for improving yield.

1 INTRODUCTION

Developments in renewable energy shows the importance of pushing the boundaries to find new ways of extracting energy in various locations. In the past decade strides have been made towards developing kite based generation systems as an economic alternative to conventional wind turbines (Khan & Rehan 2016).

Such systems can be divided into one of two designs. A distinction is made according to the placement of the generator. Generation will take place either at the kite, or at ground level. The first design sees the kite acting as a platform for one or multiple turbines. The kite is flown through the airspace allowing the turbines to generate electricity, which is send down to the surface through a power cable incorporated in the tether.

An alternative design has the generator located at ground level. The kite movement is transferred through the tether to induce motion in the generator. A commonly investigated method used is the pumping kite model, where a kite is used to reel out a tether. This tether real out causes a ground based generator to rotate and generate power. Once the kite is fully reeled out, the kite is retrieved by reducing the pull on the kite and reeling in the tether. This cycle is designed such that there is a net power gain.

Both these designs have been researched extensively and progressed towards early stage commercial development. Much of this research is summarized by Cherubini *et al*. (2015). A substantial amount of research has focused on accurately modelling kite behavior (Argatov *et al.* 2011, Bosch *et al.* 2014, Fechner *et al.* 2014, van der Vlugt *et al.* 2017, Pastor-Rodríguez, *et al.* 2017, Losantos & Sánchez-Arriaga 2015, Cadalen *et al.* 2017, Geschiere 2014). First as proof of concept and subsequently as a basis for the development of kite control strategies. Models range from low-order point mass models (Dadd, *et al.* 2010) to computationally intensive high-order finite element models (Bosch *et al*. 2014).

Thus far, the bulk of research and development has focused on single kite systems. Although, multi-kite systems have been mentioned and studied as a potential way to further increase power output (Cherubini 2017). However, issues with control and lack of firm, validated kite models, have thus far limited the development of many such concepts to full physical models.

This paper describes a low order dynamic model of a kite which would generate power through a carousel type setup. This setup involves a vertical axis generator where the generating motion comes from one or more kites flying along a flight path that induces motion in the generator. Such a concept was first mentioned by Williams, *et al.* (2007), and Fagiano (2009). Followed by a concept for a large scale carousel by KiteGen (Ippolito 2009, Canale *et al.* 2009).

While both Williams *et al.* and Fagiano investigate carousel designs with high tether length to generator diameter ratios, the resulting control strategies result in substantially different flightpaths. Williams *et al.* seek an optimum flightpath to match generator rotation leading to quick crosswind loops. Fagiano on the other hand simulates the carousel as a number of vehicles moving along a rail, with power take off hap-

pening through the rotation of the wheels while moving downwind. Moving upwind, the vehicles are powered through the rail to pull the kite upwind. As such, two distinct kite behaviours are modelled, with transition phases between them. This results in quick crosswind loops while the kite is moving downwind, and the kite being sent to a stationary zenith position while it is being pulled upwind. Fagiano further includes tether dynamics, where these are excluded from the Williams model. Both models allow for a variable tether length, allowing the models to work as either a pure pumping generator, a pure carousel or a combination of the two. As such both models are computationally intensive.

This paper describes the work that lead to the highly reduced model that was developed to be faster than real time and functions as a first step towards a generic carousel model which can be further developed to demonstrate the feasibility of carousel based generation for tidal applications. To reduce computation time and resources the model was reduced to model only the carousel model. Keeping the tether length at a constant reduced length minimizes the degrees of freedom and consequently keeps the model complexity low. The model is described in section 2. The experimental kite setup used to validate this numerical model is described in section 3. The resulting tuning and validation of the numerical model are shown and discussed in section 4, which are discussed in section 5. Finally, conclusions are drawn in section 6 and, ongoing work and future model progression is highlighted in Section 7.

2 NUMERICAL MODEL

2.1 *Frames of reference*

The axes system used is illustrated in Figure 1, which shows a neutral kite position where $\vec{z}_k$ is in line with the tether pointing-vector. This definition of axes is important as with each iteration through time the kite axes position and orientation are updated to represent the kite attitude at the following time step. Kite design allows for manipulation of the power setting, by adjusting the built in angle of attack through manipulation of the kite control lines. In the numerical model this is represented as a rotation around the kite pitch axis $\vec{y}_k$. The base reference is defined by the X-axis ($\vec{x}_k$) pointing directly upwind. The tether vector is indicated by $\vec{x}_T$.

2.2 *Model assumptions*

In order to speed up modelling times, assumptions were made. The assumptions concerning wind profile, kite control, and tether modelling are described in more detail in the following sections. The model

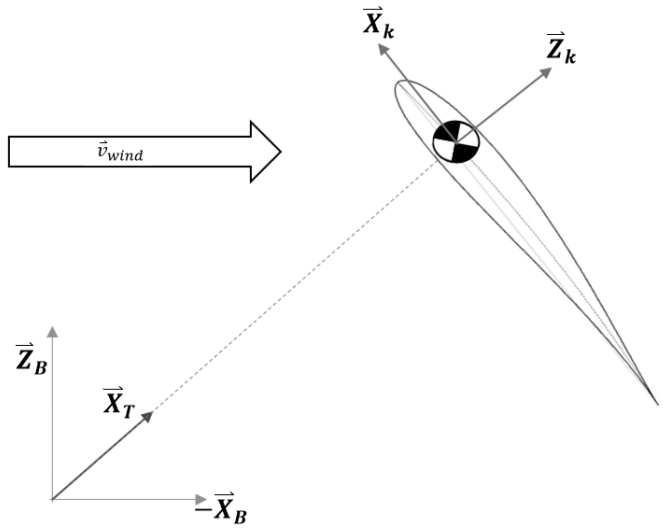

Figure 1: Reference frames used for model.

introduced in this paper was designed in such a way that it represents a generic carousel model. For validation purposes the model simulates kite behaviour in air, such that it can be compared to the results of physical kite tests. The kite is modelled as a point mass with a specific aerodynamic profile. Kite control is modelled pitching and rolling the kite to adjust the aerodynamic coefficients and force profiles as described in sections 2.2.2 and 2.2.3.

2.2.1 *Wind profile*

Initially an ideal wind profile was considered of a constant uniform wind. To more accurately represent the increase of velocity with height, a log profile is applied as proposed by Stull (2000). The log profile used is shown in equation 1, where the wind velocity ($\vec{v}_{w,k}$) is computed at kite level (h_k) using the wind measured at ground level ($\vec{v}_{w,g}$ at h_g), and the roughness length (z_0= 0.005) for smooth landscape.

$$\vec{v}_{w,k} = \vec{v}_{w,g} \frac{\ln\left(\frac{h_k}{h_0}\right)}{\ln\left(\frac{h_g}{h_0}\right)} \quad (1)$$

2.2.2 *Power control*

Kite power control is defined as the manipulation of the built in kite angle of attack (α_0) This is done by either adjusting the length of the rear control lines, attached to the trailing edge of the kite, with respect to

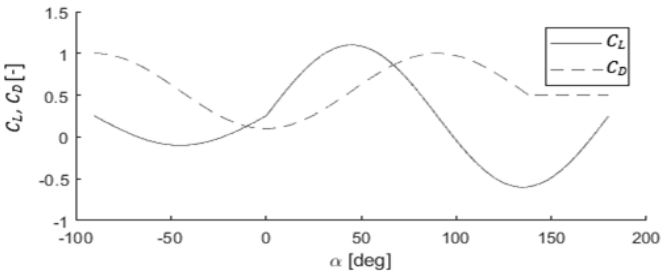

Figure 2: Aerodynamic coefficients used for initial estimation (Fechner 2016, Spera 2008)

the main power line, attached at the leading edge of the kite. Lengthening the control lines simultaneously reduces α_0, and consequently the overall angle of attack α, as per equation 2. The reverse is true for shortening the control lines.

The force felt through the main power line is adjusted due to the effect of the altered angle of attack on the lift and drag coefficients, (C_L and C_D), on overall aerodynamic forces. This effect is further explained in Section 2.3.

The initial aerodynamic coefficients are estimated from literature (Fechner 2016, Spera 2008) and their variation with respect to α is shown in Figure 2 . These graphs will be tailored to the values deduced from the experimental model. The graphs are used to interpret the initial acceptable working range of α to be $-10\,° \leq \alpha \leq 20\,°$. The angle of attack α is computed as

$$\alpha = \alpha_0 + \alpha_w, \tag{2}$$

where

$$\alpha_0 = \sin^{-1}\left(\vec{X}_T \cdot \vec{X}_k\right), \tag{3}$$

$$\alpha_w = \sin^{-1}\left(\frac{\vec{v}_{app} \cdot \vec{X}_T}{\left|\vec{v}_{app}\right|}\right), \tag{4}$$

and α_w is the angle between the apparent wind vector and the vector perpendicular to the tether from which α_0 is measured. In this case it is important to take the component of the apparent wind speed ($\vec{v}_{app}$) in line with the kite pointing vector ($\vec{X}_k$). The apparent wind speed is computed through $\vec{v}_{app} = \vec{v}_{w,k} - \vec{v}_k$.

2.2.3 *Turning control*

Turning dynamics of a flexible kite have been modelled and approximated extensively, (Fechner et al. 2014, Bosch et al. 2014). Typically a turn rate law is used to represent kite turning in numerical models (Erhard & Strauch 2013).

A pseudo control has been implemented in the numerical model similar to that proposed by Williams et al. (2007), and Paiva & Fontes (2018), where the roll angle is controlled to adjust the orientation of the aerodynamic forces acting at the kite point mass. Attitude dynamics are similarly ignored. To this end it is assumed that the kite auto-corrects to align $\vec{X}_k$ with the apparent incoming wind velocity. The yaw turn rate is limited to allow for side slip at low kite velocities, such as is experienced at the edges of the wind window.

2.2.4 *Tether contributions*

It is presumed that due to the short tether length used for the numerical model of less than 500 m. The tether behaves as a straight, rigid rod connecting the kite to the ground station. The mass of the tether is included in the point mass of the kite. At this point the tether drag contribution is assumed to be negligible.

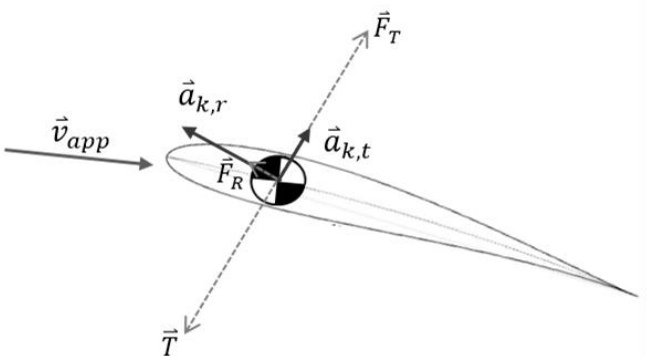

Figure 3: Kite accelerations

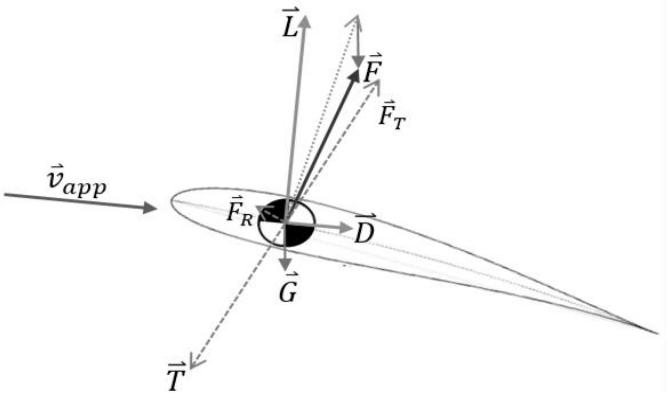

Figure 4: Kite load case

When the tether length is increased the drag effects are taken into account by adding a quarter of the tether drag area to the kite drag area in the overall drag computation, as shown in Argatov et al. (2011).

2.3 *Load case*

The load case considered here includes both aerodynamic and gravity forces. These forces are depicted in Figure 4. The resultant force is defined by equation

$$\vec{F} = \vec{L} + \vec{D} + \vec{G} \tag{5}$$

Where the corresponding lift ($\vec{L}$), and drag ($\vec{D}$) forces are computed as

$$\vec{L} = \frac{1}{2}\rho A C_L \left|\vec{Y}_k \times \left(\vec{v}_{app} \times \vec{Y}_k\right)\right|^2 \cdot \frac{\vec{Y}_k \times \vec{v}_{app}}{\left|\vec{Y}_k \times \vec{v}_{app}\right|}, \tag{6}$$

and

$$\vec{D} = \frac{1}{2}\rho A C_D \left|\vec{v}_{app}\right| \vec{v}_{app}\,. \tag{7}$$

with air density (ρ) and kite area (A). The axis $\vec{Y}_k$ represents the Y-axis of the kite reference system as indicated in Figure 1. Finally gravity ($\vec{G}$) is calculated through

$$\vec{G} = (m_k + m_t)\vec{g} \tag{8}$$

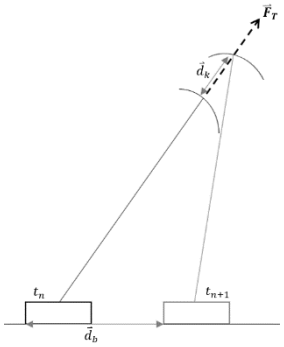

Figure 5: Kite motion due to carousel

Where m_k, and m_t, represent the kite and tether mass respectively, and $\vec{g}$ indicates gravitational acceleration.

This resultant force is divided into two components, tangential ($\vec{F}_T$) and perpendicular ($\vec{F}_R$) to the kite tether, which are determined as follows

$$\vec{F}_T = \left(\vec{F} \cdot \vec{X}_T\right)\vec{X}_T \tag{9}$$

$$\vec{F}_R = \vec{X}_T \times \left(\vec{F} \times \vec{X}_T\right) \tag{10}$$

Due to the tether length remaining constant the kite acceleration perpendicular to the tether ($\vec{a}_{k,t}$) is set to zero as illustrated in Figure 3. As such, $\vec{T} = -\vec{L}_T$. Finally, the kite angular kite acceleration ($\vec{a}_{k,r}$) is computed through equation 11.

$$\vec{a}_{k,r} = \frac{\vec{F}_R}{(m_k + m_t)l_T} \tag{11}$$

2.4 *Carousel motion*

For initial analysis, the carousel is modelled to rotate at a set angular velocity. The additional displacement of the kite due to this movement of the tether base is assumed to be in the direction of $\vec{F}_T$, as shown in Figure 5. It is subsequently assumed that the velocity of the tether base is substantially smaller than that of the kite and thus will have a negligible effect on the kite forces within a single time step iteration. Thus, this displacement solely affects the tether tension ($\vec{T}$) as per the following:

$$\vec{T} = \vec{F}_T - \vec{F}_{T,car}\,, \tag{12}$$

where:

$$\vec{F}_{T,car} = (m_k + m_t)\frac{\vec{d}_k}{dt^2} \tag{13}$$

In equation 13, the kite movement ($\vec{d}_k$) is derived from the carousel movement of the tether base $\vec{d}_b$, the tether vector along $\vec{X}_T$, and the assumption that the tether length remains constant.

The timestep used is set suitably small to prevent significant errors from building up. The carousel effect on the kite displacement is added to the displacement due to the radial acceleration computed using equation 11.

The power take off (P) is subsequently computed using the 'effective' horizontal component of the tether tension in the direction of travel of the base of the tether ($\vec{F}_p$). An efficiency factor (η) is included to account for losses in the system

$$\vec{F}_P = \left(\vec{F}_T \cdot \vec{v}_T\right)\frac{\vec{v}_T}{|\vec{v}_T|^2} \tag{14}$$

$$P = \left|\vec{v}_T \vec{F}_P\right|\eta \tag{15}$$

3 EXPERIMENTAL MODEL

3.1 *Setup*

The physical kite model incorporates a 10 m^2 Flysurfer Psycho kite, with a 21 m tether attaching to the kite bridle. This kite is fitted out with a Pixhawk unit including GPS and pitot tube. The Pixhawk is outfitted with accelerometers, gyrometers, a barometer, an external pitot tube, and a GPS transmitter. The measured values are fed through a Kalmann filter and stored. As such the kite position, rotations, and accelerations are recorded. The pitot tube provides the pressure difference at the leading edge of the kite, which is used to derive the kite apparent velocity. The tether base is fixed to a stationary strongpoint through a load cell. The output from the loadcell is amplified and subsequently logged using an M0 Feather Adafruit Adalogger.

The kite is controlled manually through the kite control bar. This input is recorded through a chest mounted GoPro, the position of the control bar is used

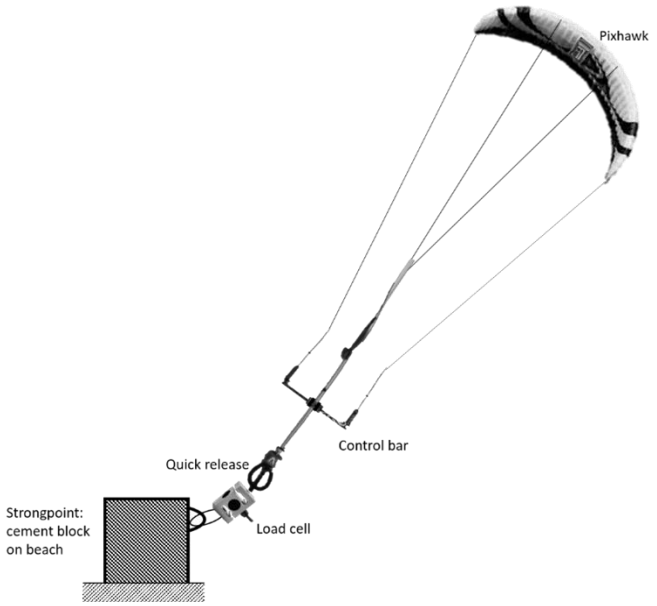

Figure 6: Visual representation of kite setup (not to scale)

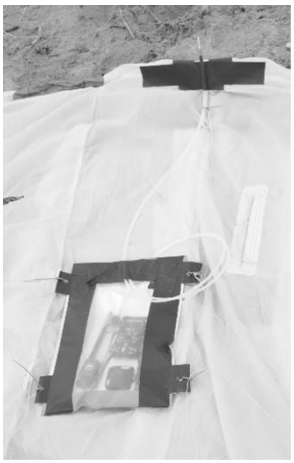

Figure 8: Pixhawk and pitot tube mounted in kite bridle

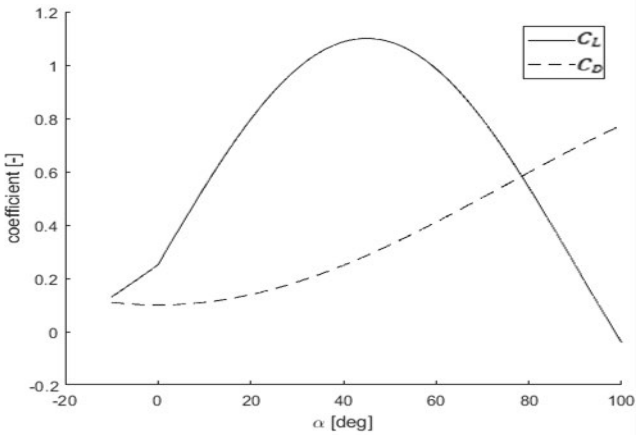

Figure 7: Lift and drag coefficient approximations

to deduce he approximate percentage of the maximum control limit input is applied. Turning control is further discussed in section 3.3.

The setup depicted in Figure 6, illustrates the various elements of the physical testing setup, with Figure 8 showing the mounting of the Pixhawk unit with the pitot tube at the leading edge of the kite.

3.2 *Aerodynamic coefficients*

Figure 2 shows an approximation of how aerodynamic coefficients vary with α. An additional variable often used to relate lift and drag coefficients is the glide ratio: $\gamma = C_L/C_D$. This glide ratio effectively shows the ratio between lift and drag forces across the kite. Due to the assumption of a straight tether, this angle can be deduced from the tether elevation angle (θ_T) found when the kite is at a stationary point down wind, as shown in equation 16(Alexander & Stevenson 2001)

$$\theta_T = \tan^{-1}\left(\frac{L-G}{D}\right) \tag{16}$$

The aerodynamic coefficients are derived using equations 16, and 6 to 8.

3.3 *Turning control*

Turning control is simulated in the numerical model through imposing a roll angle on the kite represented by a point mass. The roll angle is determined with respect to the tether, such that a neutral angle has $\vec{Y}_k$ directly perpendicular to $\vec{X}_T$. This angle is dictated as a percentage of a maximum allowable turn angle.

To determine a realistic scale, the kite is flown in figure 8s. The maximum allowable values are concluded from the measured kite position and attitude combined with the recorded control input throughout the manoeuvre. Subsequently the kite is flown in loops as a secondary measurement.

3.4 *Power control*

The control of kite pull through manipulation of α_0 is modelled from the manual control input through the kite control bar. As in Cadalen *et al.* (2017), this translation from physical control to adjusted α_0 is done as follows:

$$\alpha_0 = K\epsilon + \epsilon_0 \tag{17}$$

Where, ε shows the control input and offset (ε_0), with additional scaling coefficient (K). These coefficients are deduced from the kite response to control variations starting with kite at zenith at the lowest power setting. The control bar is subsequently pulled in to increase α_0. The corresponding location of the kite in the wind window is used to determine the range of α_0 in the Flysurfer kite.

4 RESULTS

In this section the preliminary findings from the initial flight tests are discussed. The results are compared with the findings of the numerical study and deviations between the models are addressed. The resulting carousel model output is also shown and discussed.

4.1 *Aerodynamic coefficients*

Positioning the kite at zenith showed an angle of attach of 10º. This corresponds to a tether elevation angle of 80º, and through equation 16 an glide ratio of 5.7. This lead to the original lift drag coefficients being adjusted to the fit shown in Figure 7. These altered curves fit with the lift and drag coordinates presented by De Lellis Costa de Oliveira (2016).

The gyrometer measurements show a general yaw rate of up to 3 deg/s when flying in a smooth figure 8 pattern. However, when initiating a steep dive from

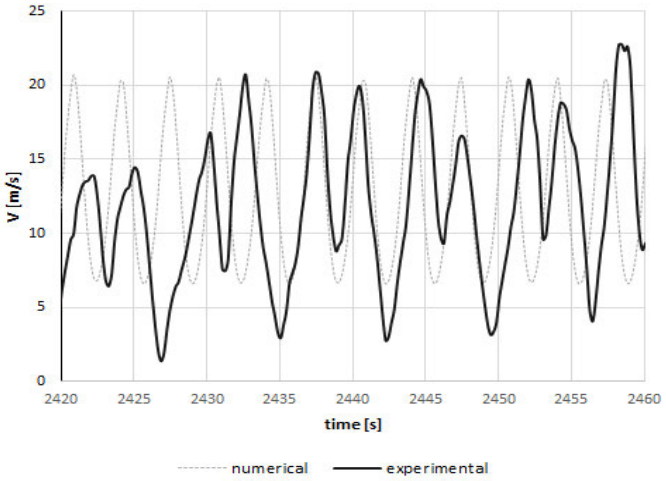

Figure 10: Kite velocity comparison

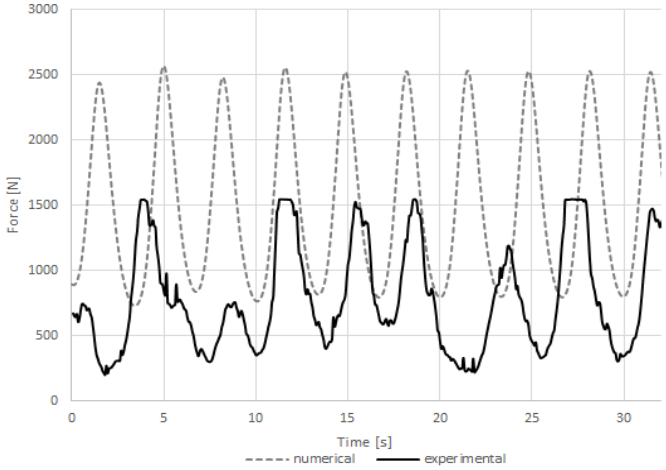

Figure 9: Tether tension comparison

zenith this rate increased up to 10 deg/s. The yaw limits imposed on the numerical model reflect these limits.

4.2 *Kite velocities*

The kite velocity was recorded by both the GPS unit and can be derived from the data recorded by the accelerometers within the Pixhawk. The resulting kite velocity during a number of figure 8 manoeuvres was compared to the output of the numerical model. This comparison is shown in Figure 10.

While the top velocities reach match up well it is at the lower end where the results vary more substantially. As the kite approaches the end of the wind window it decelerates due to the change in kite orientation, leading to the kite velocity being practically opposite to the wind speed. In the numerical model the kite turn is initiated before this effect is seen. An automated control system would be able to fine tune the timing of these manoeuvres.

4.3 *Tether tension*

The tension in the main power line was measured throughout the kite test. The results were compared to those gained from the numerical model and are depicted in Figure 9. As with the velocities the numerical model shows a higher predicted load. This is primarily due to the higher velocities computed as discussed in the previous section. However, a minor portion of the discrepancy is due to the fact that only the load along the main power line is considered, as the load used to steer the kite through the steering lines was not measured during the flight.

Additionally, it was found that the line loading appears to top out at around 1.5 kN. The kite used during this test is a highly developed design, using the deformability of the wing to produce a consistent pulling force required for kite surfing. As such there are safety features to prevent over powering of the kite during such high loading manoeuvres, a feature that is not incorporated in the numerical model.

4.4 *Carousel effects*

Using the adjusted aerodynamic coefficients discussed in section 4.1, the kite carousel model was run to show a initial estimation of generation potential. The results shown in Figure 11 assume a single airborne kite with a 30 m tether. The carousel modelled has a radius of 3 m. and rotates at 3.5 rpm. A constant wind speed of 6 m/s is assumed. Because only one kite is modelled, the power generated dips into negative values where the kite needs to be dragged upwind.

The power production is highly dependent on the kite flight path. In this case a basic control is used to fly the kite in high power figure 8's while generating, and send it to a low power holding position at zenith during the non-generating part of the carousel cycle. While this rudimentary control strategy causes the high power spikes seen while transitioning between the powered and non-powered sections of the carousel cycle, it does show a net power production of

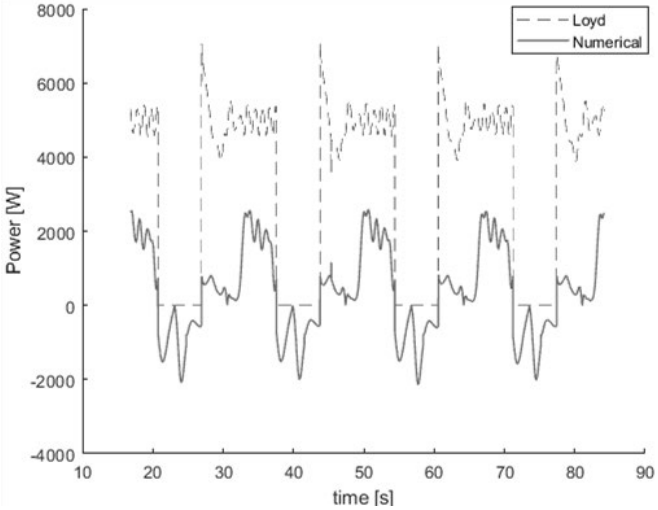

Figure 11: Numerical estimate of power generated by carousel versus Loyd maximum available crosswind power.

360W. Optimizing the carousel design and specifically the kite trajectory leaves room to greatly improve this output.

5 DISCUSSION

The initial numerical results were checked against the theoretical limit of crosswind kite power generation, deduced by (Diehl 2013), from earlier work by Loyd (1980). The equation shown below shows the maximum assumed perfect crosswind flight with an extending tether causing rotation in a ground based generator, at an optimum reel out velocity equal to $\vec{v}_w/3$.

$$P_{Loyd} = \frac{1}{2}\rho V_w^3 A \frac{4}{27} C_L \left(\frac{C_L}{C_D}\right)^2 \quad (18)$$

Computing the potential power using the Loyd equation shows a maximum generation of 3 kW, as shown in Figure 11. In this case this does not take into account the power required to pull the kite upwind, as shown in Figure 11, at this point in time the Loyd power is set to zero. This check shows that in it's current configuration the kite carousel power generation falls substantially beneath the theoretical power limit of crosswind power. Which allows for substantial system improvements due to further optimization of the flightpath and transition between powered and depowered portion of the generator cycle.

A substantial amount of optimization is possible in the transition phases where the kite transitions from high powered generation mode, to low powered glide mode. Figure 11 shows the first half of the cycled power still sees the kite transferring slowly into a higher powered flightpath. Improving this may require a deviation from the current flightpath of low and high figure 8's to a pattern more tailored to the carousel movement.

With kite power not having reached commercial stages of production, there is limited possibility to compare with similar cases. At the current power estimation this would compare the output of a 3 m wind turbine in 6 m/s winds with an aerodynamic efficiency of 0.4 (Burton et al. 2011).

Further flightpath optimization would lead to a more efficient transition phase, pushing up the net power generation up towards the 2kW. This can be compared to a 3.5 m wind turbine.

6 CONCLUSIONS

A minimum order numerical kite model has been introduced, which models a kite generator in a carousel configuration. The kite dynamics have been compared to data gained through experimental testing using a high performance ram air sports power kite.

Subsequently, model parameters including the lift and drag coefficient curves have been adjusted to reflect the practical behaviours of the kite. Although some distinct differences are noted in kite velocity and tether tension between models, this is attributed to the lack of sophisticated kite control in the experimental testing.

Using the updated model to evaluate potential power production of the carousel design showed a net power production of 360W. This can be greatly improved by further optimizing the kite flight path to initiate a more effective transition between when the kite is rotating the generator and when it is being pulled up wind by the generator.

7 FUTURE WORK

Following on from this work the carousel model will be subjected to submerged conditions. This includes accounting for added mass and replacing the wind model with a tidal flow.

To deal with this varying flow the control scheme must be adapted to vary flightpath options for optimum generation. Finally the carousel will be expanded to include multiple kites working in unison to smooth generation. All of this will lead to a full model that will determine the feasibility of the submerged carousel design.

8 ACKNOWLEDGMENTS

The authors would like to thank the Energy Technology Institute and the Research Council Energy Programme for funding this research as part of the IDCORE programme (grant EP/J500847), and the Scottish Association for Marine Science for providing technical assistance and equipment.

REFERENCES

Alexander, K, and J Stevenson. 2001. "A Test Rig for Kite Performance Measurement." Proceedings of the Institution of Mechanical Engineers, Part B: Journal of Engineering Manufacture 215 (4): 595–98. https://doi.org/10.1243/0954405011518412.

Argatov, I., P. Rautakorpi, and R. Silvennionen. 2011. "Apparent Wind Load Effects on the Tether of a Kite Power Generator." Journal of Wind Engineering and Industrial Aerodynamics 99 (10): 1079–88. http://dx.doi.org/10.1016/j.jweia.2011.07.010.

Bosch, Allert, Roland Schmehl, Paolo Tiso, and Daniel Rixen. 2014. "Dynamic Nonlinear Aeroelastic Model of a Kite for Power Generation." Journal of Guidance, Control, and Dynamics 37 (5): 1426–36. https://doi.org/10.2514/1.G000545.

Cadalen, B., P. Lanusse, J. Sabatier, F. Griffon, and Y. Parlier. 2017. "Modeling and Control of a Tethered Kite in Dynamic Flight." In Innov'Sail 2017. Lorient, France. https://hal.archives-ouvertes.fr/hal-01707611.

Canale, M., L. Fagiano, and M. Milanese. 2009. “KiteGen: A Revolution in Wind Energy Generation.” Energy, WESC 2006Advances in Energy Studies6th World Energy System Conference5th workshop on Advances, Innovation and Visions in Energy and Energy-related Environmental and Socio-Economic Issues, 34 (3): 355–61. https://doi.org/10.1016/j.energy.2008.10.003.

Cherubini, A., A. Papini, R. Vertechy, and M. Fontana. 2015. “Airborne Wind Energy Systems: A Review of the Technologies.” Renewable and Sustainable Energy Reviews 51: 1461–76. http://dx.doi.org/10.1016/j rser.2015.07.053.

Cherubini, Antonello. 2017. “Advances in Airborne Wind Energy and Wind Drones.” PhD Thesis, Sant’Anna University of Pisa. https://www. areasciencepark. it/wp-content/uploads/PHD_THESIS-Cherubini. pdf.

Dadd, G. M., D. A. Hudson, and R. A. Shenoi. 2010. “Comparison of Two Kite Force Models with Experiment.” Journal of Aircraft 47 (1): 212–24. https://doi.org/10.2514/1.44738.

De Lellis Costa de Oliveira, Marcelo. 2016. “Airborne Wind Energy with Tethered Wings: Modeling, Analysis and Control.” PhD Thesis. https://doi.org/10.13140/RG.2.2.12207.74409.

Diehl, Moritz. 2013. “Airborne Wind Energy: Basic Concepts and Physical Foundations.” In Airborne Wind Energy, edited by Uwe Ahrens, Moritz Diehl, and Roland Schmehl, 3–22. Berlin, Heidelberg: Springer Berlin Heidelberg. https://doi.org/10.1007/978-3-642-39965-7_1.

Erhard, Michael, and Hans Strauch. 2013. “Theory and Experimental Validation of a Simple Comprehensible Model of Tethered Kite Dynamics Used for Controller Design.” In Airborne Wind Energy, 141–65. Green Energy and Technology. Springer, Berlin, Heidelberg. https://doi.org/10.1007/978-3-642-39965-7_8.

Fagiano, L. 2009. “Control of Tethered Airfoils for High-Altitude Wind Energy Generation.” PhD Thesis, Politecnico di Torino.

Fechner, U. 2016. “A Methodology for the Design of Kite-Power Control Systems.” https://doi.org/10.4233/uuid:85efaf4c-9dce-4111-bc91-7171b9da4b77.

Fechner, Uwe, Rolf van der Vlugt, Edwin Schreuder, and Roland Schmehl. 2014. “Dynamic Model of a Pumping Kite Power System.” *ArXiv:1406.6218 [Cs]*, June. http://arxiv.org/abs/1406.6218.

Geschiere, Nick H. 2014. “Dynamic Modelling of a Flexible Kite for Power Generation.” MSc Thesis, TU Delft. http://www.lr.tudelft.nl/fileadmin/Faculteit/LR/Organisatie/Afdelingen_en_Leerstoelen/Afdeling_AEWE/Wind_Energy/Education/Masters_Projects/Finished_Master_projects/doc/Nick_Geschiere_r.PDF.

Ippolito, Massimo. 2009. “KiteGen Research » KiteGen Carousel.” April 9, 2009. http://www.kitegen.com/en/products/kite-gen-carousel/.

Khan, Zeashan, and Muhammad Rehan. 2016. “Harnessing Airborne Wind Energy: Prospects and Challenges.” *Journal of Control, Automation and Electrical Systems* 27 (6): 728–40. https://doi.org/10.1007/s40313-016-0258-y.

Losantos, L. Salord, and G. Sánchez-Arriaga. 2015. “Flight Dynamics and Stability of Kites in Steady and Unsteady Wind Conditions.” *Journal of Aircraft* 52 (2): 660–66. https://doi.org/10.2514/1.C032825.

Loyd, M. L. 1980. “Crosswind Kite Power.” *Journal of Energy* 4 (3): 106–11. https://doi.org/10.2514/3.48021.

Paiva, Luís, and Fernando A. C. C. Fontes. 2018. “Optimal Control Algorithms with Adaptive Time-Mesh Refinement for Kite Power Systems.” *Energies* 11 (February): 475. https://doi.org/10.3390/en11030475.

Pastor-Rodríguez, A., G. Sánchez-Arriaga, and M. Sanjurjo-Rivo. 2017. “Modeling and Stability Analysis of Tethered Kites at High Altitudes.” *Journal of Guidance, Control, and Dynamics* 40 (8): 1892–1901. https://doi.org/10.2514/1.G002550.

Spera, D. A. 2008. “Models of Lift and Drag Coefficients of Stalled and Unstalled Airfoils in Wind Turbines and Wind Tunnels.” NASA nasa/cr-2008-215434. https://ntrs.nasa.gov/archive/nasa/casi.ntrs nasa.gov/20090001311.pdf.

Stull, Roland B. 2000. Meteorology for Scientists and Engineers. Brooks/Cole.

Vlugt, R. van der, A. Bley, M. Noom, and R. Schmehl. 2017. “Quasi-Steady Model of a Pumping Kite Power System.” ArXiv:1705.04133 [Cs, Math], May. http://arxiv.org/abs/1705.04133.

Williams, P., B. Lansdorp, and W. Ockels. 2007. “Optimal Trajectories for Tethered Kite Mounted on Vertical Axis Generator.” In AIAA Modeling and Simulation Technologies Conference and Exhibit. Hilton Head, South Carolina. http://dx.doi.org/10.2514/6.2007-6706.

Appendix B

Optimization Results

Table B.1: Parameter study results

$C1$ $[r_c/L_t]$	$C2$ $[v_b/v_f]$	A_k [m^2]	ρ [kg/m^3]	v_f [m/s]	L_t [m]	r_c [m]	T [s]	P [kW]	s_k [m]	$P1$ $\left[\frac{P}{\rho {v_f}^3 {r_c}^2}\right] 10^6$	$P2$ $\left[\frac{P}{\rho {v_f}^3 {s_k}^2}\right] 10^9$	$s_k/(2\pi r)$	*comments*
0.01	0.25	25	1.225	15	1000	10	17	20	530	0.0	0.0	8.44	*Williams et.al.*
0.017	0.14	10	1025	2	60	1	22	448	78.4	54.6	8.9	12.48	*loops(1)*
0.017	0.26	10	1025	2	60	1	12	241.1	38	29.4	20.4	6.05	*loops(1)*
0.017	0.32	10	1025	2	60	1	10	171	31.8	20.9	20.6	5.06	*fig 8*
0.017	0.43	10	1025	2	60	1	7.5	85	18.7	10.4	29.6	2.98	*fig 8*
0.017	0.52	10	1025	1	60	1	12.08	12.8	10.6	12.5	111.1	1.69	*fig 8*
0.017	0.52	10	1025	1	60	1	12.08	22	13.6	21.5	116.0	2.16	*fig 8*
0.017	0.52	10	1025	2	60	1	6	-6	7.2	-0.7	-14.1	1.15	*small loop*
0.017	0.71	10	1025	1	60	1	8.85	8.3	26.5	8.1	11.5	4.22	*loop*
0.017	0.79	10	1025	1	60	1	7.95	3.8	6.7	3.7	82.6	1.07	*small loop*
0.017	0.71	10	1025	2	60	1	4.5	-3	6.6	-0.4	-8.4	1.05	*small loop*
0.017	0.79	10	1025	2	60	1	4	-9	6.2	-1.1	-28.6	0.99	*small loop*
0.017	0.14	10	1025	2	30	0.6	13.5	247.4	62.8	83.8	7.7	16.66	*L*
0.02	0.14	10	1025	2	30	0.6	13.5	262.6	62	89.0	8.3	16.45	*L*
0.02	0.26	10	1025	2	60	1.2	14.5	338.1	53	28.6	14.7	7.03	*fig 8*
0.02	0.32	10	1025	2	60	1.22	12	238	34.1	19.5	25.0	4.45	*loops(1)*
0.02	0.43	10	1025	2	60	1.2	8.8	118.9	21.1	10.1	32.6	2.80	*fig 8*
0.02	0.52	10	1025	2	60	1.2	7.2	63.6	15.9	5.4	30.7	2.11	*fig 8*
0.02	0.71	10	1025	2	60	1.2	5.3	1.9	8	0.2	3.6	1.06	*small loop*
0.02	0.79	10	1025	2	60	1.2	4.8	-11.7	7.4	-1.0	-26.1	0.98	*small loop*
0.033	0.14	10	1025	2	30	1	22	674	99.5	82.2	8.3	15.84	*weird long(L)*
0.033	0.26	10	1025	2	30	1	12	639	55.2	77.9	25.6	8.79	*loop*
0.033	0.14	10	1025	2	30	1	22	643.9	99.7	78.5	7.9	15.87	*loops*
0.033	0.26	10	1025	2	30	1	12	268.7	48.4	32.8	14.0	7.70	*loop(1)*

Continued on next page

Table B.1 – *Continued from previous page*

$C1$ $[r_c/L_t]$	$C2$ $[v_b/v_f]$	A_k [m^2]	ρ [kg/m^3]	v_f [m/s]	L_t [m]	r_c [m]	T [s]	P [kW]	s_k [m]	$P1$ $\left[\frac{P}{\rho {v_f}^3 {r_c}^2}\right] 10^6$	$P2$ $\left[\frac{P}{\rho {v_f}^3 {s_k}^2}\right] 10^9$	$s_k/(2\pi r)$	*comments*
0.033	0.32	10	1025	2	60	2	19.6	351.7	38.8	10.7	28.5	3.09	*thin 8*
0.033	0.43	10	1025	2	60	2	14.6	319.9	37.9	9.8	27.2	3.02	*loops(1)*
0.033	0.52	10	1025	2	60	2	12	185.4	26.7	5.7	31.7	2.12	*fig 8*
0.033	0.71	10	1025	2	60	2	8.9	59.5	18.5	1.8	21.2	1.47	*fig 8*
0.033	0.79	10	1025	2	60	2	8	27.8	15.7	0.8	13.8	1.25	*fig 8*
0.05	0.26	10	1025	2	30	1.5	18	408.9	53.4	22.2	17.5	5.67	*loops(wide)*
0.05	0.32	10	1025	2	30	1.5	14.5	618	68.4	33.5	16.1	7.26	*loops*
0.05	0.26	10	1025	2	30	1.5	18	229.9	41.9	12.5	16.0	4.45	*loop*
0.05	0.32	10	1025	2	30	1.5	14.5	205.9	43.3	11.2	13.4	4.59	*loops(1)*
0.05	0.43	10	1025	2	60	3	22	413	51.5	5.6	19.0	2.73	*loops(1)*
0.05	0.52	10	1025	2	60	3	18	360.4	39	4.9	28.9	2.07	*fig 8*
0.05	0.71	10	1025	2	60	3	13.3	139	29.4	1.9	19.6	1.56	*fig 8*
0.05	0.79	10	1025	2	60	3	12	70.9	24.9	1.0	13.9	1.32	*smooth loop*
0.067	0.26	10	1.225	8	60	4	12.08	98.7	253	9.8	2.5	10.07	*L*
0.067	0.26	10	1025	4	30	2	12	3783.6	101	14.4	5.7	8.04	*smooth w 8s*
0.067	0.32	10	1025	2	30	2	19.7	968.8	86.9	29.5	15.6	6.92	*loops*
0.067	0.43	10	1025	2	30	2	14.6	704.1	61.2	21.5	22.9	4.87	*loops(1)*
0.067	0.52	10	1025	2	30	2	12	474.5	48.3	14.5	24.8	3.84	*smooth loop*
0.067	0.26	10	1025	2	30	2	24	586.6	91.7	17.9	8.5	7.30	*skinny 8*
0.067	0.32	10	1025	2	30	2	19.7	398	50.2	12.1	19.3	3.99	*smooth*
0.067	0.43	10	1025	2	30	2	14.6	513.2	55.4	15.6	20.4	4.41	*loops(1)*
0.067	0.52	10	1025	2	30	2	12	294.9	35.6	9.0	28.4	2.83	*loops(1)*
0.067	0.71	10	1025	2	60	4	17.7	220.2	40.6	1.7	16.3	1.62	*smooth loop*
0.067	0.79	10	1025	2	60	4	16	115	31.6	0.9	14.0	1.26	*fig 8*
0.083	0.32	10	1025	2	30	2.5	24.5	1026.8	108.7	20.0	10.6	6.92	*weird*
0.083	0.43	10	1025	2	30	2.5	18	669.7	59.6	13.1	23.0	3.79	*smooth loop[*

Continued on next page

Table B.1 – *Continued from previous page*

$C1$ $[r_c/L_t]$	$C2$ $[v_b/v_f]$	A_k [m^2]	ρ [kg/m^3]	v_f [m/s]	L_t [m]	r_c [m]	T [s]	P [kW]	s_k [m]	$P1$ $\left[\frac{P}{\rho {v_f}^3 {r_c}^2}\right] 10^6$	$P2$ $\left[\frac{P}{\rho {v_f}^3 {s_k}^2}\right] 10^9$	$s_k/(2\pi r)$	*comments*
0.083	0.52	10	1025	2	30	2.5	15	124.9	39.2	2.4	9.9	2.50	*smooth loop[*
0.083	0.32	10	1025	2	30	2.5	24.5	954.2	93.2	18.6	13.4	5.93	*loops*
0.083	0.43	10	1025	2	30	2.5	18	649.7	61.9	12.7	20.7	3.94	*smooth loop*
0.083	0.52	10	1025	2	30	2.5	15	319	50.7	6.2	15.1	3.23	*loops weird*
0.083	0.71	10	1025	2	60	5	22	341.1	50.2	1.7	16.5	1.60	*loop smooth*
0.083	0.79	10	1025	2	60	5	20	209.8	50.2	1.0	10.2	1.60	*loop smooth*
0.2	0.7	10	1025	3	25	5	15.00	1232.6	77.6	1.8	7.4	2.47	*loops*
0.2	0.9	10	1025	3	25	5	11.60	561.6	52.3	0.8	7.4	1.66	*smooth*
0.3	0.7	10	1025	5	30.0	9	16.16	1874	106.2	0.2	1.3	1.88	*smooth*
0.3	0.9	10	1025	4	30.0	9	15.71	1452.9	104.9	0.3	2.0	1.86	*smooth*
0.33	0.33	500	1.225	9	600	300	628.3	1730	3500	0.0	0.3	1.86	*Fagiano*